Numerical simulation of a magnetron discharge utilized for the reactive sputter deposition of titanium nitride and oxide layers

Proefschrift voorgelegd tot het behalen
van de graad van Doctor in de Wetenschappen
aan de Universiteit Antwerpen te verdedigen door

Evi Bultinck

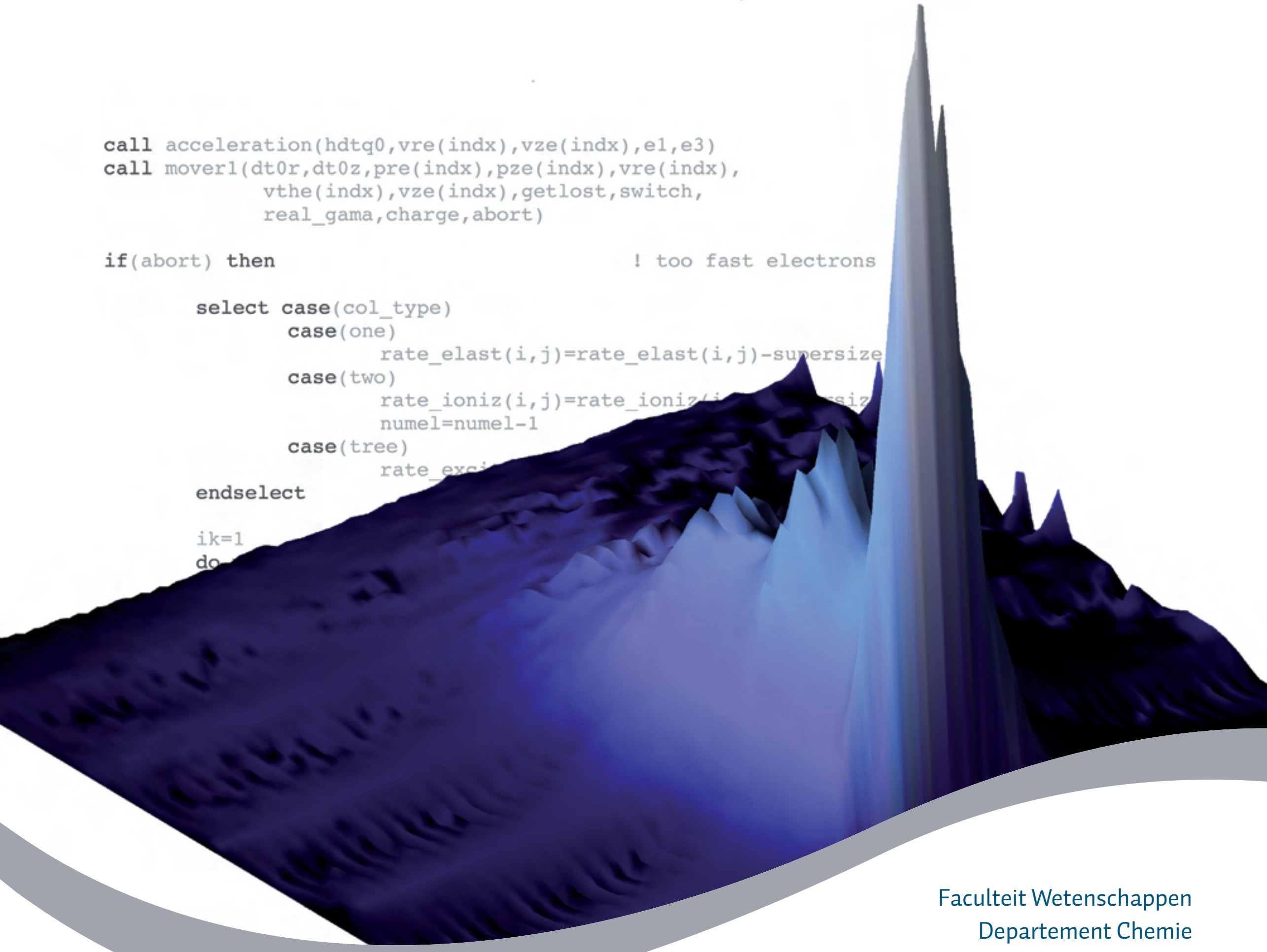

```
call acceleration(hdtq0,vre(indx),vze(indx),e1,e3)
call mover1(dt0r,dt0z,pre(indx),pze(indx),vre(indx),
            vthe(indx),vze(indx),getlost,switch,
            real_gama,charge,abort)

if(abort) then                              ! too fast electrons

      select case(col_type)
            case(one)
                  rate_elast(i,j)=rate_elast(i,j)-supersize
            case(two)
                  rate_ioniz(i,j)=rate_ioniz
                  numel=numel-1
            case(tree)
                  rate_exc
      endselect

      ik=1
      do
```

Faculteit Wetenschappen
Departement Chemie

Promotor
Prof. Dr. Annemie Bogaerts

Universiteit Antwerpen

Universiteit Antwerpen

Faculteit Wetenschappen
Departement Chemie

Numerical simulation of a magnetron discharge utilized for the reactive sputter deposition of titanium nitride and oxide layers

Numerieke simulatie van een magnetron ontlading aangewend voor de reactieve sputter depositie van titaan nitride en oxide lagen

Proefschrift voorgelegd tot het behalen
van de graad van doctor in de wetenschappen
aan de Universiteit Antwerpen
te verdedigen door

Evi BULTINCK

Promotor: Prof. Dr. Annemie Bogaerts

Antwerpen, 2009

Contents

Acknowledgments

Before starting with the scientific part of this PhD thesis, this will be an appropriate place and time to thank the people that have helped me during the past four years. Without these people, this doctoral thesis would not have been possible.

First of all, I would like to express my deepest gratitude and respect to my advisor, Prof. Annemie Bogaerts. Even without reference of previous work, she gave me unconditional belief and faith, which encouraged me from the first day on. Her enthousiasm was contagious, her views enlighting. Even in busy times, she always found the time to discuss problems. Also, I would like to thank her for the many opportunities to spread my scientific results world-wide.

I also had the honour to know Prof. Renaat Gijbels. Thank you professor, for your never ending stimulation to be critical, for making me think outside the chemical box, for making difficult things look easy, and for finding flaws in my reports no one else could. Especially during the application of my IWT fellowship, your help was indispensable.

This computational work started from an already exsisting code, written by Ivan Kolev. Therefore, I am also grateful for his contribution in sharing his knowledge and computer code with me.

Numerical simulations give us a theoretical view on certain physical issues. However, it is essential to not lose grip with reality. In this scope, I would like to thank all the experimentalists I met, who always questioned my theoretical findings, especially Prof. Diederik Depla and Dr. Stijn Mahieu. Thank you very much for the nice collaboration, and for giving me the opportunity to experiment for myself.

This computational work would not have been possible without the powerful UA supercomputer, CalcUA. Also, I appreciate the help of Tom Dockx and Stefan Becuwe, the former and present system administrators.

For more general computer issues, I could always count on the PLASMANT computer specialist, Luc Van ’t Dack, for solving small and bigger computer problems.

The administrative side of this doctoral work was covered by the women of the secreteriat, Ingrid Swenters, Nelly Suijkerbuijk, and Tania Beyers. Thank you very much for the hearty care of all the paper work.

Financially, I am indebted to the Institute for the Promotion of Innovation through Science and Technology in Flanders (IWT-Vlaanderen), and the University of Antwerp.

A big thank you to all of my group members, for the daily talks and breaks. You made the stay in PLASMANT very nice. Especially, I thank David and Tom, my two former class mates, and simultanious PhD starters with me, for sharing similar satisfactions and frustrations. Also, a special thank you to Axel, Erik and Maxie, my office colleagues, for making B2.32 a room full of joy. You are the (as)best!

Besides the people who supported me scientifically or university related, a lot of people from my personal life have encouraged me in one way or another. I would like to thank all my friends for the wonderfull times and talks we had together, in particular Gie, Kurt, Maxie and Wine. A special assignment to all the people I met during my study time, e.g. from KDA and Hera. Also, I would like to thank Harmonie Labore et Constantia and Harmonie Sint-Bavo for the musical relaxation.

Lastly, I greatly acknowledge my whole family for the cosiness at their welcoming homes, and for the belief and interest in me and my work. In particular, I want to thank Marina, Bert, Ellen, and Davy for the chances I got, for always encouraging me, and for supporting me indisputably in all my choices.

Evi Bultinck, June 2009

List of Figures

List of Tables

List of abbreviations

List of symbols

2D	two-dimensional
3D	three-dimensional
A	cathode target area (m^2)
a_0	Bohr radius (5.2918×10^{-11} m)
B	magnetic field (G)
b	impact parameter, or distance of closest approach (m)
DC	direct current
E	electric field (V/m); or species energy (eV)
g	relative velocity (m/s)
I	plasma current (A)
J	surface current density ($\mathrm{A/m}^2$)
k_B	Boltzmann constant (1.380662×10^{-23} J/K)
m, M	mass (kg)
MCC	Monte Carlo collisions
n	species density (m^{-3})
p	pressure (Pa)
P	collision probability
PIC	particle-in-cell
q	electric charge (C)
r	radial position (m)
R	resistance (Ω)
RC	reflection coefficient

$RN[x,y]$	random number, uniformly distributed in the interval $[x,y]$
S	surface area (m^2)
$SEEC$	secondary electron emission coefficient
SC	sticking coefficient
SC_{eff}	effective sticking coefficient
SP	superparticle
t	time (s)
T	temperature (K)
U_s	sublimation energy (eV)
v, V	velocity (m/s)
v', V'	after collision velocity (m/s)
V_0	cathode voltage or potential (V)
V_b	breakdown voltage or potential (V)
V_L	dimensionless voltage, caused by an applied voltage of 1 V
$V_{(P)}$	plasma potential (V)
Vol	volume (m^3)
W	weight factor, number of real particles per superparticle
x	a general position (m)
Y	sputter yield
z	axial position (m)

α	thermal accomodation coefficient
α_p	polarizability ($\ldots\times a_0$)
β	dimensionless impact parameter
β_∞	dimensionless impact parameter for which deflection angle χ is negligibly small
Δr	radial dimension of grid cell (m)
Δz	axial dimension of grid cell (m)
Δt	time step (s)
ϵ_0	permittivity of vacuum (8.854×10^{12} F/m)
θ	spherical polar angle (rad); or a general angle (rad)
$\theta_{cs}^{t,r}$	compound fraction on the substrate (at time t and position r)

λ_D	Debye length (m)
μ	reduced mass (kg)
ρ	volume charge density (C/m^3)
σ	surface charge density (C/m^2); or collision cross section (m^2); or differential cross section (m^2)
ϕ	spherical azimuthal angle (rad)
φ	angle between center of mass reference frame and laboratory reference frame (rad)
χ	deflection or scattering angle (rad)

List of subscripts and superscripts

dis	discharge
e	electron
ej	ejected electron
exc	excitation
ext	external circuit
inc	incoming, or incident species
ion	ionization
r	radial
$refl$	reflected species
$scat$	scattered species
$slow$	slow species
sp	sputtered species
T	total
t	time
thr	threshold
tar	target
$wall$	wall
z	axial
θ	angular

Part I

Background

Chapter 1

Introduction

1.1 Motivation

A plasma is referred to as the fourth state of matter, and consists of a *partially ionized gas*. The presence of reactive ions and electrons, and the interactions betweem them, is the origin of plasma applications. Besides omnipresent plasmas in the universe like stars, sun wind, lightning, . . . , laboratory plasmas are very often subdivided into two groups, according to their temperature. The plasmas that are investigated in this work are *low temperature plasmas* or *gas discharges*.

A gas discharge is generated by applying a sufficiently high potential difference between two electrodes placed in a gas. The generated *electric field* partially breaks down the gas into ions and electrons, which can interact in different plasma processes. Gas discharges are nowadays intensively used for many different industrial applications, such as plasma displays, lamps, lasers, and biomedical (e.g. sterilisation) and environmental (e.g. water cleaning) applications. Also, gas discharges are applied in the field of surface modification, among which etching and sputter deposition, for example to activate, clean, or coat a material.

When besides the electric field, also a *magnetic field* is applied, the electrons can be used more efficiently. This kind of gas discharge is called *"magnetron discharge"*, and is used since the 1970's [1] as *sputter deposition device*, for coating materials with a thin metallic or compound layer. As such, this protective layer can improve the coated material with certain mechanical and optical properties (for example anti-reflective, anti-static, hard, and corrosion and wear resistant, to be used on displays, machinery, food packaging, sun blinds, solar cells, medical implants, ...). Also certain electrical properties can be achieved (for example to be used on semiconductor chips, solar cells, ...). Nowadays, magnetron sputter deposition has become the established technique of choice for the deposition of a large variety of industrially important thin films.

The industrially important applications of sputter deposition make a magnetron discharge very interesting to investigate. *Experimentally*, this device has been widely investigated over the years (wide overviews are presented in [2, 3]). However, several experimental techniques can only be carried out at limited locations in the discharge (for instance not always close to the target), and certain characteristics are hard to measure (for instance certain particle densities), or cannot be measured at all (for instance information on separate collision processes). Moreover, certain measuring techniques, such as Langmuir probe measurements, can even disturb the discharge. *Numerical modeling* can overcome some of these experimental obstacles.

Therefore, this work is dedicated to the numerical investigation of the magnetron discharge used for sputter deposition of thin films. Different kinds of models exist to investigate gas discharges. Dependent on the type of discharge, its conditions, and the desired information and corresponding accuracy, the most suitable model can be chosen. In this thesis, a so-called *"particle-in-cell/Monte Carlo collisions (PIC/MCC)"* modeling technique is applied. The purpose of this work is to obtain fundamental understanding of the chemical and physical reactions in a magnetron discharge, and thereby to visualize and predict theoretically the sputter deposition process.

1.2 Magnetron sputter deposition

1.2.1 Sputter deposition

The main industrial application of magnetron devices is a process called "sputter deposition". In this process, species with a sufficient amount of energy bombard a target, which initiates a collision cascade in the target, leading to a possible release of a surface atom. This target process is called "sputtering". The sputtered atoms pass through the plasma and can be deposited on a substrate, forming a thin coating. The sputter deposition mechanism is schematically presented in figure 1.1.

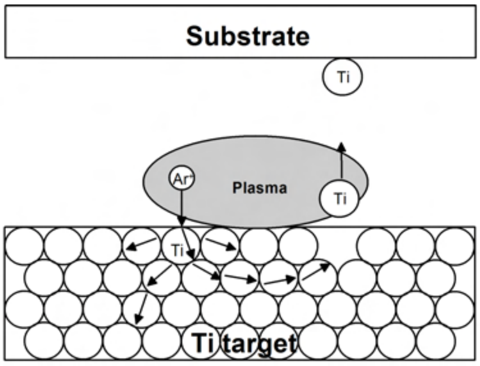

Figure 1.1: Schematic presentation of the sputter deposition process. After bombardement of (for example) Ar^+ ions from the plasma, a collision cascade follows in the Ti target, after which a Ti atom can be sputtered. Subsequently, this Ti atom can be deposited on a substrate.

In our case, the energetic species originate from argon background gas, which is electrically transformed into a plasma: by coupling an electrical circuit to the target, and setting the other walls at ground potential, the target acts as a cathode, and the other walls as anode. Hence, an electric field is generated, which partially breaks down the gas into ions and electrons, i.e. a plasma is created.

In a magnetron discharge, the plasma is magnetically enhanced: by placing magnets behind the cathode target, a magnetic field is created. Charged particles with mass m, velocity v, and charge q from the plasma circulate around the magnetic field lines with magnitude B, with their *Larmor radius*:

$$r = \frac{mv}{qB} \tag{1.1}$$

The high ion mass causes the ion Larmor radius to be very large, leading to an almost straight movement of the ions. However, electrons have a much lower mass, which causes them to be trapped in the magnetic field. As a consequence, the electrons have longer mean free paths, and therefore a higher probability for ionizing the background gas, and hence creating ions. When these ions, accelerated by the electric field, hit the cathode target, target material can be sputtered. The enhanced ionization results in *more sputtering*, and allows the magnetron to operate at lower pressures (typically in the range of 0.1 to 1 Pa [4]) in comparison to non-magnetized sputtering discharges. Due to the lower pressure, the sputtered atoms will be less scattered on their way to the substrate. This results in a *more efficient deposition*.

Most magnetized electrons reside where the radial magnetic field is at maximum. As a consequence, the ionizations occur in the same area. In the present work, a *planar circular magnetron in a cylindrical chamber* is investigated: the magnetron consists of a planar cirular cathode on which a planar cirular target is clamped. The magnetron is *balanced*, meaning that the majority of the magnetic flux lines that originate at, also return to the cathode without crossing the anode. In a planar balanced magnetron, the maximum plasma density is therefore found in a narrow area in front of the cathode, denoted as a dotted area in figure 1.1. Therefore, the planar circular target is locally sputtered, leaving behind an erosion cavity, the so-called “race track”. Consequently, the target is ineffectively and rapidly consumed. Furthermore, a non-uniform sputtering causes also a non-uniform deposition. Therefore, the challenge is to find the optimal operating conditions, whereby the target is more efficiently used, and the deposited film is more uniform, keeping the deposition rate as high as possible.

Alternatively, in order to avoid a non-uniformly consumed target, different magnetron configurations can be built, such as (rotating) cylindrical targets, with a larger and more uniform sputtered surface as advantage [5, 6]. However, the simplicity of a planar target makes its use, and therefore its investigation, very interesting.

On the other hand, to control the properties of the deposited film, the magnetic configuration can be unbalanced, i.e. the magnetic flux lines do cross the anode before returning to the cathode. As a consequence, electrons, and by ambipolar diffusion also ions, follow the magnetic field lines. Hereby, the substrate is bombarded by ions, causing modification of the film properties, such as orientation, hardness, wear resistance, and corrosion resistance of the film [7–11]. However, the deposition rate is lower than the balanced alternative, due to a more spread out plasma, and hence a less efficient ionization. Consequently the sputter rate is lower in the unbalanced case.

1.2.2 Reactive sputter deposition

When a reactive gas, like nitrogen or oxygen, is added to the argon background gas, atoms originating from this reactive gas or the gas molecules themselves can react with the sputtered metal atoms on the substrate to form a *metal nitride* [8, 12–18] or *oxide layer* [9, 19, 20], in a process called "reactive sputter deposition". This process is presented schematically in figure 1.2.

However, when a reactive gas is added to the argon background gas, ions from the reactive gas can be implanted in the target material, reactive gas molecules and atoms can be chemisorbed at the target surface, and chemisorbed species can be knock-on implanted into the target. Subsequently, they react with the target atoms, to form a nitride or oxide layer [21], denoted as "TiN_x target" on figure 1.2. Note that, apart from Ti atoms, N or

O atoms can now also be sputtered from the poisoned TiN_x or TiO_x target. This surface modification process is called *"target poisoning"*, and influences all of the plasma properties. One very important disadvantage of poisoning is that it may drastically reduce the sputter yield and thereby the deposition rate [22]. Furthermore, the transition from the so-called "metallic" to "reactive" condition happens via a complex and inconvenient hysteresis [21, 23]. On the other hand, in order to deposit a stoichiometric metal nitride or oxide film, the reactive gas is needed. The goal here is to find reactive/background gas proportions which allow a satisfactory high deposition rate, as well as the deposition of a stoichiometric film.

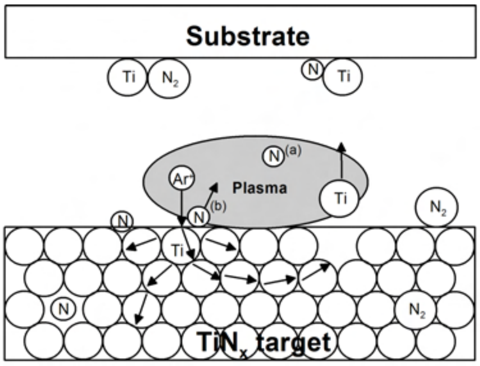

Figure 1.2: Schematic presentation of the reactive sputter deposition process. N atoms, originating from the reactive N_2 gas or the N_2 gas molecules themselves can react with sputtered Ti atoms on the substrate to form a TiN_x film.

1.3 Experimental studies

Magnetron (reactive) sputter deposition is studied extensively by experiments: an overview on sputter deposition is presented in [2], and on reactive sputter deposition in [3]. These experiments enable to discover and explain relations between external parameters, such as cathode current and voltage, gas pressure and pumping speed, magnetic field, geometrical characteristics of the magnetron,. . . and the measured properties.

Current, voltage and pressure can change during the time progression of the discharge: these *macroscopic characteristics* are measured easily with an amperometer, a voltmeter, and a capacitance gauge, respectively. Certain less accessible macroscopic characteristics can be measured with more advanced equipement, such as the erosion profile at the target, which is measured with profilometry or interferometry.

More advanced techniques are available to measure *microscopic properties*, such as species densities, fluxes and energies in the plasma, plasma potential distribution, and characterization of the deposited thin film. These techniques comprise energy resolved mass spectrometry, Langmuir probe measurements, and optical techniques. It should however be mentioned that certain microscopic characteristics are more precarious to measure due to possible plasma disturbance with the measuring tool and/or limitations in size of the measuring tool (so certain areas are not reachable).

1.4 Numerical studies

As mentioned in section 1.1, several experimental techniques suffer from limitations: limited locations of measurement in the discharge, certain characteristics are hard to measure or cannot be measured at all, or measuring tools can disturb the plasma. However, to validate the developed numerical models, experiments still remain inevitable. Moreover, certain input parameters are required in models, which need to be measured experimentally. Therefore, the combination of experiments and numerical models is desirable to provide a complete chemical and physical picture of plasma discharges, needed to optimize the applications.

Different kinds of models exist to simulate gas discharges. Mostly, these models are subdivided into analytical, continuum and particle models, and hybrid models comprise combinations of these aforementioned models. In each of the subsequent sections, a general explanation is given, followed by some examples in literature for the case of magnetron discharges.

1.4.1 Analytical models

Analytical models are based on *simple analytical (mostly (semi-)empirical) formulas* to describe the behavior of macroscopic plasma characteristics, such as voltage, current, pressure, and magnetic field. Their advantage is a short calculation time, but, since approximations are used, this goes in expense of accuracy. Also, these models are mostly not general: they only apply for a limited range of discharge conditions.

For magnetron discharges, analytic models exist to calculate rapidly some general relations between macroscopic plasma characteristics [2, 24–29]. The simulation domain is frequently approximated to a one-dimensional (or even zero-dimensional) space [24, 26, 27], which fastens the calculation considerably. However, in general, plasma species move in all directions due to collisions and diffusion. Especially in the presence of a curved magnetic field, the electrons move in different dimensions (parallel to the electric field lines, and around the curved magnetic field lines). Without second dimension, only constant, uncurved magnetic fields can be investigated. However, two-dimensional analytical models were developped, which are able to describe the magnetron in a more complete and correct way [2, 28, 29]. The advanced analytical model of [2,29] is able to calculate self-consistently plasma characteristics over a wide range of external parameters. Furthermore, the reactive sputter deposition process itself is modeled in [22,30,31], by means of balance equations of the particle fluxes towards these surfaces.

1.4.2 Continuum models

Continuum or fluid models are based on the *continuity and flux equations* for the plasma species in combination with the Poisson equation, to calculate, relatively fast, the electric field in a self-consistent way. It is hence a very powerful modeling approach, if the “local field approximation” is fullfilled, i.e. the energy of the charged particles must be in equilibrium with the electric (and magnetic) field. More precisely, the energy loss by the collisions must be more or less equal to the energy gain by the fields, and hence the plasma must behave as a continuum or a fluid.

Fluid models are widely used to simulate gas discharges, however, modeling magnetron discharges with a fluid model is not so common, since they cannot be simply considered as a fluid. Indeed, in a low pressure discharge, such as a magnetron, the loss of energy caused by collisions is much smaller than the energy gain due to the electric and magnetic field, especially for electrons. Furthermore, the complexity of the magnetic field makes a continuum model for magnetron discharges very inefficient [32]. However, some have reported on fluid modeling for magnetron discharges [33, 34], thereby trying to solve the above mentioned problems.

1.4.3 Particle models

Particle models do not suffer from the condition of continuum models, because *all particles are followed individually*, instead of as one continuum. An example is a “Monte Carlo (MC)” model [35], which treats the collisions probabilistically, and calculates the movement of the charged particles, starting from a known electric field distribution. This implies that the MC model is not self-consistent. However, this model can be coupled to a so-called “particle-in-cell (PIC)” model [36–39], which calculates the electric field, produced by the external electrical circuit and the spatial distribution of the charged particles, in a *self-consistent* manner. The coupled model is named *“particle-in-cell/Monte Carlo collisions (PIC/MCC)” model* [37–39], and is able to produce a wealth of data, such as cathode voltage and current, species densities, fluxes and energies, potential distribution, and information on the individual collisions in the plasma. PIC/MCC models calculate the entire discharge behavior very accurately, however, a drawback is the longer calculation time, which is partially accounted for by representing real particles by a limited number of superparticles (SPs), and by weighting the SPs on a grid (hence the name "particle in cell"). However, permanently evolving computational devices (fast computers) and methods (code parallellizing) make these methods very attractive.

Magnetron sputter deposition is investigated by MCC models [6], and more precisely, reactive sputter deposition was studied in [40].

PIC/MCC models for sputter deposition in a pure Ar discharge are extensively developed [37–39, 41–45], but to our knowledge, no PIC/MCC model exists for an Ar/N_2 mixture, and only one PIC/MCC model [46] exists for an Ar/O_2 gas mixture. However, this PIC/MCC model does not take into account plasma-surface interactions, such as target sputtering, target poisoning, and atom sticking, i.e. the sputter deposition process itself is not described. Moreover, these plasma-surface interactions influence all of the calculated discharge characteristics [21, 23]. Secondly, the external circuit is not included in the model of [46]. Nevertheless, the external circuit occurs to be inevitable in a PIC/MCC code for an accurate and correct description of magnetron discharges [47], see also section 2.2.3.

1.4.4 Hybrid models

Hybrid models can be *combinations* of one or more of the above mentioned models. In that manner, the advantages of the used modeling approaches are coupled. However, the term is mostly applied to denote the combination of MC or PIC/MCC descriptions for the fast electrons, and fluid approaches for all the other species (slow electrons, ions, and neutrals). In that manner, the calculation time is much shorter than a complete PIC/MCC description for all the charged species. However, as mentioned before, due to the low pressure, a fluid approach for the charged particles is not suitable, since they are far from thermal equilibrium [32]. Moreover, the fluid model describes the complex magnetic field in magnetrons very inefficiently [32].

Aim of the work

In our opinion, the PIC/MCC modeling approach produces the most elaborate and accurate data, making it a very powerful tool to simulate magnetron discharges. However, as mentioned above, a complete PIC/MCC model does not yet exist to describe the reactive sputter deposition in Ar/N_2 and Ar/O_2 gas mixtures in a magnetron discharge. Therefore, to study the reactive magnetron sputter deposition process of TiN_x and TiO_x layers, a PIC/MCC model is developed in this work, to obtain a complete insight into the complicated, but yet still not entirely unraveled physics inside a magnetron discharge.

1.5 Outline of the thesis

Chapter 2 describes the details of the PIC/MCC modeling method, developed by Kolev for a DC magnetron in pure Ar [37–39] and further extended in this thesis for mixtures of Ar/N_2 and Ar/O_2, including plasma-surface interactions related to reactive sputter deposition. The movement of the charged particles in the electric and magnetic fields, the diffusion dominated movement of the neutrals, the collisions between the species (collision probabilities and post-collision treatment) and their interactions with the reactor walls will be explained.

Chapter 3 emphasizes the importance of including an external electrical circuit, used for generating a plasma, in modeling discharges, such as magnetron discharges. This current-limiting device, consisting of a voltage source and a resistor, is very often omitted in models. The influence of its neglection is investigated on the calculated plasma current and voltage, on particle fluxes and densities, and on the potential distribution in the plasma. The model is validated by experiments.

Chapter 4 handles the effect of the magnetic field strength on the sheath region of a magnetron discharge. By influencing the very important sheath area in the magnetron discharge, other plasma characteristics, such as sputter yield of the titanium target and deposition profile, are greatly affected. Thereby, by a proper choice of the magnetic field strength, the sputter deposition process can be optimized.

Chapter 5 presents the addition of nitrogen gas to the discharge, for the deposition of thin titanium nitride films. The included species and collisions are listed, and the effect of a poisoned target was included. The PIC/MCC model is combined with an analytical surface model to predict the deposition rate of the adsorbed species and the stoichiometry of the deposited film, for different argon/nitrogen gas proportions. Also, detailed and accurate plasma species densities and fluxes are calculated, which are validated by mass spectrometric measurements.

Chapter 6 examines, similar to chapter 5, the addition of oxygen gas to the discharge, for the deposition of thin titanium oxide films. Hereby, the consequences of the present negative O^- ion on the plasma potential is emphasized. Again, the deposition rates of the adsorbed species and the stoichiometry of the deposited film is predicted, and compared to the nitrogen case.

Chapter 2

Particle-in-cell/Monte Carlo collisions (PIC/MCC) model

2.1 Scheme of the simulated magnetron and flow chart of the model

The magnetron setup under study is a planar circular magnetron in a cylindrical chamber. On the planar circular cathode, a circular titanium target is clamped, both with a radius of 25 mm. An external resistance (R_{ext}) and voltage source (V_{ext}), which together form the external electrical circuit [47], are connected to the cathode, to create a direct current (DC). The other walls are placed at a radial distance of 2 mm and an axial distance of 24 mm from the cathode target, and are at ground potential. In this manner, an electric field is created in the discharge, which generates the discharge. Magnets are placed behind the cathode to generate a magnetic field. In the model, the measured axisymmetric magnetic field was given as input. A scheme of the magnetron discharge, simulated in our model, is presented in figure 2.1.

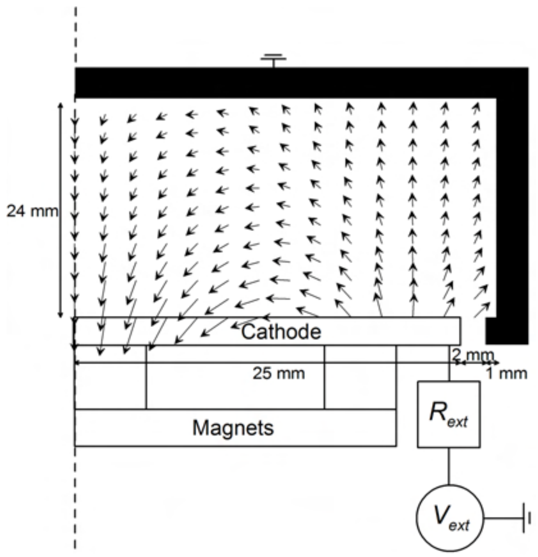

Figure 2.1: Scheme of the simulated two-dimensional (r, z) magnetron discharge, with the external electrical circuit generating an electric field, and the external magnets, creating a magnetic field (magnetic field vectors are indicated on the figure). The cylindrical three-dimensional magnetron discharge is apparent by rotating around the dashed symmetry axis.

Because of the cylindrical symmetry, the magnetron can be described in a two dimensional space, i.e. (r, z) coordinates. However, all three velocity components must be taken into account in order to describe properly the electron gyration around the magnetic field lines, and to satisfy the energy conservation. The model used in the present work is therefore the so-called *"2d3v particle-in-cell/Monte Carlo collisions (PIC/MCC)" model*, i.e. two dimensional in space (2d) and three dimensional in velocity (3v). The outlines of this method are given in [32, 36–39, 47, 48]. The flow chart of the model is presented in figure 2.2. The particle movement is simulated with the particle-in-cell method (see section 2.2), except for the slow neutrals (see section 2.5). The collisions are treated with the Monte Carlo collisions module (see section 2.3). Plasma-surface interactions are accounted for (see section 2.4), and the influence of a poisoned target is included, in case a reactive gas (nitrogen or oxygen) is added. The sequence of steps, presented in figure 2.2, is repeated during succesive time steps Δt until the plasma is at steady state, typically around a simulated time of 15 μs.

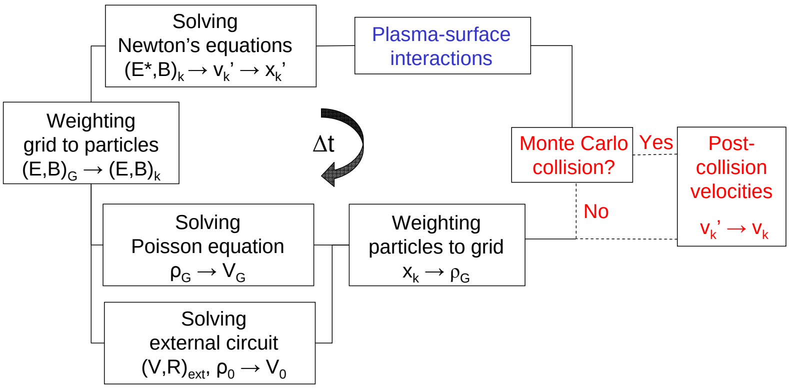

Figure 2.2: Flow chart of the PIC/MCC model. The PIC part is denoted in black (described in section 2.2), the MCC part in red (described in section 2.3), and the plasma-surface interactions in blue (described in section 2.4). Particle quantities are marked with k, grid quantities with G.

2.2 PIC algorithm: particle movement

In the *particle-in-cell (PIC) algorithm*, the space-dependent properties, such as the densities of the charged particles as well as the fast neutrals (i.e. with an energy above thermal energy) are described on a grid. The charged particles in the discharge generate an electrical potential, leading to an electric field. Together with the electrical potential, generated by the external electrical circuit, the total electric field distribution in the discharge is calculated in the PIC algorithm. In other words, the electric field is on one hand generated by the external electrical circuit, and on the other hand created by the charged particles themselves. Apart from the present electric field, a magnetic field is externally applied by the magnets behind the cathode target. Due to the presence of these electric and magnetic fields, the charged particle move in the discharge, which is also described in the PIC algorithm. The neutrals are not influenced by the electric and magnetic fields.

2.2.1 Weighting the superparticle charges to the grid

The real particles in the discharge are represented by a limited ensemble of so-called "superparticles (SPs)". Each SP has a weight factor W which specifies the number of real particles it represents. This is done in order to reduce the computation time. The program starts with a number of SPs and fixed number densities of the electrons and ions. Initially, the SPs are uniformly distributed and their velocities are described by the Maxwellian distribution.

Instead of calculating the field quantities on every SP itself, they are calculated on a grid to reduce the calculation time. As such, the simulation area is divided into grid cells with certain dimensions $(\Delta r, \Delta z)$. The charges of the SPs are assigned to their nearest grid points, hence the origin of the name "particle-in-cell" [36]. In a two-dimensional system, *bilinear* or *area weighting* is applied, i.e. the magnitude of the areas between the charged SP and its four nearest grid points defines the weighting factors, illustrated in figure 2.3.

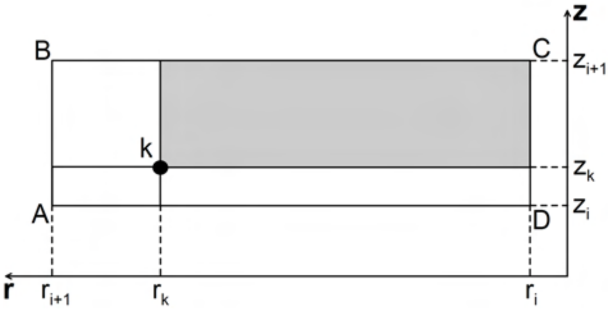

Figure 2.3: The bilinear or area weighting "particle-in-cell (PIC)" method, for the assignement of the charge q of SP k to its nearest grid points in A, B, C and D. For example, the charge assigned to point A equals the charge in k multiplied by the shaded area normalized over the total area $ABCD$.

The charge of SP k, q_k, is divided over its nearest grid points A, B, C and D, in accordance to the fraction of their opposite grid cell area. For example, the charge assigned to grid point A, q_A, is given as:

$$q_A = \frac{(r_k - r_i)(z_{i+1} - z_k)}{(r_{i+1} - r_i)(z_{i+1} - z_i)} q_k = \frac{(r_k - r_i)(z_{i+1} - z_k)}{(\Delta r)(\Delta z)} q_k \tag{2.1}$$

However, when axisymmetric geometries are modeled as in our case, the areas must be a representation of the cylindrical system, instead of simply $r.z$, i.e. rectangular. Therefore, the weighting occurs with *cylindrical volume segments* $\pi.r^2.z$, as presented in figure 2.4.

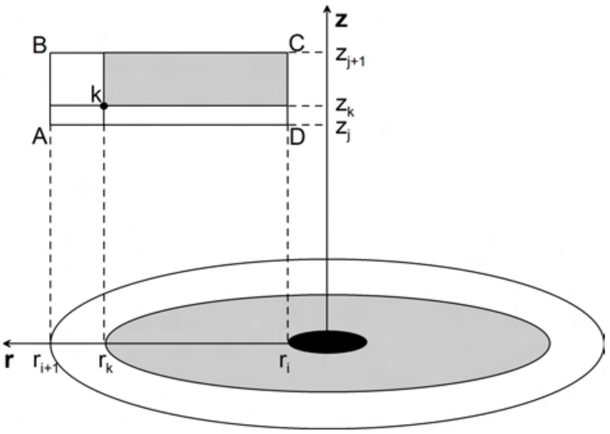

Figure 2.4: The cylindrical volume weighting, for the assignement of the charge q of SP k to its nearest grid points in A, B, C and D. For example, the charge assigned to point A equals the charge in k multiplied by the shaded area, rotated around the z-axis, normalized over the total area $ABCD$, also rotated around the z-axis.

The charge from SP k, q_k, assigned to grid point A, q_A, is given as:

$$q_A = \frac{\pi(r_k^2 - r_i^2)(z_{i+1} - z_k)}{\pi(r_{i+1}^2 - r_i^2)(z_{i+1} - z_i)} q_k = \frac{(r_k^2 - r_i^2)(z_{i+1} - z_k)}{(r_{i+1}^2 - r_i^2)(\Delta z)} q_k \tag{2.2}$$

Assigning the charges of all the present SPs to the corresponding grid points, gives the charge distribution on the grid (for example the sum of all the charge contributions assigned to A is the total charge in A, q_A^{tot}).

The *charged particle density* at each grid point is derived after dividing the total charge by the corresponding volume box around the grid cell:

$$\rho_A = \frac{q_A^{tot}}{\pi(r^2_{(i+1)+1/2} - r^2_{(i+1)-1/2})(z_{j+1/2} - z_{j-1/2})} \tag{2.3}$$

2.2.2 Solving the Poisson equation on the grid

As mentioned above, the charge density distribution on the grid creates an *electrical potential* V, according to the Poisson equation. Besides, the potential distribution is also determined by boundary conditions, i.e. the cathode potential. Therefore, in order to simplify the solution of this equation, we use the *superposition principle*, so that the electrical potential can be presented as the sum of the potential only due to the space charge (V_P) and the potential only due to the cathode voltage (V_0):

$$V = V_P + V_0 V_L \tag{2.4}$$

where V_L is the dimensionless potential caused by an applied voltage with magnitude 1 V [49]. In section 2.2.3, it will be shown how the voltage drop between the electrodes (V_0) is calculated, resulting from the coupling of the external circuit to the plasma. Also, the calculation of V_L will be explained.

V_P can be found as a solution of the *Poisson equation*, which reads in (r, z) coordinates:

$$\frac{1}{r}\frac{\partial}{\partial r} r \frac{\partial V_P}{\partial r} + \frac{\partial}{\partial z}\frac{\partial V_P}{\partial z} = -\frac{q}{\epsilon_0}\left(n_i - n_e\right) \tag{2.5}$$

with q the elementary charge, ϵ_0 the permittivity of vacuum, and n_i and n_e the ion and electron densities, respectively. Equation (2.5) can be solved, applying the *Gauss' theorem* on a box surrounding the grid point (i, j) (see figure 2.5) [50].

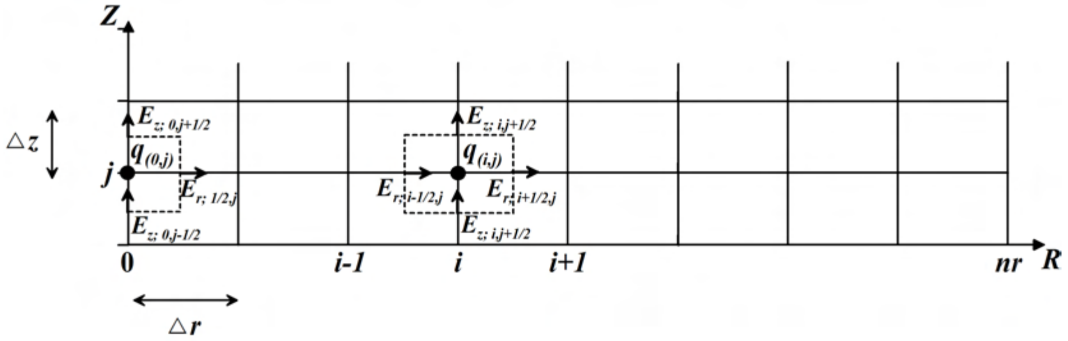

Figure 2.5: The Gauss' theorem on a box surrounding the grid points $(0, j)$ and (i, j) in the discharge.

The Gauss' theorem reads:

$$\oint_{S_{(i,j)}} \mathbf{E} \cdot d\mathbf{S} = \frac{q_{(i,j)}}{\epsilon_0} \tag{2.6}$$

In other words, the charge at grid point (i, j), $q_{(i,j)}$ generates an electric field E working on the box surface $S_{(i,j)}$. As derived from figure 2.5, equation (2.6) can be rewritten as:

$$\begin{aligned} &2\pi r_{i+1/2}\Delta z E_{r;i+1/2,j} - 2\pi r_{i-1/2}\Delta z E_{r;i-1/2,j} \\ &+\pi(r^2_{i+1/2} - r^2_{i-1/2})E_{z;i,j+1/2} - \pi(r^2_{i+1/2} - r^2_{i-1/2})E_{z;i,j-1/2} = \frac{q_{(i,j)}}{\epsilon_0} \end{aligned} \tag{2.7}$$

Using finite differencing, the electric field components can be expressed as:

$$\begin{aligned} E_{r;i+1/2,j} &= -\frac{V_{P;i+1,j} - V_{P;i,j}}{\Delta r} \quad and \quad E_{r;i-1/2,j} = -\frac{V_{P;i,j} - V_{P;i-1,j}}{\Delta r} \\ E_{z;i,j+1/2} &= -\frac{V_{P;i,j+1} - V_{P;i,j}}{\Delta z} \quad and \quad E_{z;i,j-1/2} = -\frac{V_{P;i,j} - V_{P;i,j-1}}{\Delta z} \end{aligned} \tag{2.8}$$

Since the volume of the box $Vol_{i,j} = \pi(r^2_{i+1/2} - r^2_{i-1/2})\Delta z$, and $\rho_{i,j} = q_{i,j}/Vol_{i,j}$, equation (2.7) can be rewritten, using equation (2.8), as a function of the potential V_P:

$$\begin{aligned}&\frac{2r_{i+1/2}}{r_{i+1/2}^2 - r_{i-1/2}^2}\frac{V_{P;i+1,j} - V_{P;i,j}}{\Delta r} - \frac{2r_{i-1/2}}{r_{i+1/2}^2 - r_{i-1/2}^2}\frac{V_{P;i,j} - V_{P;i-1,j}}{\Delta r}\\ &+\frac{1}{\Delta z^2}(V_{P;i,j+1} - 2V_{P;i,j} + V_{P;i,j-1}) = -\frac{\rho_{(i,j)}}{\epsilon_0}\end{aligned} \tag{2.9}$$

Equation (2.9) at the symmetry axis, $i = 0$, becomes:

$$\begin{aligned}&\frac{2r_{1/2}}{r_{1/2}^2}\frac{V_{P;1,j} - V_{P;0,j}}{\Delta r}\\ &+\frac{1}{\Delta z^2}(V_{P;0,j+1} - 2V_{P;0,j} + V_{P;0,j-1}) = -\frac{\rho_{(0,j)}}{\epsilon_0}\end{aligned} \tag{2.10}$$

Since at the other side of the symmetry axis the same equations apply, this implies that the physical boundary condition at $i = 0$ is:

$$\left(\frac{\partial V_P}{\partial r}\right)_{r=0} = 0 \tag{2.11}$$

Moreover, $V_P = 0$ at the surfaces $z = 0$, $z = z_{max}$ and $r = r_{max}$. With these boundary conditions, equations (2.9) and (2.10) are used to obtain the potential distribution in the plasma $V_{P;i,j}$.

2.2.3 External circuit

The ever present cosmic radiation causes a gas to partially ionize into ions and electrons, which recombine again to the neutral gas. However, when a sufficiently high *potential difference* (V_0) is generated over electrodes placed inside the gas, the ions and electrons are accelerated, gaining enough energy to create new charged particles, which causes the discharge to become self-sustaining. This potential difference can be generated by coupling an electrical circuit, consisting of a *constant voltage source* (V_{ext}) and a *constant resistance* (R_{ext}), to one of the electrodes: the cathode. The other walls are at ground potential, and hence they function as the anode. In other words, a potential difference is created over the electrodes, as presented schematically in figure 2.1. The formation of charged particles causes a current I to flow in the discharge. Note that this discharge current is limited to the *current flowing in the external circuit* I_{ext}, because the external circuit is connected in series to the discharge gap. The current influences the potential difference across the electrodes of the discharge V_0, as defined by Kirchhoff's voltage loop law:

$$V_0 = V_{ext} - R_{ext} I_{ext} \tag{2.12}$$

This equation is plotted as a straight line, the "load line", as seen in figure 2.6, and the intercept on the x-axis is the limiting current V_{ext}/R_{ext}.

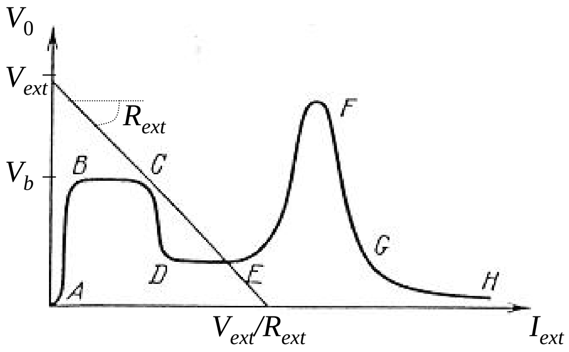

Figure 2.6: General discharge current-voltage characteristics of gas discharges [51]: the symbols A - H are explained in the text below. The diagonal straight line is the load line, which represents equation 2.12: the symbols are explained in the text above.

On the other hand, a plasma can be formed in different *current-voltage regimes*, as can be seen in figure 2.6. Certain areas can be distinguished corresponding to the discharge current. Region A-B (10^{-10} A - 10^{-9} A) is the region of a non-self-sustaining discharge. From a certain "breakdown voltage (V_b)" [51], the discharge becomes self-sustaining, and region B-C (10^{-9} A

- 10^{-5} A) corresponds to the Townsend discharge. Region D-E (10^{-4} A - 10^{-1} A) is the normal glow discharge, E-F (10^{-1} A - 1 A) the abnormal glow discharge, F-G (1 A - 10 A) is the transition to arcing and G-H (10 A - . . .) is the region of an arc discharge.

Since the discharge current I is equal to the external current I_{ext}, the intersect of the load line and the discharge $I - V$ curve determines the discharge current regime, and therefore the type of discharge. In other words, the type of discharge and the discharge current regime are determined by the external resistance and voltage.

In the presence of an external circuit, the cathode potential is a function of both the discharge process and the external parameters. Hence, simultaneous advance in time of the simulation of the discharge and the circuit is necessary, leading to a complete coupling of the discharge and the external circuit. This coupling is maintained by satisfying the *charge conservation* at the cathode [50]:

$$A\frac{d\sigma}{dt} = I_{ext}\left(t\right) + AJ_{dis} \tag{2.13}$$

where A is the cathode area, σ its total surface charge density, I_{ext} is the current in the external circuit and J_{dis} is the current density arriving at the cathode due to the charged discharge species.

The surface charge density σ can be determined independently of equation (2.13) applying the Gauss' theorem on a box surrounding the cathode grid points (see figure 2.7) [50].

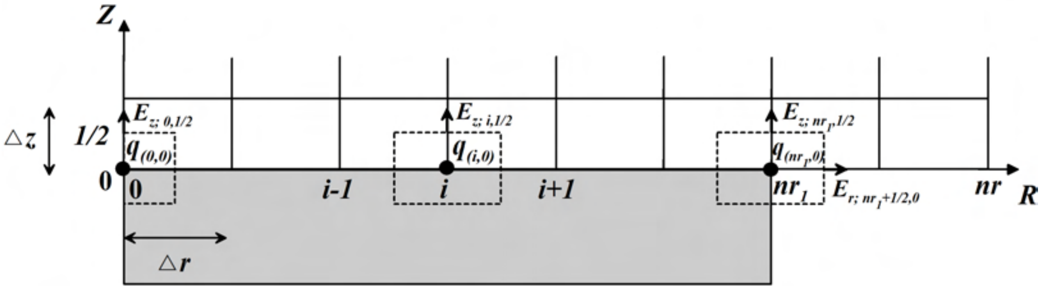

Figure 2.7: The Gauss' theorem on a box surrounding the grid points $(0,0)$, $(i,0)$, and $(nr_1,0)$ on the cathode surface.

The Gauss' theorem reads:

$$\oint_{S_i} \epsilon_0 \mathbf{E} \cdot d\mathbf{S} = \oint_{S_i} \sigma_i dS + \int_{Vol_i} \rho_i dV = q_i \tag{2.14}$$

σ_i represents the surface charge density at point i on the cathode surface, ρ_i the volume charge density in the same point, and q_i the total charge at grid point $(i,0)$.

Similar to the procedure applied in [50], equation (2.14) is equivalent to [52]:

$$\epsilon_0 E_{z;i,1/2} S_i = \sigma_i S_i + \frac{1}{2}\rho_i Vol_i \tag{2.15}$$

$E_{z;i,1/2}$ is the electric field in z-direction in point $(i,1/2)$. S_i is the surface of the box around point i, and Vol_i is its volume, which is equal to $S_i \Delta z$ with Δz the grid size in z-direction. From figure 2.7, it is clear that only half of the volume contributes to the charge density in Vol_i, which declares the factor 1/2.

Using central finite differencing, $E_{z;i,1/2}$ can be expressed as $(V_0 - V_{i,1})/\Delta z$, where V_0 is the cathode potential and $V_{i,1}$ is the potential at the first grid point of the discharge region. The cathode is assumed to be a perfect conductor, meaning that there is no radial dependence of the cathode potential.

Equation (2.15) can then be rewritten analogous to [50], and yields for σ_i [52]:

$$\begin{aligned}\sigma_i &= \frac{\epsilon_0}{\Delta z}V_0 - \frac{\epsilon_0}{\Delta z}V_{i,1} - \frac{\Delta z}{2}\rho_i \qquad\qquad i \in [0, nr_1 - 1] \\ \sigma_{nr_1} &= \left(\frac{\epsilon_0}{\Delta z}C_1 + \epsilon_0 C_2\right)V_0 - \frac{\epsilon_0}{\Delta z}C_1 V_{nr_1,1} - C_3\rho_{nr_1,0}\end{aligned} \tag{2.16}$$

with nr_1 the grid point at the cathode border, as illustrated in figure 2.7, and constants C_1, C_2 and C_3:

$$\begin{aligned}C_1 &= \frac{r^2_{nr_1} - r^2_{nr_1-1/2}}{r^2_{nr_1} - r^2_{nr_1-1/2} + r_{nr_1}\Delta z} \\ C_2 &= \frac{1}{r_{nr_1+1/2} - r_{nr_1-1/2}}\frac{r_{nr_1+1} - r_{nr_1}}{r_{nr_2} - r_{nr_1}}\frac{r_{nr_1}\Delta z}{r^2_{nr_1} - r^2_{nr_1-1/2} + r_{nr_1}\Delta z} \\ C_3 &= \frac{\Delta z}{2}\frac{2r^2_{nr_1+1/2} - r^2_{nr_1} - r^2_{nr_1-1/2}}{r^2_{nr_1} - r^2_{nr_1-1/2} + r_{nr_1\Delta z}}\end{aligned} \tag{2.17}$$

The total surface charge density on the cathode is the sum of the surface charge densities in all the cells:

$$\sigma_T = \sum_{i=0}^{nr_1}\sigma_i = \sum_{i=0}^{nr_1-1}\sigma_i + \sigma_{nr_1} \tag{2.18}$$

This yields for the *total cathode surface charge density* σ_T [52]:

$$\sigma_T = a_1 V_0 + a_2\sum_{i=0}^{nr_1-1}V_{i,1} + a_3 V_{nr_1,1} + a_4\sum_{i=0}^{nr_1-1}\rho_{i,0} + a_5\rho_{nr_1,0} \tag{2.19}$$

with:

$$\begin{aligned}
a_1 &= nr_1\frac{\epsilon_0}{\Delta z} + \frac{\epsilon_0}{\Delta z}C_1 + \epsilon_0 C_2 \\
a_2 &= -\frac{\epsilon_0}{\Delta z} \\
a_3 &= a_2 C_1 \\
a_4 &= -\frac{\Delta z}{2} \\
a_5 &= -C_3
\end{aligned} \tag{2.20}$$

On the other hand, equation (2.13) can be discretized with the backward finite difference method (backwards, since we know the surface charge of the previous time step):

$$A\left(\sigma_T^t - \sigma_T^{t-1}\right) = \left[I_{ext}\left(t\right) + AJ_{dis}\right]\Delta t \tag{2.21}$$

Using equation (2.12) for an expression of I_{ext}, equation (2.21) leads to:

$$\sigma_T^t = \frac{1}{A}\left(V_{ext} - V_0\right)\frac{\Delta t}{R_{ext}} + J_{dis}\Delta t + \sigma_T^{t-1} \tag{2.22}$$

Equations (2.19) and (2.22) can then be combined to obtain an expression for the cathode potential V_0. Nevertheless, $V_{i,1}$ depends on both the discharge and the boundary. This implies that the expression is a boundary condition for the Poisson equation, meaning that the Poisson equation must be solved iteratively until the boundary condition is fulfilled. This obviously requires a long calculation time and is computationally very inefficient. Alternatively, the potential $V_{i,1}$ can be expressed with the superposition principle (see also equation (2.4) above) [50]:

$$V_{i,1} = V_{i,1}^P + V_0 V_{i,1}^L \tag{2.23}$$

Combining equations (2.19) and (2.22), and replacing $V_{i,1}$ by equation (2.23) leads to the expression of the *cathode potential* V_0 [52]:

$$V_0 = \frac{-a_2 \sum_{i=0}^{nr_1-1} V_{i,1}^P - a_3 V_{nr_1,1}^P - a_4 \sum_{i=0}^{nr_1-1} \rho_{i,0} - a_5 \rho_{nr_1,0} + J_{dis}\Delta t + a_6 V_{ext} + \sigma_T^{t-1}}{a_7} \tag{2.24}$$

where:

$$\begin{aligned} a_6 &= \frac{\Delta t}{R_{ext} A} \\ a_7 &= a_1 + a_2 \textstyle\sum_{i=0}^{nr_1-1} V_{i,1}^L + a_3 V_{nr_1,1}^L - a_6 \end{aligned} \tag{2.25}$$

In this way, V_0 is calculated self-consistently from the potentials $V_{i,1}^P$ and $V_{i,1}^L$, the volume charge density $\rho_{i,0}$ (at all points i on the cathode surface), the current density of the charged plasma species to the cathode J_{dis}, the cathode surface charge from the previous time step σ_T^{t-1} and the time step Δt itself, and from the constants V_{ext}, R_{ext} and the geometric parameters of the grid. The external current I_{ext}, which equals the plasma current at steady state, can be calculated from equation (2.12).

In equation (2.4), V_0 is multiplied by a dimensionless potential V_L, which is caused by applying 1 V to the cathode [49]. V_L is the solution of the Laplace equation:

$$\Delta V_L = 0 \tag{2.26}$$

with the applied potential boundary condition, i.e. $V_L = 1$ at the cathode surface and $V_L = 0$ at the grounded walls. Moreover, in the gap between the cathode and the grounded wall at $z = 0$, V_L is assumed to decay linearly from 1 to 0 with the distance from the cathode. The Laplace equation needs only to be solved at the beginning of the simulation, which simplifies and accelerates the calculation of the Poisson equation.

2.2.4 Electric field on the grid

In sections 2.2.2 and 2.2.3, it was explained how V_P, V_L and V_0 are calculated. From the superposition equation, i.e. equation (2.4), the total potential distribution at every grid point $V(r,z)$ can be derived. This potential creates an *electric field* $E(r,z)$ in the discharge, according to:

$$\mathbf{E}(r,z) = -\nabla V(r,z) \tag{2.27}$$

This equation is discretized by the central finite difference method:

$$\begin{aligned} E_{r;i,j} &= -\frac{V_{i+1,j} - V_{i-1,j}}{2\Delta r} \\ E_{z;i,j} &= -\frac{V_{i,j+1} - V_{i,j-1}}{2\Delta z} \end{aligned} \tag{2.28}$$

On the surfaces, forward or backward differencing is applied:

$$\begin{aligned} E_{r;nr,j} &= -\frac{V_{nr,j} - V_{nr-1,j}}{\Delta r} \\ E_{z;i,0} &= -\frac{V_{i,1} - V_{i,0}}{\Delta z} \\ E_{z;i,nz} &= -\frac{V_{i,nz} - V_{i,nz-1}}{\Delta z} \end{aligned} \tag{2.29}$$

On the symmetry axis, $i = 0$:

$$E_{r;0,j} = 0 \tag{2.30}$$

2.2.5 Weighting the fields on the grid to the superparticle positions

After calculating the above mentioned characteristics on the grid points (i.e. the charge density, the potential and the electric field), the SPs are moved by the new electric field (caused by the charged particle distribution and the external circuit), together with the external constant magnetic field. Therefore, the electric and magnetic fields on the grid must be weighted on the SPs. A reverse weighting to the one explained in section 2.2.1 is applied for the weighting of the electric field from the grid to the SP positions:

$$\begin{aligned}E_k = &\frac{(r_k^2 - r_i^2)(z_{j+1} - z_k)}{(r_{i+1}^2 - r_i^2)(\Delta z)} E_A + \frac{(r_k^2 - r_i^2)(z_k - z_j)}{(r_{i+1}^2 - r_i^2)(\Delta z)} E_B \\ &+ \frac{(r_{i+1}^2 - r_k^2)(z_k - z_j)}{(r_{i+1}^2 - r_i^2)(\Delta z)} E_C + \frac{(r_{i+1}^2 - r_k^2)(z_{j+1} - z_k)}{(r_{i+1}^2 - r_i^2)(\Delta z)} E_D\end{aligned} \tag{2.31}$$

Similar to the electric field, the external magnetic field is also weighted from the grid to the SP positions.

2.2.6 Solving Newton's equations

The weighted electric and magnetic fields move the SPs, according to *Newton's equations of motion*:

$$\begin{aligned} m\frac{d\mathbf{v}}{dt} &= q\left(\mathbf{E} + \mathbf{v} \times \mathbf{B}\right) \\ \frac{d\mathbf{x}}{dt} &= \mathbf{v} \end{aligned} \tag{2.32}$$

where m represents the mass of a particle, $\mathbf{v}$ its velocity, q its charge, $\mathbf{x}$ its position, $\mathbf{E}$ the electric field, and $\mathbf{B}$ the magnetic field. These continuous equations are discretized using the central finite difference method:

$$\begin{aligned} m\frac{\mathbf{v_{t+\Delta t/2}} - \mathbf{v_{t-\Delta t/2}}}{\Delta t} &= q\left(\mathbf{E} + \mathbf{v_t} \times \mathbf{B}\right) \\ \frac{\mathbf{x_{t+\Delta t}} - \mathbf{x_t}}{\Delta t} &= \mathbf{v_{t+\Delta t/2}} \end{aligned} \tag{2.33}$$

This time-centered finite difference method is called the *"leap-frog algorithm"* [36], which is schematically presented in figure 2.8.

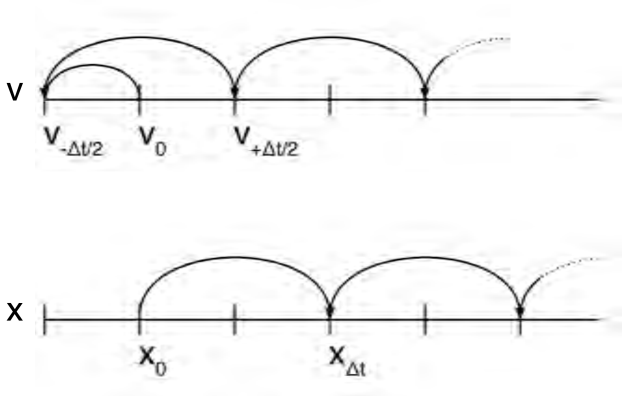

Figure 2.8: Schematic presentation of the leap-frog algorithm, used for central finite differencing of Newton's equations of motion.

In the first time step, the velocity must be "pushed backwards" to obtain $\mathbf{v_{-\Delta t/2}}$. This is done by a backward finite difference equation:

$$m\frac{\mathbf{v_0} - \mathbf{v_{-\Delta t/2}}}{\Delta t/2} = q\left(\mathbf{E} + \mathbf{v_0} \times \mathbf{B}\right) \tag{2.34}$$

The first equation of equation (2.33) contains two terms, i.e. an acceleration along the electric field, and a rotation around the magnetic field lines. Since the first term influences the magnitude of the velocity vector, whereas the second term only influences its direction, the two terms can be solved separately. To be consistent with the time centering, the rotation is carried out in between two half accelerations, schematically presented in figure 2.9.

$$\mathbf{v_{t-\Delta t/2}} \xrightarrow[\text{1/2 }\mathbf{E}\text{ over }\Delta t/2]{\text{Half acceleration}} \mathbf{v'} \xrightarrow[\mathbf{B}\text{ over }\Delta t]{\text{Full rotation}} \mathbf{v''} \xrightarrow[\text{1/2 }\mathbf{E}\text{ over }\Delta t/2]{\text{Half acceleration}} \mathbf{v_{t+\Delta t/2}}$$

Figure 2.9: Schematic presentation of the advance in time of the acceleration along the electric field and rotation around the magnetic field lines.

Here, $\mathbf{v}'$ and $\mathbf{v}''$ are intermediate dummy velocities. In this manner, the velocity is advanced according to the following sequence:

$$\begin{aligned} m\frac{\mathbf{v}' - \mathbf{v_{t-\Delta t/2}}}{\Delta t/2} &= q\mathbf{E} \\ m\frac{\mathbf{v}'' - \mathbf{v}'}{\Delta t} &= q\left(\mathbf{v}' \times \mathbf{B}\right) \\ m\frac{\mathbf{v_{t+\Delta t/2}} - \mathbf{v}''}{\Delta t/2} &= q\mathbf{E} \end{aligned} \tag{2.35}$$

With this new velocity $\mathbf{v_{t+\Delta t/2}}$, the new positions $\mathbf{x_{t+\Delta t}}$ are calculated, according to the second equation of equation (2.33).

The $\mathbf{v}' \times \mathbf{B}$ rotation is treated geometrically according to the algorithm suggested by Boris [53]. If θ is the rotation angle, $\mathbf{v}'$ is first advanced over $\theta/2$ to a dummy $\mathbf{v}^*$, so that $\mathbf{v}^*$ is perpendicular to both the magnetic field line $\mathbf{B}$, and $\mathbf{v}'' - \mathbf{v}'$, as clarified in figure 2.10.

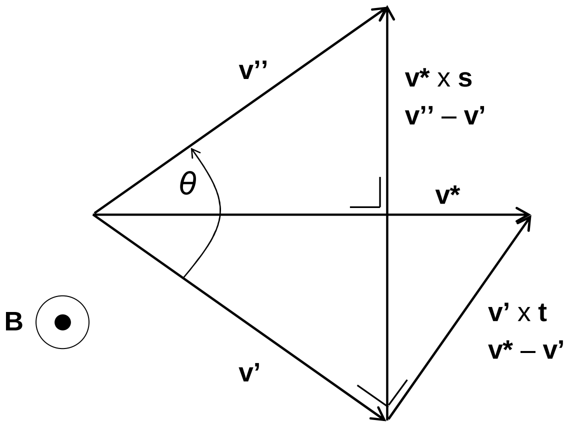

Figure 2.10: Schematic presentation of the rotation from $\mathbf{v}'$ to $\mathbf{v}''$, around the magnetic field line $\mathbf{B}$. All the presented velocity vectors are projections of the actual velocities onto the plane perpendicular to $\mathbf{B}$.

From figure 2.10, it is clear that advancing $\mathbf{v}'$ in its corresponding time step $\Delta t/2$ due to the magnetic field, $\mathbf{B}$, to $\mathbf{v}^*$ is described with a central finite difference equation, similar to the second equation of equation (2.35):

$$\frac{q\mathbf{B}}{m}\frac{\Delta t}{2} = \frac{\mathbf{v}^* - \mathbf{v}'}{\mathbf{v}'} \tag{2.36}$$

Geometrically, this equation can be expressed as a rotation over the angle $\theta/2$:

$$\mathbf{v}^* = \mathbf{v}' + \mathbf{v}' \times \mathbf{t} \tag{2.37}$$

where $\mathbf{t} = \hat{\mathbf{b}} tan\frac{\theta}{2}$, $\hat{\mathbf{b}}$ being the unity vector, parallel to $\mathbf{B}$.

On the other hand, we find from figure 2.10:

$$\mathbf{s} = \hat{\mathbf{b}} sin\theta = 2\hat{\mathbf{b}} sin\frac{\theta}{2}cos\frac{\theta}{2} = 2\frac{\mathbf{v}^* - \mathbf{v}'}{\mathbf{v}^*}\frac{(\mathbf{v}'' - \mathbf{v}')/2}{\mathbf{v}^* - \mathbf{v}'} = \frac{\mathbf{v}'' - \mathbf{v}'}{\mathbf{v}^*} \tag{2.38}$$

From equation (2.38), and similar to equation (2.37), advancing $\mathbf{v}^*$ over $\theta/2$ to $\mathbf{v}''$ is described as follows:

$$\mathbf{v}'' = \mathbf{v}' + \mathbf{v}^* \times \mathbf{s} \tag{2.39}$$

From equations (2.36) and (2.37) follows an expression for $\mathbf{t}$:

$$\mathbf{t} = \hat{\mathbf{b}} tan\frac{\theta}{2} = \frac{q\mathbf{B}}{m}\frac{\Delta t}{2} \tag{2.40}$$

And from equations (2.40) and (2.38), an expression for $\mathbf{s}$ is composed:

$$\mathbf{s} = \hat{\mathbf{b}} sin\theta = \frac{2\hat{\mathbf{b}} tan\frac{\theta}{2}}{1 + \hat{\mathbf{b}} tan^2\frac{\theta}{2}} = \frac{2\mathbf{t}}{1 + \mathbf{t}^2} \tag{2.41}$$

In order to implement equations (2.37) and (2.39) in the model, these equations must be converted into cylindrical coordinates:

$$\begin{aligned}
&v_r^* = v_r' + v_\theta' t_z \quad ; \quad v_z^* = v_z' + v_\theta' t_r \quad ; \quad v_\theta^* = v_\theta' + v_z' t_r + v_r' t_z \\
&v_r'' = v_r' + v_\theta^* s_z \quad ; \quad v_z'' = v_z' + v_\theta^* s_r \quad ; \quad v_\theta'' = v_\theta' + v_z^* s_r + v_r' s_z
\end{aligned} \tag{2.42}$$

Here, t_r, t_z, t_θ and s_r, s_z, s_θ are derived from equation (2.40) and equation (2.41), respectively:

$$\begin{aligned}
&t_r = \lambda B_r \quad ; \quad t_z = \lambda B_z \quad ; \quad t_\theta = 0 \\
&s_r = \frac{2\lambda B_r}{1 + \lambda^2 \left(B_r^2 + B_z^2\right)} \quad ; \quad s_z = \frac{2\lambda B_z}{1 + \lambda^2 \left(B_r^2 + B_z^2\right)} \quad ; \quad s_\theta = 0
\end{aligned} \tag{2.43}$$

where $\lambda = \dfrac{q\Delta t}{2m}$.

2.3 MCC algorithm: particle collisions

Apart from moving in the electric and magnetic fields, the (charged) particles in the discharge can also interact with each other, described in the *Monte Carlo collisions (MCC) algorithm.* The occurrence of the collision is dependent on the velocity of the incident particle, the density of the target species, and a collision probability, which is based on the collision cross section (the effective area for collision), or on the reaction rate constant. This is discussed in detail in section 2.3.1.

Dependent on the colliding species (electrons, ions, atoms, and/or molecules) and on the type of collision (elastic or inelastic), post-collision velocities can be calculated. Section 2.3.2 presents a general overview of the collisions' treatment. The collisions included in the models are summarized in the corresponding chapters in part II.

2.3.1 Probability and type of collision

In the model, the occurrence of collisions is treated at the middle of each time step to be consistent with the time centering of the leap-frog algorithm. Assume that a certain species has N different types of possible collisions. To decide which type of collision occurs, the interval $[0, N]$ is divided into N equal subintervals. Then, a random number, uniformly distributed in the interval $[0, N]$, is generated. In all the following, this is denoted as "$RN[0, N]$". This $RN[0, N]$ belongs to a certain subinterval, which corresponds to the collision type that might take place. This procedure is schematically presented in figure 2.11.

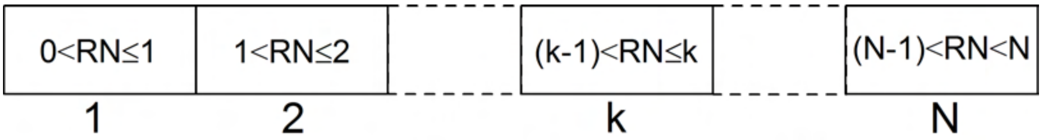

Figure 2.11: Schematic presentation of the choice of collision type, based on a random number between 0 and N ($RN[0, N]$) and on the amount of possible collisional events, N, for a certain type of SP.

To define whether this k^{th} collision type really takes place, the *collision probability* P_k is calculated, for a SP i of energy E_i and velocity v, to collide with a target SP with species density, n_{tar}:

$$\begin{aligned} P_k &= 1 - \exp\left(-\Delta t \cdot n_{tar} \cdot v \cdot \sigma_k\left(E_i\right)\right) \\ or \quad P_k &= 1 - \exp\left(-\Delta t \cdot n_{tar} \cdot \frac{v}{\langle v \rangle} \cdot k_k\left(E_i\right)\right) \end{aligned} \tag{2.44}$$

$\sigma_k\left(E_i\right)$ is the collision cross section as a function of the energy of the incident SP. In case the collision probability is defined by a rate constant k_k, the velocity of the incident SP must be divided by the average velocity of the incident SP species.

This probability is compared to another random number, uniformly distributed in the interval $[0, 1]$. If this $RN[0, 1]$ is smaller than or equal to P_k, the k^{th} collision effectively takes place, and the SPs receive new velocities according to the collision type. This procedure is schematically presented in figure 2.12.

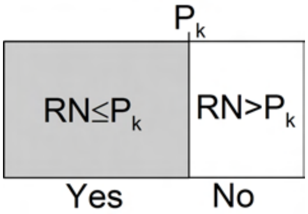

Figure 2.12: Schematic presentation of the probability P_k that the k^{th} collision type takes place.

2.3.2 Post-collision velocities

After the collision, the SPs are scattered from their original part, and their new velocities (direction and magnitude) are based on the *center of mass theory* [54]. Dependent on the type of collision, the total kinetic energy is conserved (elastic collisions) or not (inelastic collisions). In the latter case, the energy is partly consumed as internal chemical energy for one of the collision partners (such as excitation, ionization, dissociation, dissociative ionization), or created and supplied to the discharge as light or heat (such as deexcitation, recombination).

In the center of mass description, the electrons, ions, atoms and molecules are assumed to have spherical shapes. Since the total momentum is conserved, the center of mass will always move with a constant velocity $\mathbf{w}$, and therefore it is convenient to work in the center of mass reference frame. Its constant velocity, $\mathbf{w}$, is defined as a function of the masses (m and M) and (pre-collision) velocities ($\mathbf{v}$ and $\mathbf{V}$) of the collision partners:

$$\mathbf{w} = \frac{m\mathbf{v} + M\mathbf{V}}{m + M} \tag{2.45}$$

Therefore, in the center of mass reference frame, the pre-collision velocities $\tilde{\mathbf{v}}$ and $\tilde{\mathbf{V}}$ are:

$$\begin{aligned} \tilde{\mathbf{v}} &= \mathbf{v} - \mathbf{w} = \frac{M}{m+M}\mathbf{g} = \frac{\mu}{m}\mathbf{g} \\ \tilde{\mathbf{V}} &= \mathbf{V} - \mathbf{w} = -\frac{m}{m+M}\mathbf{g} = -\frac{\mu}{M}\mathbf{g} \end{aligned} \tag{2.46}$$

with $\mathbf{g}$ the relative pre-collision velocity $\mathbf{v} - \mathbf{V}$, and μ the reduced mass $mM/(m+M)$. Consequently, the pre-collision momenta of the collision partners are:

$$\begin{aligned} m\tilde{\mathbf{v}} &= \mu\mathbf{g} \\ M\tilde{\mathbf{V}} &= -\mu\mathbf{g} \end{aligned} \tag{2.47}$$

Equations (2.46) and (2.47) illustrate that, in the center of mass reference frame, the pre-collision velocities are opposite in direction, as for the corresponding momenta, which are also equal in magnitude.

After the collision, the particles are scattered from their original path, as illustrated in figure 2.13. Satisfying conservation of energy, the magnitude of the velocities must be unchanged by a collision (only the direction is changed):

$$\begin{aligned} \tilde{v'} &= \tilde{v} \\ \tilde{V'} &= \tilde{V} \end{aligned} \tag{2.48}$$

With equation (2.48), also conservation of momentum is satisfied:

$$\begin{aligned} m\tilde{v'} &= m\tilde{v} \\ M\tilde{V'} &= M\tilde{V} \end{aligned} \tag{2.49}$$

As a result, from equations (2.47) and (2.49), it is deduced that the post-collision momenta are equal in magnitude and opposite in direction:

$$m\tilde{\mathbf{v}}' = -M\tilde{\mathbf{V}}' \tag{2.50}$$

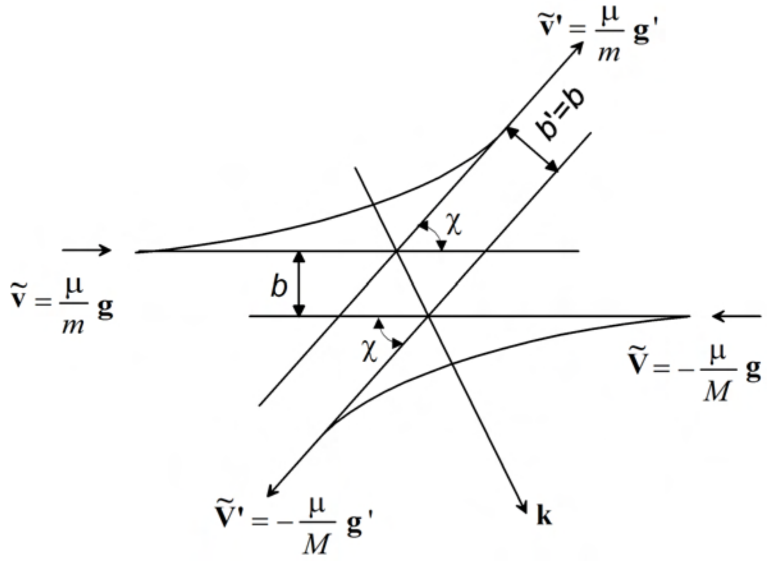

Figure 2.13: Trajectories of colliding particles in the center of mass reference frame. b denotes the impact parameter (or the distance of closest approach), and χ the deflection (or scattering) angle. The figure is adopted from [55].

With these results, conservation of energy (equation (2.48)) and conservation of momentum (equation (2.49)) in the center of mass reference frame are satisfied. Additionally, by conservation of angular momentum, the impact parameter is also unchanged after the collision, so that $b' = b$.

The calculation now reduces to finding the direction of the post-collision velocities, i.e. finding the deflection angle χ, in terms of the pre-collision velocities, the masses, and a unit vector parallel to the line of symmetry of both trajectories, vector $\mathbf{k}$, as shown in figure 2.13.

The components of momentum and hence velocity parallel to $\mathbf{k}$ (in the plane of the center of mass reference frame) are reversed, whereas the components perpendicular to **k** remain unchanged. With vector **k**, the difference between the pre- and post-collision velocities can be expressed as:

$$\begin{aligned}
\mathbf{v}' - \mathbf{v} &= \tilde{\mathbf{v}}' - \tilde{\mathbf{v}} &= -2\left(\tilde{\mathbf{v}}.\mathbf{k}\right)\mathbf{k} &= -2\frac{M}{m+M}\left(\mathbf{g}.\mathbf{k}\right)\mathbf{k} \\
\mathbf{V}' - \mathbf{V} &= \tilde{\mathbf{V}}' - \tilde{\mathbf{V}} &= -2\left(\tilde{\mathbf{V}}.\mathbf{k}\right)\mathbf{k} &= 2\frac{m}{m+M}\left(\mathbf{g}.\mathbf{k}\right)\mathbf{k}
\end{aligned} \tag{2.51}$$

where $(\mathbf{g}.\mathbf{k})$ represents the dot product of **g** and **k**, i.e. the magnitude of the vector, which is multiplied by the unit vector **k**. **k** can be divided into a component parallel to **g** (and to the center of mass plane), $\mathbf{k}_{\parallel}$ with magnitude $sin\left(\frac{\chi}{2}\right)$, and a perpendicular one, $\mathbf{k}_{\perp}$ with magnitude $cos\left(\frac{\chi}{2}\right)$. From these considerations, the following relations can be constructed:

$$\begin{aligned}
\mathbf{g}.\mathbf{k}_{\parallel} &= gsin\left(\frac{\chi}{2}\right) \\
\mathbf{k}_{\parallel} &= \frac{\mathbf{g}}{g}sin\left(\frac{\chi}{2}\right) \\
\mathbf{g}.\mathbf{k}_{\perp} &= 0
\end{aligned} \tag{2.52}$$

The first equation represents a dot product, and therefore a magnitude. Consequently, it equals the magnitude of **g**, i.e. g, multiplied by the magnitude of **k**, i.e. $sin\left(\frac{\chi}{2}\right)$. The second equation is a vector, and therefore characterized by its magnitude $sin\left(\frac{\chi}{2}\right)$, and the unit vector in the **g** direction, $\frac{\mathbf{g}}{g}$. The last equation is caused by a zero **g** in the perpendicular direction. The components of $\mathbf{k}_{\perp}$ originate from the transformation to the laboratory reference frame, and will be derived below.

With equation (2.52), the post-collision velocities (equation (2.51)) become:

$$\begin{aligned}
\mathbf{v}' &= \mathbf{v} - 2\frac{M}{m+M}sin\left(\frac{\chi}{2}\right)\left(\mathbf{g}sin\left(\frac{\chi}{2}\right) + g\mathbf{k}_{\perp}\right) \\
\mathbf{V}' &= \mathbf{V} + 2\frac{m}{m+M}sin\left(\frac{\chi}{2}\right)\left(\mathbf{g}sin\left(\frac{\chi}{2}\right) + g\mathbf{k}_{\perp}\right)
\end{aligned} \tag{2.53}$$

To return to the real laboratory reference frame, the angle φ is defined as the angle between the planes of the center of mass reference frame and the laboratory reference frame, as presented in figure 2.14.

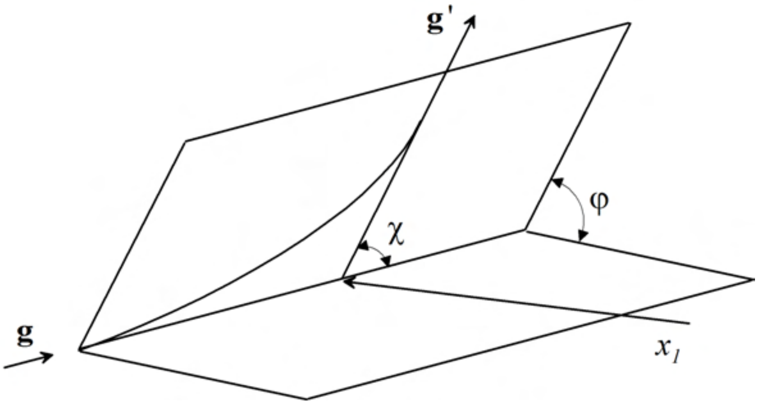

Figure 2.14: Specification of the angle, φ, between the planes of the center of mass reference frame (the plane of $\mathbf{g} - \mathbf{g}'$, i.e. the plane of figure 2.13), and the laboratory reference frame.

From geometrical considerations, the components of $\mathbf{k}_\perp$ are:

$$\begin{aligned} k_{1\perp} &= \quad cos\left(\frac{\chi}{2}\right)\sqrt{1 - g_1^2/g^2 cos\varphi} \\ k_{2\perp} &= - \quad cos\left(\frac{\chi}{2}\right)\left(\frac{g_2 g_1 cos\varphi + g g_3 sin\varphi}{g\sqrt{g^2 - g_1^2 cos\varphi}}\right) \\ k_{3\perp} &= - \quad cos\left(\frac{\chi}{2}\right)\left(\frac{g_3 g_1 cos\varphi + g g_2 sin\varphi}{g\sqrt{g^2 - g_1^2 cos\varphi}}\right) \end{aligned} \tag{2.54}$$

From equations (2.53) and (2.54), the post-collision velocities $\mathbf{v}'$ and $\mathbf{V}'$ of the colliding particles can be calculated from their pre-collision velocities $\mathbf{v}$ and $\mathbf{V}$, their masses m and M, the deflection angle χ and the angle with the laboratory reference frame φ.

The angle with the laboratory reference frame φ is arbitrary, and is therefore sampled as:

$$\varphi = 2\pi RN[0,1] \tag{2.55}$$

On the other hand, the deflection angle χ is characteristic for each type of collision. When a particle is scattered after a collision, $\mathbf{v}'$ can be found in the angle $d\Omega$, see figure 2.15.

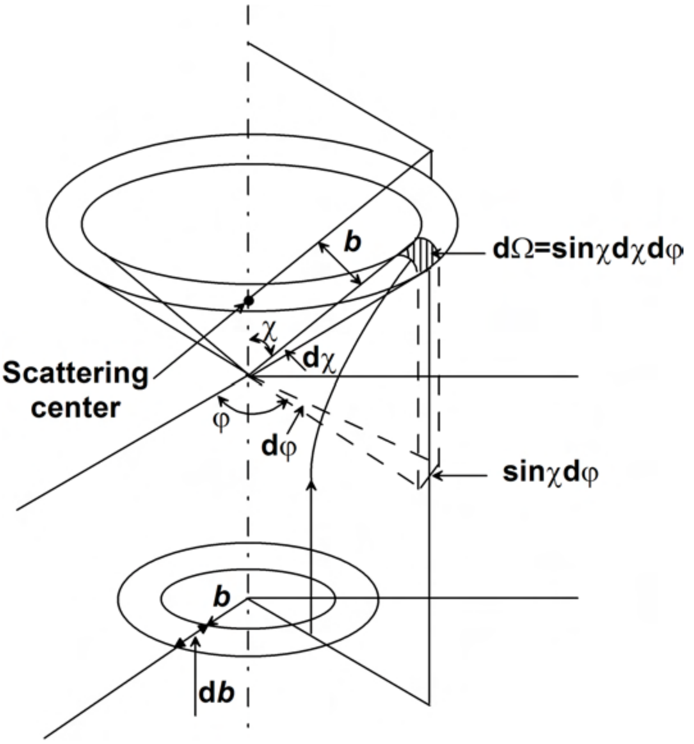

Figure 2.15: Illustration of the deflection angle χ and the impact parameter b, which cause the post-collision velocity $\mathbf{v}'$ to be found in the angle $d\Omega$. The figure is adopted from [55].

From figure 2.15, $d\Omega$ is:

$$d\Omega = sin\chi d\chi d\varphi \tag{2.56}$$

Conservation of flux F requires that all particles entering the area $2\pi bdb$ leave through this differential solid angle $2\pi sin\chi d\chi$:

$$F2\pi bdb = -F\sigma(g,\chi)2\pi sin\chi d\chi \tag{2.57}$$

The minus sign assures that an increase in b leads to a decrease in χ. $\sigma(g,\chi)$ represents the "differential cross section" which is related to χ. From equation (2.57), an expression for $\sigma(g,\chi)$ can be found:

$$\sigma(g,\chi) = -\frac{bdb}{sin\chi d\chi} \tag{2.58}$$

$\sigma(g,\chi)$ has the dimension of area (m^2) per steradian (dimensionless). It is related to the probability for collision between particles with relative velocity g, to be scattered within a solid angle $d\Omega$, given by equation (2.56). This probability is obtained by evaluation towards the "total cross section":

$$\sigma_T(g) = \int_0^{2\pi} d\varphi \int_0^{\pi} \sigma(g,\chi) sin\chi d\chi = 2\pi \int_0^{\pi} \sigma(g,\chi) sin\chi d\chi \tag{2.59}$$

So that the probability that $\mathbf{v}'$ is found in the solid angle $d\Omega$ (equation (2.56)) is given by:

$$P(g,\chi) = \frac{\sigma(g,\chi)}{\sigma_T(g)} sin\chi d\chi d\varphi \tag{2.60}$$

Consequently, the deflection angle χ can be randomly sampled by:

$$\int_0^{2\pi} d\varphi \int_0^{\chi} \frac{\sigma(g,\chi)}{\sigma_T(g)} sin\chi d\chi = \frac{2\pi}{\sigma_T(g)} \int_0^{\chi} \sigma(g,\chi) sin\chi d\chi = RN[0,1] \tag{2.61}$$

For every kind of colliding species and collision type, there exists an expression for the differential cross section $\sigma(g,\chi)$, which is derived experimentally or computationally. With this expression, the deflection angle χ can be calculated with equation (2.61). Subsequently, the post-collision velocities of the colliding particles can be derived from equations (2.53) and (2.54). In the following sections, these expressions for $\sigma(g,\chi)$ and/or the corresponding deflection angle χ, are presented for the different kinds of included collisions in the PIC/MCC model. The collisions themselves which are included in the model are presented in their corresponding chapter in part II.

Electron collisions

The interaction potential of electron collisions can be approximated by the screened Coulomb potential [56], which applies to all of the considered electron collisional events, i.e. elastic scattering, excitation, ionization, dissociation, dissociative ionization, ion pair formation, dissociative attachment, and recombination. The normalized differential cross section for screened Coulomb scattering of an electron is [56]:

$$\sigma(\epsilon,\chi) = \frac{1+8\epsilon}{4\pi\left(1+4\epsilon-4\epsilon cos\chi\right)^2} \tag{2.62}$$

where $\epsilon = E/E_h$ is the dimensionless energy, with E the electron energy ($mv^2/2$) and E_h the atomic unit of energy (1 hartree = 27.21 eV). Substituting equation (2.62) into equation (2.61), gives the deflection angle:

$$\chi = arccos\left(1 - \frac{2.RN[0,1]}{1+8\epsilon\left(1-RN[0,1]\right)}\right) \tag{2.63}$$

This equation describes the anisotropic scattering of an electron. Indeed, the deflection angle depends on ϵ, and therefore on E. Only if ϵ is very low, the scattering of the electron becomes isotropic. On the other hand, at higher ϵ, χ becomes smaller, and at the high energy limit, the electron moves more or less straight after the collision.

Combining equation (2.63) with equations (2.53), (2.54) and (2.55), the post-collision velocities can be calculated. Since the velocity of an electron is much larger than the velocity of the target atoms (Ar, Ar_m^*, Ti), ions (N_2^+, or O_2^+, O^+ and O^-) or molecules (N_2 or O_2), the velocity of the target particle $\mathbf{V}$ is assumed to be zero, so that $\mathbf{g}$ is approximated to the velocity of the electron $\mathbf{v}$.

It should be noted that for inelastic collisions, the loss of kinetic energy as internal energy of the target species has to be accounted for. In an excitation, the target particle (Ar, N_2/O_2) is excited to a higher energy level, if the energy of the incoming electron, $E_{inc} = mv^2/2$ (v the pre-collision velocity of the electron), is at least the excitation threshold energy of the target atom E_{thr}^{exc}. After the collision, the remaining energy of the electron E_{scat} is therefore $E_{inc} - E_{thr}^{exc}$. Hence, its post-collision velocity has a magnitude [57]:

$$v' = v\sqrt{1 - \frac{E_{thr}^{exc}}{E_{inc}}} \tag{2.64}$$

Let us define a vector $\mathbf{v}^*$ with magnitude v' and direction $\mathbf{v}/v$ [57]:

$$\mathbf{v}^* = \mathbf{v}\sqrt{1 - \frac{E_{thr}^{exc}}{E_{inc}}} \tag{2.65}$$

$\mathbf{v}^*$ replaces $\mathbf{v}$ in equation (2.53), and the electron is thus scattered as for elastic scattering [57] to find its post-collision velocity $\mathbf{v}'$. If the created excited atom is in the metastable state, it is followed by the PIC/MCC model, and it receives an initial velocity $\mathbf{V}'$ sampled from a Maxwellian distribution with thermal energy.

In an ionization reaction, the target particle (Ar, Ar_m^*, Ti, N_2/O_2) is ionized only if E_{inc} can overcome the required ionization threshold energy E_{thr}^{ion} of the target particle. After the collision an electron is released from the neutral species. Therefore, after the collision, the remaining energy $E_{inc} - E_{thr}^{ion}$ is divided between the incident electron (with pre-collision energy E_{inc}) and the electron which is released from the parent neutral (with energy E_{ej}). Hence, the post-collision velocity of the incident electron has a magnitude [57]:

$$v' = v\sqrt{1 - \frac{E_{thr}^{ion} + E_{ej}}{E_{inc}}} \tag{2.66}$$

A vector $\mathbf{v}^*$ is constructed with magnitude v' and direction $\mathbf{v}/v$ [57]:

$$\mathbf{v}^* = \mathbf{v}\sqrt{1 - \frac{E_{thr}^{ion} + E_{ej}}{E_{inc}}} \tag{2.67}$$

The procedure to find $\mathbf{v}'$ is the same as for excitation (see previous paragraph), i.e. $\mathbf{v}^*$ replaces $\mathbf{v}$ in equation (2.53), and the incident electron is scattered as for elastic scattering [57]. To find E_{ej}, the following consideration is made: as mentioned before, the energy $E_{inc} - E_{thr}^{ion}$ is divided between the incident electron (with pre-collision energy E_{inc}) and the electron which is released from the parent neutral (with energy E_{ej}). In general, when there was no information found in literature on the division of the energy between the original and the ejected electron, we have assumed that it is divided randomly, so that:

$$\begin{aligned} E_{ej} &= RN[0,1]\left(E_{inc} - E_{thr}^{ion}\right) \\ E_{scat} &= \left(1 - RN[0,1]\right)\left(E_{inc} - E_{thr}^{ion}\right) \end{aligned} \tag{2.68}$$

However, for the electron-impact ionization of Ar atoms, we use an expression for sampling E_{ej} by a random number, as presented in [57]:

$$E_{ej} = a_0 + a_1 \left[RN[0,1]\left(arctan\left(\frac{a_1}{b}\right) + arctan\left(\frac{a_0}{b}\right)\right) - arctan\left(\frac{a_0}{b}\right)\right] \tag{2.69}$$

with:

$$\begin{aligned} a_0 &= 2 - \frac{100}{E_{inc} + 10} \\ a_1 &= \frac{E_{inc} - E_{thr}^{ion}}{2} - a_0 \\ b &= 10.3 \end{aligned} \tag{2.70}$$

To find the direction of the velocity of the ejected electron, the ejected electron is also “scattered” onto the atom by assigning a virtual “pre-collision” velocity parallel to $\mathbf{v}$ with magnitude $v'_{ej} = \sqrt{(2E_{ej}/m)}$. $\mathbf{V}'$ is calculated as sampled from a Maxwellian distribution with thermal energy.

Dissociation (of N_2/O_2), dissociative ionization (of N_2/O_2), ion pair formation (of O_2), dissociative attachment (of O_2) and recombination (of N^+/O^+,

N_2^+/O_2^+, O^-) are treated in a similar way. Note that recombinations do not require kinetic energy. Dissociation and ion pair formation are treated as excitation, but two atoms (dissociation) or a positive and a negative ion (ion pair formation) are created from the target molecule, with Maxwellian thermal velocities. Dissociative ionization is treated as ionization, but the molecule is dissociated into an ion and an atom, which receive velocities as sampled from a Maxwellian distribution with thermal energy. In case of dissociative attachment and recombination, the incident species (the electron and, in case of recombination, the target ion) are removed from the calculation and the created species (atoms and/or negative ions in our case) obtain a velocity from a Maxwellian distribution with thermal energy.

Ion collisions

The different kinds of ion collisions included in the model are elastic scattering without charge transfer (Ar^+, Ti^+, N^+/O^+, N_2^+/O_2^+, O^-) and with charge transfer (Ar^+, N^+/O^+, N_2^+/O_2^+), excitation (Ar^+), ionization (Ar^+), and recombination (O^+, O^-). Ions are assumed to scatter isotropically, and therefore, the deflection angle is:

$$\chi = 2\pi RN[0,1] \tag{2.71}$$

The same procedure is again followed: combining equation (2.71) with equations (2.53), (2.54) and (2.55), the post-collision velocities can be calculated.

Collisions with the background gases and with atoms are considered. Since an ion moves much faster than the "motionless" background gas atoms or molecules (see also section 2.5.2 below), the velocity of the latter is assumed to be zero: $\mathbf{g}$ is then approximated to the velocity of the ion $\mathbf{v}$. However, for collisions with fast atoms, the velocity of the atoms is taken into account.

In the case of charge transfer, the charge of the ion is transferred to the neutral. Whereas elastic scattering mainly occurs at low ion energies, charge transfer occurs at higher energies [58]. Therefore, after delivering its charge, the neutralized atom moves straight with the velocity of its parent ion. The ionized target species receives a velocity, sampled from a Maxwellian velocity distribution with thermal energy and with an isotropically scattered direction.

Ion-impact excitation and ionization are treated as for electrons, i.e. the energy of the incident ion is reduced with the threshold energy needed for excitation (equation (2.64)) or ionization (equation (2.66)), respectively.

Note that certain ions can also undergo recombination reactions. In this case, the incident ion and the target species are removed from the calculation, and after isotropic scattering, the created species take the velocity from a Maxwellian distribution with thermal energy.

Atom collisions

In the model, fast atoms (Ar_f and Ti_f; moving with an energy above the thermal energy) undergo different kinds of collisions, i.e. elastic scattering, and fast-atom-impact excitation and ionization. For metastable atoms (Ar_m^*), metastable-metastable collisions, Penning ionization of sputtered Ti atoms, and two-body collisions are included. Scattering of atoms is isotropic, so the deflection angle χ is:

$$\chi = 2\pi RN[0,1] \tag{2.72}$$

The same procedure is followed again: combining equation (2.72) with equations (2.53), (2.54) and (2.55), the post-collision velocities can be calculated.

The included atom collisions occur with the background gases and with atoms. When collisions occur between fast atoms and “motionless” background gas atoms or molecules (see also section 2.5.2 below), the velocity of the latter is assumed to be zero: **g** is approximated to the velocity of the atom **v**. However, for collisions with fast target atoms, the velocity of the target atoms is taken into account.

Atom-impact excitation and ionization are treated analogous to ions and electrons: the energy of the incident atom is reduced with the threshold energy needed for excitation (equation (2.64)) or ionization (equation (2.66)), respectively.

When a metastable-metastable collision occurs, the two metastable atoms are removed from the calculation, and an electron, an Ar^+ ion, and an Ar atom, in the case that it is fast, are added. Penning ionization is treated as follows: isotropic scattering of the metastable Ar_m^* atom and the Ti atom occurs, leading to a new velocity of the created Ti^+ ion. Note that if the colliding Ti atom is fast, it was included in the model, and hence its velocity is known. If the Ti atom is slow, its velocity is sampled as a thermal Maxwellian velocity, to be used in the scattering formula. The created electron has a random velocity direction with the magnitude of the original Ti atom, if the Ti atom was fast (and hence included in the model). Otherwise the velocity of the electrons is generated from isotropic scattering onto Ti with a thermal Maxwellian velocity, similar to electron-impact excitation. The two-body collision of a metastable and a ground state atom deexcites the metastable to its ground state. However, because excess energy was transferred, a fast Ar_f atom can be created. In that case, it receives a new velocity after isotropic scattering of the parent metastable atoms.

2.4 Plasma-surface interactions

Apart from interactions among each other, particles can also interact with the reactor walls: reflection, adsorption, or the creation of new particles (such as secondary electrons and sputtered atoms) can occur. These interactions between plasma species and reactor walls is described in the *plasma-surface* *interactions algorithm.*

When a reactive gas, like nitrogen (or oxygen), is added to the argon background gas, nitrogen (or oxygen) ions can penetrate the Ti target (implantation), nitrogen (or oxygen) molecules and atoms can chemisorb at the target surface, and chemisorbed species can be knock-on implanted into the target. Subsequently, they react with the target atoms, to form a TiN_x (or TiO_x) layer [21]. This surface modification process is called "target poisoning", and influences the plasma-target interactions (i.e. sputtering and secondary electron emission), and therefore all of the plasma properties. The transition from the so-called "metallic" to "reactive or poisoned" condition happens via a hysteresis [21, 23], as was also explained in section 1.2.2 above.

In the following sections, the plasma-surface interactions included in the model are described, together with the effect of a poisoned target on the interaction.

2.4.1 Secondary electron emission

In the model, secondary electron emission occurs at the target due to the impact of ions or atoms. It is characterized by the "secondary electron emission coefficient ($SEEC$)", which describes the number of secondary electrons produced by an atom or ion hitting the cathode surface. Note that secondary electron emission at the other walls is less important, so it is not included in the model. Unfortunately, a wide range of different $SEEC$ values are reported for ion bombardement of Ti (from 0.075 [59] to 0.148 [60]). Moreover, some of these values describe the effective secondary electron yield, which is dependent on both $SEEC$ and reflection coefficent (RC) [61] (see below). Therefore, the exact $SEEC$ to be used in the model is not known. The values used in our model for the different conditions investigated will be presented in part II.

In the model, the value of the $SEEC$ is implemented as a probability for secondary electron creation. Each time an atom or ion hits the cathode surface, a random number, uniformly distributed in the interval $[0,1]$, is generated. If this random number is smaller than or equal to the $SEEC$, a secondary electron is produced. This electron starts at the position $(r,0)$ where it is created, and with an initial energy, E_e, of a few eV (we assume 4 eV in the model). With E_e, the magnitude of the initial velocity can be derived, from the expression of the average velocity:

$$v_0 = \sqrt{\frac{2.E_e.q}{m}} \tag{2.73}$$

The direction of the velocity is chosen in order to obey the cosine law [62]. As a consequence, the azimuthal angle $\phi = 2\pi.RN[0,1]$, whereas the polar angle $\theta = sin^{-1}\left(\sqrt{RN[0,1]}\right)$. Physically, the former is associated with a scattering probability function $f(\phi) = 1/(2\pi)$. In other words, the probability for scattering with an azimuthal angle of ϕ is a constant, $1/(2\pi)$. The polar angle is associated with a scattering probability function $g(\theta) = sin\,(2\theta)$, which is highest for $\theta = \pi/4$, and lowest for $\theta = 0$ and $\theta = \pi/2$. As a consequence, for emission of an electron from the cathode surface, the components of the velocity vector $\mathbf{v}$, v_r and v_θ correspond to the azimuthal angle ϕ, whereas v_z is derived from the polar angle θ. In carthesian coordinates, this can be expressed as [62]:

$$\begin{aligned} v_x &= v_0.RN[0,1].cos(2\pi.RN[0,1]) \\ v_y &= v_0.RN[0,1].sin(2\pi.RN[0,1]) \\ v_z &= v_0\sqrt{RN[0,1]} \end{aligned} \tag{2.74}$$

In cylindrical coordinates, equation (2.74) becomes:

$$\begin{aligned} v_r &= v_x cos(2\pi.RN[0,1]) + v_y sin(2\pi.RN[0,1]) \\ v_\theta &= -v_x sin(2\pi.RN[0,1]) + v_y cos(2\pi.RN[0,1]) \\ v_z &= v_0\sqrt{RN[0,1]} \end{aligned} \tag{2.75}$$

Due to target poisoning, the $SEEC$ will be altered which results in a target voltage change [61]. In the model, the effect of a poisoned target is therefore described by changing the $SEEC$ value, depending on the N_2 (or O_2) gas flow. This will be explained in detail in part II, chapters 5 and 6.

2.4.2 Electron adsorption/reflection

When an electron strikes a wall, it can be reflected or absorbed, characterized by the “reflection coefficient (RC)”. In magnetron discharges, the electron density near the cathode is much higher than at the other walls, so only interaction of electrons with the cathode surface is important. The RC is, however, hard to measure and to our knowledge, no values are reported in the literature. The RC values used in our model for the different conditions investigated will be presented in part II.

In the model, similar to the $SEEC$, the value of the RC is implemented as a probability for electron reflection. Each time an electron hits the cathode surface, a random number, uniformly distributed in the interval $[0,1]$, is generated. If this random number is smaller than or equal to the RC, the electron is reflected. This reflected electron keeps its position $(r,0)$, but its energy is partly transferred to the cathode, leaving the electron an energy E_e of 4 eV. This causes an initial velocity with magnitude as expressed by equation (2.73). The direction of the velocity $\mathbf{v}$ is chosen as such to obey the cosine law [62], and its components (v_r, v_θ, v_z) are as equation (2.75). On the other hand, if the random number is larger than the RC, the electron is adsorbed, and thus removed from the calculation.

To our knowledge, the influence of target poisoning on electron reflection has not been reported in literature. Therefore, in the model, the value of the RC is kept the same after poisoning of the target.

2.4.3 Sputtering the target

Since magnetron discharges are mainly applied as sputter devices, sputtering of the target is included in the model. This is done by calculating the sputter yield Y, each time an ion or atom hits the cathode surface. The sputter yield for an incident particle i with energy E_i is described by the empirical formula of Matsunami [63]:

$$Y\left(E_i\right) = 0.42\frac{\alpha Q K s_n\left(E_i\right)}{U_s\left(1+0.35 U_s s_e\left(E_i\right)\right)}\left[1-\left(E_{thr}/E_i\right)^{1/2}\right]^{2.8} \tag{2.76}$$

where U_s is the sublimation energy of the cathode, E_{thr} the threshold energy, and the other parameters are properties of the cathode material, as described in [63].

In the model, Y is calculated, and compared to a uniformly distributed random number in $[0,1]$. If this $RN[0,1]$ is smaller than Y, an atom is sputtered from the cathode target. If the calculated Y is larger than one, it is reduced by one after the first sputtered atom. If another generated $RN[0,1]$ is smaller than the new Y, another atom is sputtered. So it is possible that one incident particle sputters more than one target atom. This procedure is repeated until Y is smaller than one, and the newly generated $RN[0,1]$ is larger than this last value of Y. In practice, for energies of interest in our study (0-500 eV) Y of a Ti target is typically between zero and one, see figure 2.16. Therefore, in the model, the above mentioned procedure is repeated only once.

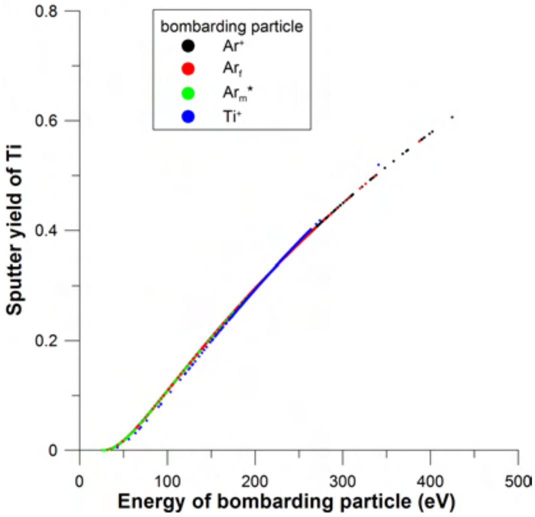

Figure 2.16: Sputter yield Y of a Ti target as a function of the energy of different bombarding species, as indicated in the legend.

The direction of the velocity of the sputtered atom is derived from the cosine distribution, i.e. its components (v_r, v_θ, v_z) are given by equation (2.75). However, the magnitude of the velocity is determined by (i) the maximum transferrable energy in an elastic collision, and (ii) the binding energy of Ti atoms [64, 65]. (i) is the maximum energy E_{max}, transferred by an elastic collision between a target atom and the incoming particle with energy E_i:

$$E_{max} = \frac{4M_i M_{sp}}{(M_i + M_{sp})^2} E_i \tag{2.77}$$

(ii) is the energy needed in order for a Ti atom to detach from the cathode surface, i.e. the sublimation energy U_s. The target atoms are assumed to be sputtered according to a cosine distribution, adapted to sputtering (i.e. taking into account (i) and (ii)) by Sigmund [64] and Thompson [65]. This leads to an expression for the energy of the sputtered atom E_{sp}:

$$E_{sp} = \frac{U_s \sqrt{RN[0,1]}}{1 - \sqrt{RN[0,1]}} \tag{2.78}$$

which is restricted by the maximum possible energy, E_{max}. This means that in the model E_{sp} is calculated and if larger than E_{max}, it is recalculated. When E_{sp} is found, the corresponding magnitude of the velocity v_0 can be calculated:

$$v_0 = \sqrt{\frac{2E_{sp}}{M_{sp}}} \tag{2.79}$$

As mentioned before, the sputtered atoms have a cosine distribution, and therefore, the direction of the velocity is determined by equation (2.75), with v_0 as defined in equation (2.79).

After the collision with the wall, the incident ion or atom is reflected or adsorbed, according to the explanation given in section 2.4.4. However, it has lost E_{sp} to the sputtered atom.

When, in the presence of a reactive gas, the target is poisoned, both Ti and N (O) atoms can be sputtered from the TiN_x (TiO_x) target. However, their sputter yield is lower than for a metallic Ti target. In the model, the sputter yields from a poisoned target are evaluated towards the sputter yield of a metallic target, calculated with equation (2.76), according to reported values [22, 66].

2.4.4 Heavy particle adsorption/reflection

Reflection

Similarly to electrons, heavy particles can also be reflected or adsorbed when hitting a wall. The probability to form a bond with the surface is described by the "sticking coefficient (*SC*)". In the model, similar to the *SEEC* and the *RC*, the value of the *SC* is implemented as follows. Each time a heavy particle hits the wall surface, its *SC* is compared to a generated random number, uniformly distributed in $[0, 1]$. If this random number is smaller than or equal to the SC, the particle is adsorbed (see next section “adsorption”), and therefore removed from the calculation. If the random number is larger, then the particle is reflected (see below).

If the SC of a species is zero, the particle is always reflected when hitting a wall. For Ar atoms, SC=0 is assumed, since Ar is an inert gas. All included ions are assumed to neutralize after reflection at the walls, which implies that they have also a zero SC. Moreover, the metastable Ar_m^* atoms are reflected as ground state Ar atoms. In other words, the reactor walls act as a loss mechanism for Ar^+ ions, Ar_m^* metastable atoms, Ti^+ ions, N^+ (O^+) ions, and N_2^+ (O_2^+) ions.

When a heavy particle is reflected, a distinction is made between elastic and inelastic reflection depending on the thermal accommodation coefficient, defined as:

$$\alpha = \frac{E_{inc} - E_{refl}}{E_{inc} - E_{wall}}, \tag{2.80}$$

where E_{inc} is the mean energy of the incoming particles, E_{refl} is the mean energy of the reflected particles, and E_{wall} is the mean energy of the reflected particles in thermal equilibrium with the wall ($2kT_w$). This means that if $E_r = E_w$, all the energy of the incoming particle is transfered to the wall, and an inelastic reflection occurred. This corresponds to α=1. However, if $E_{relf} = E_{inc}$, the energy is conserved, and an elastic reflection occurred. In this case α=0. In the simulation, α is assumed as 0.5 [52], and a random number is generated. When the random number is smaller or equal to α, an inelastic reflection occurs, and if the random number is larger than α, an elastic reflection occurs.

After an inelastic reflection, the particle is thermalized and it is removed from the simulation. This applies to all species, except for a reflected (and possibly neutralized from a Ti^+ ion) Ti atom, which is described with diffusion equations (see section 2.5.1 below). On the other hand, if the particle is elastically reflected, its energy is conserved, which causes the magnitude of the velocity to be expressed by equation (2.73). The direction of the velocity $\mathbf{v}$ is chosen in order to obey the cosine law [62], and its components (v_r, v_θ, v_z) are as equation (2.75).

Adsorption

In contrast to the above mentioned species, Ti atoms, N (O) atoms, and N_2 (O_2) molecules do have a certain probability to interact with a wall, i.e. a sticking probability, or sticking coefficient SC. In the low pressure case which we investigate, we have found that the SC does not have a great effect on the calculated species densities. Therefore, on the walls, excluding the substrate, a constant SC is assumed: 0.5 for Ti [67], 1 for N and O [22] and 0 for N_2 and O_2 (see later in sections 5 and 6).

However, to picture the deposition process of the TiN_x (or TiO_x) film on the substrate, and to predict its stoichiometry, the effective sticking coefficients, SC_{eff}, of Ti, N (O) and N_2 (O_2) are of crucial importance. These SC_{eff} values are not constant, but are affected by the incorporation or coverage of the different implanted or adsorbed species on the surface, respectively [22]. In our case, the SC_{eff} values depend on the already deposited amount of compound on the substrate, which is defined by the "compound fraction θ_{cs}": the ratio of the TiN_x (TiO_x) amount with a desired stoichiometry x, to the sum of the TiN_x (TiO_x) and the pure Ti amounts, see figure 2.17 for the case of TiO_2. In order to take this effect of changing SC upon surface coverage by compound material into account, we have coupled an analytical surface model, based on the models described in [30,31,68] to the PIC/MCC model.

The implemented analytical surface model presented here is based on the models described in [30, 31, 68], where the compound fraction on the reactor walls is calculated from the fluxes of the species (Ti, N (O), N_2 (O_2)) bombarding these walls. However, the fully analytical description in [30, 31, 68] uses assumptions to calculate particle fluxes. The advantage of coupling this analytical model to our PIC/MCC approach is that fluxes are calculated in a more accurate way, based on the detailed behavior of the species in the plasma.

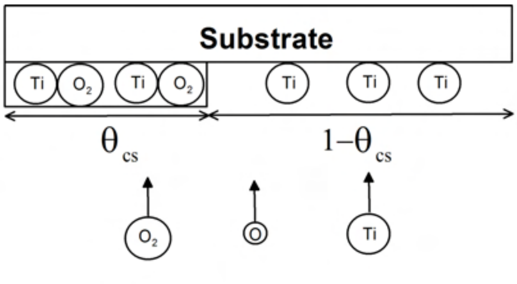

Figure 2.17: Schematic presentation of the deposited TiO_2 compound fraction on the substrate, θ_{cs}, due to the fluxes of Ti, O, and O_2.

Here, a general description is given for a A_wB_x deposited film, originating from metal A and gas B_y. Details for both N_2 and O_2 can be found in their corresponding chapters, 5 and 6. Based on the equations, presented in [30, 31, 68], a general compound fraction balance equation, for the deposition of a A_wB_x film with a desired stoichiometry x/w, is constructed:

$$\frac{y}{x}SC_{B_y}F_{B_y}(1-\theta_{cs}) + \frac{1}{x}SC_BF_B(1-\theta_{cs}) = \frac{1}{w}SC_AF_A\theta_{cs} \tag{2.81}$$

With this equation, at every PIC/MCC time step, the compound (c) fraction on every radial position on the substrate (s), i.e. θ_{cs}, is derived from the fluxes (F) of the incoming B_y, B and A species (calculated with the PIC/MCC model), with corresponding constant SC:

$$\theta_{cs} = \frac{\frac{y}{x}SC_{B_y}F_{B_y} + \frac{1}{x}SC_BF_B}{\frac{y}{x}SC_{B_y}F_{B_y} + \frac{1}{x}SC_BF_B + \frac{1}{w}SC_AF_A} \tag{2.82}$$

Subsequently, the SC values of B and B_y are adapted at that time step by the compound fraction, θ_{cs}, so that we obtain SC_{eff}, for this time step, on every position r on the substrate:

$$\begin{aligned} SC_{B_y,eff} &= SC_{B_y}(1-\theta_{cs}) \\ SC_{B,eff} &= SC_B(1-\theta_{cs}) \end{aligned} \tag{2.83}$$

Indeed, the sticking of B and B_y on compound will be lower than on a pure metallic surface. Since the sticking of metal atoms is independent from the compound fraction, a constant SC_A can be used, i.e. $SC_{A,eff} = SC_A$. Note that the actual stoichiometry (x/w) of the deposited $\mathrm{A}_w\mathrm{B}_x$ film at steady state is found by multiplying the desired stoichiometry by the compound fraction θ_{cs}. Hereby, the stoichiometry of the deposited film at different reactive gas concentrations can be predicted.

2.5 Slow neutrals

When treating the slow (thermalized) particles with the PIC/MCC method, the computation time would be tremendously high to reach a steady state. Therefore, alternative methods are used, according to the physical behavior of the species. The neutral slow particles can be subdivided into diffusing and motionless species. In the plasma, the diffusing atoms are created as slow particles, or are slowed down by collisions (Ti and N or O), and the motionless background gas atoms or molecules (Ar and N_2 or O_2) are initially slow, but can be heated.

2.5.1 Diffusing atoms

The fast Ti and N or O atoms are followed with the PIC/MCC method until they are thermalized. Afterwards, their speed is low enough to treat them as a fluid or continuum, and hence, they are excluded from the PIC/MCC method in order to reduce the computation time. They are then further described with a fluid model, since the Ti and N or O atom density is important in picturing the deposition process. Their density $n_{slow}(r, z)$ is calculated with a diffusion equation:

$$\frac{\partial n_{slow}}{\partial t} - D\Delta n_{slow}(r, z) = r_{prod}(r, z) - r_{loss}(r, z) \tag{2.84}$$

where D is the diffusion coefficient of Ti or N/O atoms in Ar gas, and r_{prod} and r_{loss} are the production and loss rates. The production of a slow Ti or N/O atom can be caused by thermalization of a fast Ti or N/O atom, or direct creation of a slow Ti or N/O atom. The loss of a slow Ti or N/O atom can be due to heating of a slow Ti or N/O atom. This will be illustrated in part II, in chapters 4, 5 and 6.

The diffusion coefficient (in m^2/s) is calculated from the rigid sphere approximation [69]:

$$D = 2.628 \times 10^{-7} \frac{\sqrt{T^3 \left(M_1 + M_2\right) / 2M_1 M_2}}{p d_{12}^2} \tag{2.85}$$

where T is the gas temperature (K), M_1 and M_2 are the masses of Ti (or N/O), and Ar (g/mol), p is the pressure (atm), and d_{12} is the collision diameter (10^{-10} m), given by $\frac{(d_1+d_2)}{2}$. The collision diameter of Ti is 2.684 $\times 10^{-10} m$ [70], 3.298 $\times 10^{-10} m$ for N [71], 3.050 $\times 10^{-10} m$ for O [71], and 3.542 $\times 10^{-10} m$ for Ar [71].

These slow atoms can be heated again by certain collisions (more details will be given in sections 5 and 6), after which they are followed again with the PIC/MCC algorithm.

2.5.2 Motionless background gases

The partial pressure of the gases p_{Ar} and p_{N_2} (p_{O_2}) is kept constant. Thermalization of fast atoms by collisions with background gas atoms or molecules can cause the background gases to heat up, i.e. the temperatures T_{Ar} and T_{N_2} (T_{O_2}) will increase. The densities of the gases n_{Ar} and n_{N_2} (n_{O_2}), which change due to gas heating, can be calculated at every position and at every time step, with the ideal gas law:

$$n = \frac{p}{k_B T} \tag{2.86}$$

k_B is the Boltzmann constant.

The flux of N_2 (O_2) is needed to calculate the deposition of the TiN_x (TiO_x) film (equation (2.82)). The amount of collisions with a surface per second (i.e. the flux) is given by:

$$F = \frac{1}{4} n v \tag{2.87}$$

The speed v is the average speed of the gas molecules, i.e. thermal speed:

$$v = \sqrt{\frac{2.k_B.T}{m}} \tag{2.88}$$

T is the gas temperature, and m the mass of an N_2 (O_2) molecule.

2.6 Stability of the calculations

The particle-in-cell method calculates in a discrete manner, in both time and space, continuous plasma characteristics. Moreover, the limited number of superparticles decreases the amount of reachable values in the domain of the calculated physical quantities. This approach is performed to solve continuous differential equations numerically, and for speeding up the calculations (see also section 2.7), but it can cause numerical instabilities such as noise or heating. The discrete factors in the model are (i) the limited number of superparticles, (ii) the time step, and (iii) the grid size. If the number of SPs approached the real number of particles, and if the time step and the grid size decreaseed in the limit to zero, the numerical noise would be eliminated.

The number of SPs, representing W (weight factor) real particles, needs to be small enough to have workable computation times, but must be large enough to have sufficient statistics. To our knowledge, there exist no criteria for this, making it a matter of trial-and-error. In our calculations, weight factors in the order of $10^6 - 10^8$ were used.

The time step must be large enough to limit the computation time, but must be small enough to eliminate numerical noise. In our PIC model, the discrete leap-frog integrator is implemented to solve Newtons' equations. To test its stability limitations, the leap-frog integrator is applied to the simple 1D harmonic oscillator case (which is justified knowing that a plasma also oscillates with a certain plasma frequency ω_0). In [36, 37, 52, 55] it is shown that the "stability criterion" can be constructed:

$$\omega_0 \Delta t \leq 0.2 \tag{2.89}$$

In a plasma the electron frequency ω_e is the highest frequency, so this is used in the stability criterion for ω_0. Moreover, based on equation (2.89) and on the considerations made in [72], we chose a value of 0.162 in our model (instead of 0.2). All together, the stability criterion in our model is:

$$\omega_e \Delta t_e = \sqrt{\frac{n_e q_e^2}{\epsilon_0 m_e}} \Delta t_e \leq 0.162 \tag{2.90}$$

with Δt_e the electron time step, n_e the maximum electron density, q_e the elementary electron charge and m_e its mass, and ϵ_0 the permittivity of vacuum.

With a time step dependent on equation (2.90), *the grid* must be large enough to avoid particles to jump over grid cells, causing an unphysical accumulation of kinetic energy, leading to numerical heating. This phenomenon is most important in the direction of the strongest electric field gradient, in our case the z-direction, with grid cell dimension Δz. This restriction is summarized in the "Courant criterion" [73]:

$$\frac{v_k \Delta t_k}{\Delta z} \leq 1 \tag{2.91}$$

Here, v_k is the velocity of the k^{th} type of superparticles, and Δt_k its time step.

On the other hand, the grid must be fine enough to limit numerical noise, and therefore a characteristic length, the Debye length λ_D, is used:

$$\lambda_D = \sqrt{\frac{\epsilon_0 k_B T_e}{n_e q_e^2}} \tag{2.92}$$

The Debye length defines the distance over which an electric field is shielded, hence not "felt" anymore by other charged particles. Therefore the upper limit for the grid size is:

$$\Delta z \leq \lambda_D \tag{2.93}$$

2.7 Speeding up the calculations

As already mentioned a few times, PIC/MCC calculations suffer from long calculation times, mainly due to a large number of simulated particles during a large number of succesive time steps, where all plasma properties are calculated self-consistently. Therefore, a few numerical methods are applied to shorten the calculation time. As already put forward, the real particles are represented by a limited ensemble of superparticles. Also, the field properties are not calculated on the particles, but on a limited number of grid nodes. However, there exist some additional numerical "tricks" to speed up the PIC/MCC calculations, summarized here.

First of all, *the weight W of the SPs*, which represents the number of real particles comprised in one SP, is different for different types of SPs. Neutrals have a much higher density, so its W is set higher to save computation time. This is justified because the higher the density, the lower the statistical noise. In a PIC simulation, implementing different W factors is straightforward. However, in the MCC module, one should take care about the particle balance. When a SP collides with another SP with the same W or with the background gas, no additional precaution needs to be made. However, when SPs with different W factors collide, the particle conservation law must be obeyed. Imagine a collision between SPs A and B with velocities $\mathbf{v_A}$ and $\mathbf{v_B}$, and different weights W_A and W_B, respectively. When A is the incident and B the target species, a correction factor has to be included in the probability that A and B collide (see also equation (2.44)):

$$P_{A,B} = 1 - \exp\left(-\frac{W_B}{max\left(W_A, W_B\right)}\Delta t \cdot n_B \cdot v_A \cdot \sigma_{AB}\left(E_A\right)\right) \tag{2.94}$$

Otherwise, when B is the incident and A the target species, another correction factor must be included in the probability that B collides with A:

$$P_{B,A} = 1 - \exp\left(-\frac{W_A}{max\left(W_A, W_B\right)}\Delta t \cdot n_A \cdot v_B \cdot \sigma_{AB}\left(E_B\right)\right) \tag{2.95}$$

This different probability for the same collisional event is more easy to understand, noting that the probabilities correspond to collisions between imaginary SPs. When considering for example a collision of a SP A that consists of five real A particles with a SP B that consists of three real B particles, only (maximum) three real A particles are able to collide with three real B particles. Therefore the probability of collision of A with B has to take into account a factor of 3/5.

As a consequence, only the real particles that collide receive post-collision velocities $\mathbf{v'_A}$ and $\mathbf{v'_B}$. Therefore, the assignment of post-collision velocities occurs with probabilities of $\frac{W_B}{max\left(W_A, W_B\right)}$ and $\frac{W_A}{max\left(W_A, W_B\right)}$, for a collision of A with B and B with A, respectively.

A second method to speed up the PIC/MCC calculation comprises *the number of SPs*. The initial number of SPs will grow during the simulation as a consequence of the plasma collisions. If the number of SPs of a certain type of particle increases above a predefined number, then this value is divided by two, and correspondingly, its weight W is multiplied by two. In order to obey charge conservation, it is important that all charged particles' SP number is handled.

A third speeding up method is the application of *the sorting algorithm*. Shortly explained, the location of a SP in its array corresponds to its real location in space. The advantage is that when looking for SPs lying close to each other, they are very quickly found. The details of this procedure are given in [52, 74].

A fourth procedure optimizes *the time step*. Since particles with very different characteristic velocities are simulated, their speed can be a measure for their time step. In that view, electrons have a smaller time step than ions and neutrals. This method is called "subcycling". Additionally, the time step in the model is variable dependent on the particles' densities. In the beginning of the simulation, the densities are lower, so the time step can be larger. The time step is checked (for example every 5000 time steps) to fulfill the stability criterion (equation (2.90)), and if not, the time step is reduced (multiplied by 0.75).

Finally, the PIC/MCC simulation usually starts from uniformly distributed particle densities. When the plasma is generated (i.e. when the simulation is started), the particle density distributions evolve to their equilibrium states. If we start the simulation with these *improved density profiles*, i.e. density profiles that are closer to the equilibrium values, the calculation time to reach steady state will noticeably be shortened. This is done by starting a new calculation, with for example different discharge conditions, from another already converged simulation.

Part II

Results

Chapter 3

Pure Ar: the importance of including an external circuit

3.1 Introduction

A plasma can be generated by applying an "external voltage, V_{ext}", to the cathode, as presented in figure 2.1 above, which breaks down the gas into a partially ionized plasma. The formation of charged particles induces a current to flow in the plasma. This current grows, and advances through different current regimes, until it tends to infinity [51]; the different regimes were explained and plotted in figure 2.6 above. Logically every regime has its own discharge characteristics.

However, a resistor is required to limit the current into a certain desired regime, by obeing Kirchhoffs law, embodied in the load line, see figure 2.6. Without an "external resistance, R_{ext}", the cathode current may converge to a wrong volt-ampere regime, but more often the current will become infinitly high. The resistor is in the simplest way, a constant resistance, and is connected to the voltage source and the cathode, as presented in figure 2.1 above.

It is clear that a current-limiting resistor is necessary in experimental setups.

However, also in models, this “external circuit” limits the current to the desired regime, and is therefore inevitable for an accurate calculation of the current and voltage, and hence a correct prediction of the plasma characteristics. In the existing PIC/MCC models for DC discharges a current-limiting device is often neglected (among which in magnetrons [44–46]). In [44, 46], nothing is mentioned about convergence of the cathode current at all, and in [45], the authors conquered convergence problems which they solved by trial and error of different input parameters such as voltage, pressure and secondary electron emission coefficient. In both cases, the cathode current was not verified with experimental values.

The overall principle of coupling an external circuit to the PIC/MCC model is given in [36]. Verboncoeur et al. [75] and Lawson [76] treated the general 1D case, and van der Straaten [42] treated the 1D case applied to a cylindrical magnetron. Vahedi et al. studied the general 2D Cartesian case [49, 50]. However, there exists no PIC/MCC model yet in 2D cylindrical geometry with external circuit included, beside the model used in our work, developed by Kolev et al. [32, 37–39].

In part I section 2.2.3 it was explained how this external circuit was implemented. This implementation was based on the above mentioned research, but the necessary modifications were done for the 2D cylindrical geometry [32, 37–39]. In our work, we have studied in detail the effect of the external circuit in an Ar magnetron discharge, before extending the model to an Ar/N_2 and an Ar/O_2 discharge, in order to make sure our calculated results could be verified with experiments. Therefore, in the present chapter, when including an external circuit, two regimes were studied in the magnetron, namely the “normal glow discharge” and the “abnormal glow discharge” regime. As mentioned before, only calculations with external circiut can bring the discharge into the desired regime. Furthermore, the importance of including an external circuit in a PIC/MCC DC magnetron code is investigated by comparing it with results when an external circuit is not included.

3.2 Description of the magnetron discharge and simulated conditions

To enable validation of our modeling results with experiments, a real magnetron setup from Ghent University [77] is simulated. This device is a planar circular magnetron, on which a 25 mm radius Ti target (3 mm thick and with 99.995% purity, Lesker) was clampled. The magnets placed behind the cathode have a remanent magnetic field of 13500 Gauss, generating a magnetic field with a maximum radial strength, B_r, of 1040 Gauss. The dimensions of the magnets were chosen in such a way that the area of the outer magnet ring was three times higher than the area of the inner magnet cylinder. Corresponding to the classification of Window and Savvides this magnet configuration corresponds to an almost balanced type II magnetron [78]. The scheme of the simulated magnetron discharge was presented earlier, in figure 2.1.

The magnetron discharge operates in pure argon gas at 300 K, at a pressure of 1 Pa. The used electrical quantities (voltage, resistance, current) are mentioned in the corresponding results sections below.

3.3 Overview of the model

The model is described in detail in part I chapter 2, i.e. the particle movement is simulated with the particle-in-cell method (section 2.2). The collisions are treated with the Monte Carlo collisions module (section 2.3), and are listed below (section 3.4). Plasma-surface interactions, i.e. secondary electron emission, electron adsorption/reflection, and Ar^+ ion adsorption/reflection (the latter followed by neutralization) are accounted for (section 2.4). The surface coefficients, $SEEC$ and RC, used in our model are mentioned in the corresponding results sections.

3.4 Included collisions

In this chapter, a discharge in pure Ar gas is evaluated. Here, only electrons, Ar^+ ions, and Ar background gas are included in the model. The metastable Ar_m^* atoms, fast Ar atoms and sputtered Ti atoms were not taken into account since their contribution to the present problem is not important. Indeed, we want to investigate the influence of the external circuit on the cathode current, which is only dependent on charged particles. Also, the contribution of the ionised sputtered particles is not very significant to the charge density [38]. The list of the considered collisions and references to their corresponding cross sections is given in table 3.1.

Table 3.1: List of the collisions considered in the model. The references where the cross sections ($\sigma(E)$) were adopted from are presented in the last column.

e^- collisions				
(1)	$e^- + Ar \rightarrow e^- + Ar$	elastic scattering	$\sigma(E)$	[79]
(2)	$e^- + Ar \rightarrow 2e^- + Ar^+$	electron-impact ionization	$\sigma(E)$	[80]
(3)	$e^- + Ar \rightarrow e^- + Ar_m^*$	electron-impact excitation	$\sigma(E)$	[81]
(4)	$e^- + Ar \rightarrow e^- + Ar^*$	electron-impact excitation	$\sigma(E)$	[82]
Ar^+ collisions				
(5)	$Ar^+ + Ar \rightarrow Ar^+ + Ar$	elastic scattering	$\sigma(E)$	[58]
(6)	$Ar^+ + Ar \rightarrow Ar + Ar^+$	charge transfer	$\sigma(E)$	[58]
(7)	$Ar^+ + Ar \rightarrow 2Ar^+ + e^-$	ion-impact ionization	$\sigma(E)$	[83]
(8)	$Ar^+ + Ar \rightarrow Ar^+ + Ar_m^*$	ion-impact excitation	$\sigma(E)$	[83]

These cross sections are plotted below, in figure 3.1.

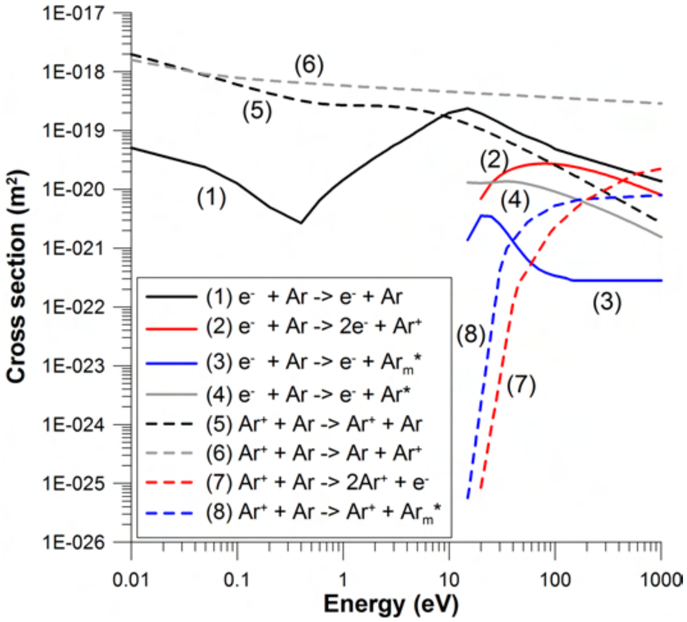

Figure 3.1: Cross section data of the electron and Ar^+ ion collisions, included in the model. The references where this data is adopted from are given in table 3.1.

3.5 Results and discussion

3.5.1 The "normal glow discharge" regime

In order for the discharge to operate in the normal glow discharge regime, the external voltage must be low and the external resistance high (see figure 2.6 above). The following input values were used for the external potential, external resistance, gas pressure, RC and $SEEC$: -400 V, 1500 Ω, 1.0 Pa, 0.1 and 0.07. The calculations are run until convergence of the cathode potential, typically after around 15 μs. The cathode potential at steady state of the plasma was calculated to be -272 V. The cathode current was calculated as 0.086 A, which corresponds to regime D-E on figure 2.6.

We have studied the effect of the cathode current on the discharge characteristics in this normal glow discharge regime. This was achieved by varying the external resistance. The following values were used: 1500 Ω, 2000 Ω and

2500 Ω.

When the resistance is increased, the external current decreases, causing also a drop of the cathode current. The calculated cathode currents for the given resistances are 0.086 A, 0.063 A and 0.048 A, respectively. These currents also correspond to the D-E regime at figure 2.6, what causes the cathode potential to be nearly constant. Indeed, the calculated values for the cathode potential for the given resistances are -272 V, -274 V and -281 V, respectively. The small increase in cathode potential could refer to an area of slightly negative differential resistance, causing the voltage drop $R_{ext}I_{ext}$ to decrease with increasing resistance. From equation (2.12), it is clear that this causes the cathode potential to increase (i.e. become more negative). Indeed, at the low current regime, the secondary electrons play the most important role in sustaining the discharge. These secondary electrons can return to the cathode in their magnetic traps. In this way, they provide a more negative charge for the cathode, and as a result, the cathode potential will increase slightly (i.e. become more negative).

3.5.2 The "abnormal glow discharge" regime

Because most magnetron experiments operate at higher currents (typically 0.1 - 1 A [84]), i.e. regime E-F on figure 2.6, we have adjusted the above mentioned input to force the cathode current into the abnormal regime. This allows us to verify the calculation with experimental values [85]. To reach this regime, the external voltage is increased and the external resistance is decreased so that the load line shifts to a higher limiting current.

The input values used were an external potential of -468.7 V and a gas pressure of 1.0 Pa [85]. To study the effect of the cathode current, the external resistance was varied over 500 Ω, 200 Ω and 100 Ω.

To verify the calculated results, we have compared them with experimental data, performed by Heirwegh [85], as shown in table 3.2. For the above mentioned values of the external resistance, a *RC* of 0.3, and a *SEEC* of 0.07 were used to obtain the calculated values for the cathode current and potential, as summarized in table 3.2 as well.

Table 3.2: Measured and calculated values of the cathode currents and corresponding potentials for a pressure of 1.0 Pa.

Measured		Calculated	
Current (A)	Potential (V)	Current (A)	Potential (V)
0.2	-336.4	0.35	-310
0.4	-382.5	0.43	-385
0.6	-405.1	0.50	-415

From table 3.2, we can conclude that a reasonable agreement is reached between the calculations and the experimental values. A higher cathode potential results in a higher current, as expected. Therefore, all the other calculated plasma characteristics, such as charged particle fluxes and densities, and plasma potential distribution, which are relatively hard to measure, are likely to be realistic as well.

The trends of the calculated currents and potentials are also manifested in the particle fluxes. An increased resistance, leading to a lower current and potential, causes a decrease in the particle fluxes, as shown in figure 3.2 below. The characteristic profile of the charged particle fluxes is caused by the magnetic field that traps the electrons near the cathode. Indeed, at a radial position of 13.5 mm, the radial magnetic field is highest (see figure 2.1 above), which leads to a trapping of the electrons. Therefore, the electrons cause most ionizations here, leading to a maximum ion density close to the cathode. This causes the maximum of the fluxes to be situated here as well. However, a slight shift of the maximum of the electron flux can be noticed, but it is considered as not significant. Obviously, the ion flux is an order of magnitude larger than the electron flux, because the electric field causes an attraction of ions and a repulsion of electrons, leading to a lower electron flux compared to the ion flux. This ion flux causes the typical race track area on the cathode surface of a magnetron discharge, i.e. the region where most particles are sputtered from the cathode.

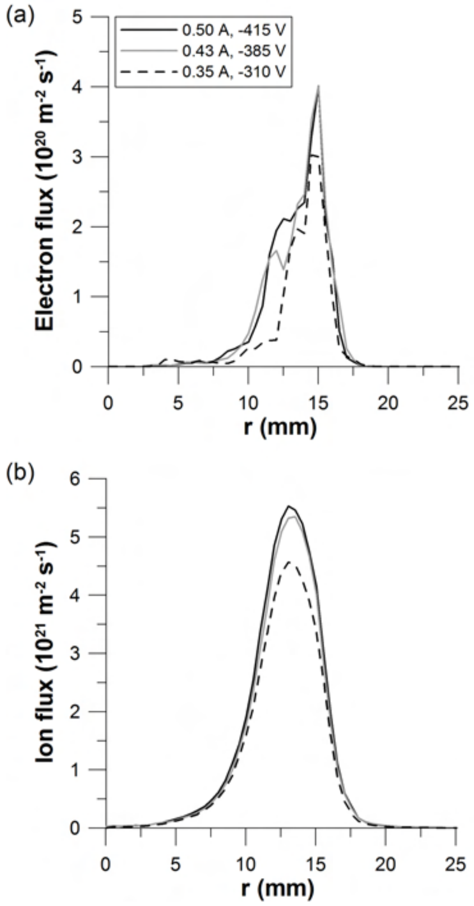

Figure 3.2: Calculated electron fluxes (a) and Ar^+ fluxes (b) to the cathode as a function of radial position. The pressure is kept constant at 1.0 Pa and three different values of cathode current and potential in the "abnormal glow discharge" regime were calculated self-consistently, as shown in the legend. Note that the y-axis (r=0) corresponds to the symmetry axis of the cilindrically symmetrical reactor.

The lower current causes the charged particle densities to decrease as well, as is seen in figure 3.3, where the electron density is presented. The ion density is similar, so is not shown here. The electrons and ions are well localized near the cathode. As mentioned before, this is a consequence of the magnetic field and the resulting enhanced ionization.

(a) 0.50 A / -415 V

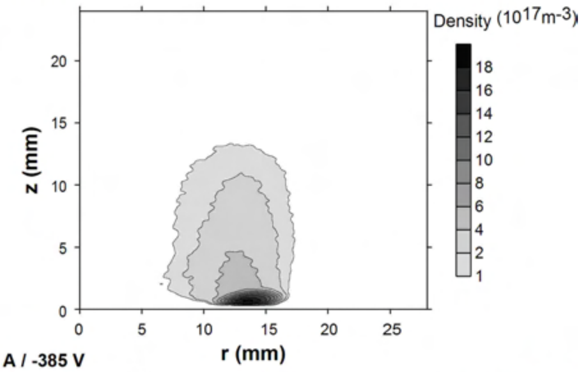

(b) 0.43 A / -385 V

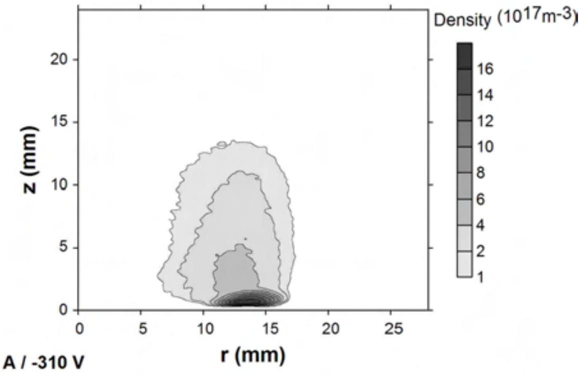

(c) 0.35 A / -310 V

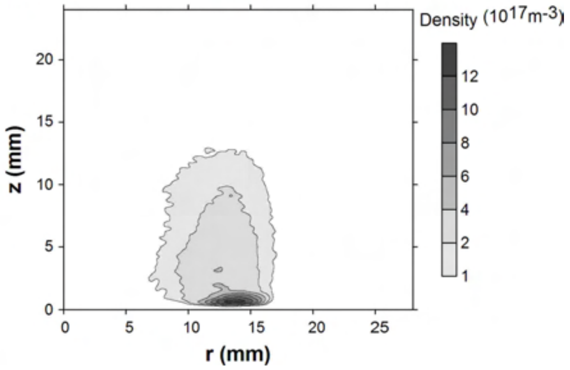

Figure 3.3: Calculated electron density profiles at a constant pressure of 1.0 Pa and three different values of cathode potential and current in the "abnormal glow discharge" regime. Note that the y-axis (r=0) corresponds to the symmetry axis of the cilindrically symmetrical reactor.

It is obvious that there are great differences between the normal and abnormal glow discharge regime. Besides the difference in potential-current dependence, the abnormal regime operates at higher currents, causing all the other plasma characteristics, for example charged particle fluxes and densities, to be larger. Indeed, the charged particle fluxes and densities in the abnormal regime were calculated to be almost one order of magnitude larger than in the normal regime.

3.5.3 Comparison with and without external circuit

To investigate the importance of the external circuit in our calculations, we have carried out a comparison of the model with and without external circuit.

When working without an external circuit, it appears that an appropriate choice of the input values such as pressure, electrical potential and current, RC and $SEEC$ is very important to avoid either divergence of the cathode current or a zero cathode current. Calculations were performed for pressures in the range of 0.4 to 1.0 Pa, and potentials received from Heirwegh [85], but only a limited number of combinations yielded converged results. From the difficulty to reach convergence, it is obvious that a simulation without external circuit is very sensitive to changes of any input value in terms of stability of the code. In contrast, the stability of the code in simulations with external circuit included is not at all sensitive to changing the input values. That is one reason why an external circuit is inevitable in a PIC/MCC simulation of every kind of discharge, among which magnetron discharges.

Another reason is that in the rare case that a calculation without external circuit converges, the results are not at all reliable, because the calculated current is either zero or is a few orders of magnitude too low. This will be shown in this section.

The “normal glow discharge” regime

For a typical input set of the normal glow discharge regime, namely a pressure of 1.0 Pa, an external potential of -400 V, an external resistance of 1500 Ω, a *RC* of 0.1, and a *SEEC* of 0.07, the cathode potential at steady state of the plasma was calculated to be -272 V in the model with external circuit included (see section 3.5.1 above). To emphasize the importance of the external circuit, attempts were made to compare the results of a simulation with external circuit to those without external circuit. In order for this comparison to be meaningfull, the cathode potential of this converged simulation should be used as input for the calculation without external circuit, instead of calculating it self-consistently when working with an external resistance and potential, as explained in section 2.2.3. Using the cathode potential as input is the common procedure when neglecting the external circuit to study the plasma quantities (e.g. [44–46]).

Unfortunately, the calculated cathode potential of -272 V appeared too low to get convergence in the model without external circuit: the cathode current became zero (i.e. the discharge extinguishes), whereas the cathode current with external circuit was calculated as 0.086 A (see section 3.5.1). This implies that an external circuit is necessary in a PIC/MCC simulation, because using the same input values but omitting an external circuit leads to a different result than with external circuit, namely to a zero cathode current.

The “abnormal glow discharge” regime

For a typical input set of the abnormal glow discharge regime, namely a pressure of 1.0 Pa, an external potential of -468.7 V, an external resistance of 200 Ω, a *RC* of 0.3 and a *SEEC* of 0.07, the cathode potential at steady state of the plasma was calculated to be -385 V (see section 3.5.2 above). This cathode potential is again used as input for the calculation without external circuit in order to be able to compare the results.

As seen in section 3.5.2, the measured cathode current for the above mentioned input values is 0.4 A. Hence, there is a good agreement with the calculated value of 0.43 A. The cathode current, calculated with the same input values in a code without external circuit, however, was calculated as

0.008 A. This means that neglecting an external circuit causes the cathode current to converge to a value which is almost two orders of magnitude too low.

Figure 3.4 illustrates the calculated charged particle fluxes with and without external circuit included. It is clear that the fluxes are a few orders of magnitude lower without than with external circuit.

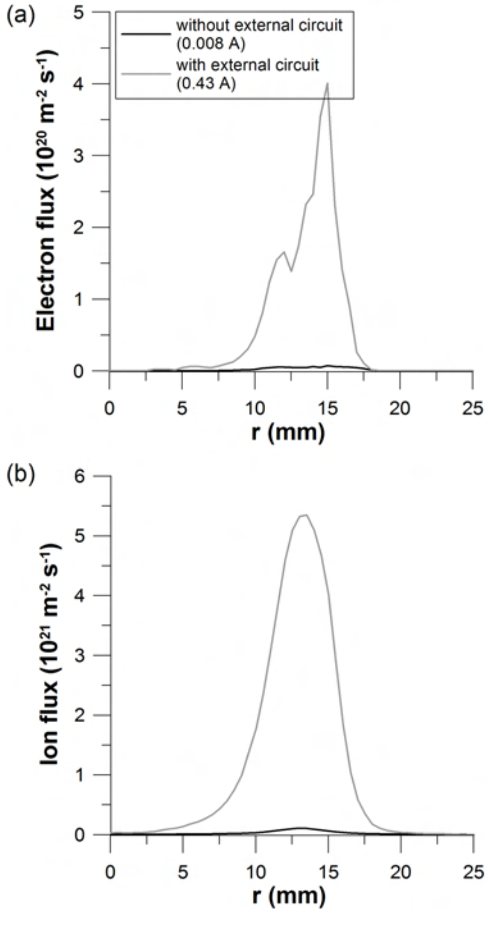

Figure 3.4: Calculated electron fluxes (a) and Ar^+ fluxes (b) at the cathode as a function of radial position, and at a constant pressure of 1.0 Pa, obtained with and without including the external circuit. Note that the y-axis (r=0) corresponds to the symmetry axis of the cilindrically symmetrical reactor.

The charged particle densities follow this trend, as shown in figure 3.5, for the electron density. The calculated electron density with external circuit is not only two orders of magnitude larger, but the profile is also totally different, i.e. the maximum of the electron density is located closer to the cathode. This is because the sheath narrows when an external circuit is included, presented in figure 3.6. Indeed, because of the higher electron density, more ionization takes place, so that the sheath can be thinner to sustain the discharge.

(a) Without external circuit (0.008 A)

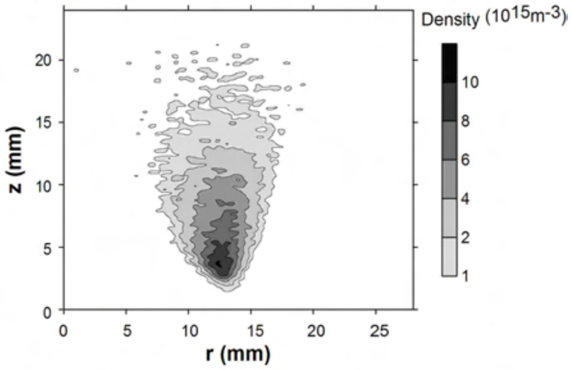

(b) With external circuit (0.43 A)

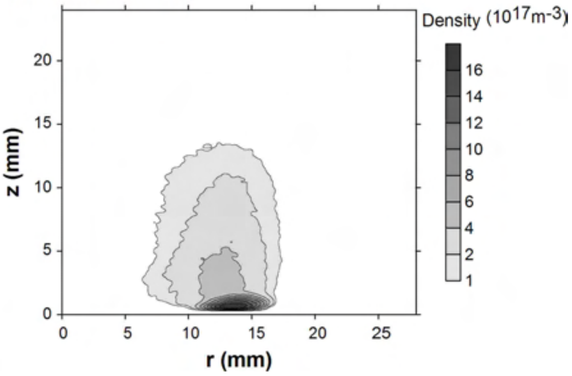

Figure 3.5: Calculated electron density profiles at a constant pressure of 1.0 Pa obtained with and without including the external circuit. Note that the y-axis (r=0) corresponds to the symmetry axis of the cilindrically symmetrical reactor.

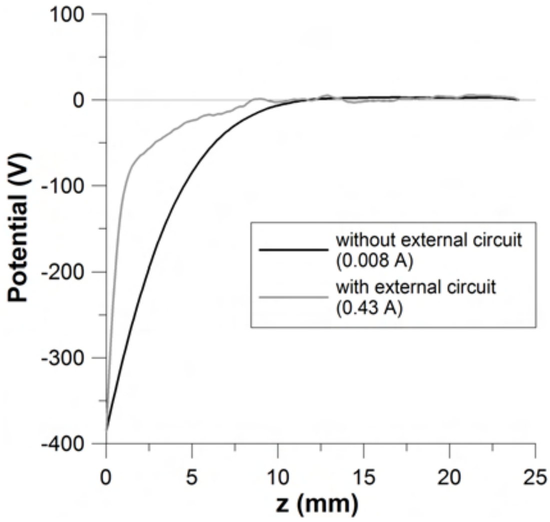

Figure 3.6: Calculated potential distribution at a line above the race track (i.e. $r = 13.5$ mm) at a constant pressure of 1.0 Pa obtained with and without including the external circuit.

The large differences in plasma characteristics are a direct consequence of the wrong calculated current when an external circuit is neglected.

3.6 Conclusion

A plasma can be formed in many different current-voltage ($I - V$) regimes, and all of them have their own plasma characteristics. An external circuit can force the discharge into a certain regime by modifying the external voltage and resistance. This was demonstrated by calculations for a "normal glow discharge" and an "abnormal glow discharge" regime of a DC magnetron discharge. The calculated results from the "abnormal" regime were validated with experiment [85].

In a model without external circuit, on the other hand, the calculated current will not be limited, leading to stability problems, or, in a small number of cases, to a converged current, which is most likely in a wrong $I - V$ regime. We have shown that the calculated current is indeed a few orders of magnitude too low when neglecting the external circuit, causing the calculated plasma characteristics to be too low. The overall conclusion is that an external circuit is inevitable in a PIC/MCC code for an accurate and correct description of magnetron discharges, and in general, of all DC glow discharges.

Chapter 4

Pure Ar: dependence of the magnetic field strength

4.1 Introduction

The presence of charged particles with very different masses (electrons and ions), and therefore different mobilities, causes a redistribution of these particles in the discharge area. As a consequence of their higher mobility, electrons are rapidly lost to the walls while the ions remain in the discharge. Therefore, the walls charge negatively, creating a positively charged bulk plasma. The region in front of the wall is called the “sheath”, and is characterized by a decreasing potential from the (positive) plasma to the (negative) wall.

Due to the negative applied potential on the cathode, the sheath in front of the cathode is the most distinct. Indeed, the whole potential difference is passed through in this small area. As a result, the ions which enter the cathode sheath are accelerated to the cathode target, leading to sputtering, which is the main application of magnetron discharges. Therefore, the cathode sheath region is the most important area of the magnetron discharge. Consequently, its structure will undoubtfully influence the sputter deposition process. Therefore, a good understanding is necessary in order to optimize the applications of magnetron sputter deposition.

In spite of its importance, the sheath is also the most complicated and uncomprehended area in (magnetron) discharges. The sheath consists of three different regions [86], i.e. the electron-free ion sheath, the Debye sheath where the electron density rises but stays lower than the ion density, and the presheath, which consists of equal electron and ion densities, but the potential decreases towards the sheath so the ions can accelerate to reach the Bohm velocity [86]. The magnetic field strength determines the structure of the sheath area, but there is uncertainty about which part of the sheath is affected by magnetic field variations [2].

Magnetrons with small magnetic fields have sheath widths comparable to non-magnetized plasmas. Indeed, for low magnetic fields, the Larmor radius (see section 1.2.1, and equation (1.1)) of the electrons is considerably larger than the sheath width, indicating that the electrons spend most of their trajectories in the bulk, as in the case of a non-magnetized plasma. As a consequence, if the magnetic field is increased, the ion density increases, leading to a decrease in sheath thickness. This decrease of sheath thickness with increasing the magnetic field for a low magnetic field strength is published frequently, based both on experimental [25, 87, 88] and on computational [43, 89, 90] studies.

However, if a magnetic field of considerable strength is applied so that the Larmor radius of the electrons is comparable to the sheath width, the electrons are trapped in the sheath, and will have a restricted mobility. This causes the cathode sheath area to be considerably different than in a non-magnetized glow discharge. Indeed, a so-called “thick sheath” is formed, with a rising width when increasing the magnetic field. Wendt and Lieberman [28] have found evidence for these thick sheaths: by comparing the erosion profile from a model using a thin sheath and a model using a thick sheath description, the thick sheath model yielded better agreement with experiment. Lister [91] used a 1D fluid model which takes into account the electron current in the sheath, to describe the effect of a constant magnetic field on the sheath. When the magnetic field is high enough, an increase of the sheath width was found with rising magnetic field. Measurements of Yeom [84] also confirm the increase in sheath thickness when increasing the magnetic field, in the case of strong magnetic fields. However, the model of Lister predicts that for magnetic fields lower than 400 G, i.e. low magnetic fields, the magnetic field strength seemed to have no influence on the sheath width, which is in contrast with experimental and computational results, mentioned before [25, 43, 87–90]. The model of Lister was therefore improved by Bradley and Lister [90], using a better approach for the interface of the sheath and pre-sheath area, i.e. a smooth integration through all the sheath areas. The pre-sheath is a term the authors use to define the sheath area where the electrons are trapped by the magnetic field and hence the ionization takes place. They found that with a low magnetic field the sheath thickness decreases when increasing the magnetic field, both in the case of a constant (maximum 100 G) and an axially variable (the maximum varies axially from 200 - 50 G) magnetic field, confirming the above mentioned trend for the case of a low applied magnetic field.

Both Lister [91] and Bradley et al. [90] state that their 1D fluid model needs further validation by a 2D particle model in order to cover the whole pressure range [91] and to overcome the used assumptions [90,91]. Also, a 2D geometry can give information about the radial structure of the sheath, and can allow more complex magnetic fields [90]. Therefore, in the present chapter, the cathode sheath structure and its dependence on the magnetic field is studied using a 2D PIC/MCC model.

Kondo et al. [43] and Nanbu et al. [89] have modeled a magnetron discharge using a 3D PIC/MCC model. However, these particle models do not cover the whole magnetic field range, but they only describe the case of low magnetic fields [43, 89]. Therefore, only a decrease in sheath thickness with increasing the magnetic field is reported, which corresponds to the results of a low applied magnetic field. Also, the models in [43,89] do not include an external circuit, which occurs to be inevitable in a PIC/MCC code, see chapter 3. Also, sputtering is not accounted for in [43, 89].

Therefore, in this chapter, the cathode sheath structure and its dependence on the magnetic field strength is studied. This allows us to gain additional insight in the underlying physical mechanisms of the sheath area and all of its regions (ion sheath, Debye sheath and pre-sheath). Also, the effect of the magnetic field strength on the sputter deposition process is investigated.

4.2 Description of the magnetron discharge and simulated conditions

The simulated magnetron discharge in this chapter is the same as in the previous chapter, see section 3.2. The scheme of the simulated magnetron discharge was presented in figure 2.1.

The magnetron discharge operates in 1 Pa Ar gas, at 300 K. The external voltage and resistance, V_{ext} and R_{ext}, are -600 V and 2000 Ω, from which the cathode current and voltage, I and V_0, are calculated self-consistently.

To study the effect of the magnetic field strength, the B_r and B_z values of the magnetic field with maximum B_r of 1040 G, are multiplied by factors of 0.5, 0.55, 0.6, 0.7, 1.5, and 2.5, leading to maximum radial field strengths, of 520 G, 570 G, 620 G, 730 G, 1560 G, and 2600 G, respectively. Due to this applied non-uniform magnetic field (see figure 2.1), the particle densities in the plasma will have a non-uniform distribution. Therefore, the sheath will also be non-uniform, being thinnest at the radial position correspondig to the maximum radial magnetic field. The term “sheath width” refers to the point where the plasma is the most intense and the sheath the thinnest, i.e. above the race track ($r = 13.5$ mm).

4.3 Overview of the model

The model is described in detail in chapter 2, i.e. the particle movement is simulated with the particle-in-cell method (section 2.2), except for the slow Ti atoms (section 2.5). The collisions are treated with the Monte Carlo collisions module (section 2.3), and are listed below (section 4.4). Plasma-surface interactions, i.e. secondary electron emission, electron and heavy particle adsorption/reflection, and target sputtering are accounted for (section 2.4). The surface coefficients, $SEEC$ and RC, are chosen as 0.08 and 0.1, respectively. In this chapter and the following chapters (5 and 6), a Ti target was used in both the experiments and the calculations, whereas in the previous chapter (3), the experiments were carried out with an Al target (note that the sputtered atoms themselves were not taken into account in the model of chapter 3). This explains the different $SEEC$ and RC values from the previous chapter.

4.4 Included collisions

To investigate the influence of the magnetic field strength on the sputter deposition process, the sputtered Ti atoms are taken into account, as well as the Ti^+ ions. After thermalization, the Ti atoms are described in the model with balance equations (see section 2.5.1 above). Also metastable Ar_m^* atoms are included, since they are important for Penning ionization, as well as fast Ar_f atoms (which originate from elastic collisions, including symmetric charge transfer collisions, with Ar^+ ions [58], i.e. reactions (8) and (9) from table 4.1 below), because they are important for sputtering.

The list of the considered collisions and references to their corresponding cross sections or rate constants is given in table 4.1. Note that only electrons and Ar^+ ions are assumed to be present from the beginning. The rest of the considered species is created by plasma reactions (from table 4.1).

In addition to the cross section data shown figure 3.1 above, cross sections for the newly added Ti atoms, Ti^+ ions, metastable Ar^*_m atoms, and fast Ar_f, are plotted against the incident species' energy in figure 4.1.

Table 4.1: List of the collisions considered in the model. The references where the cross sections ($\sigma(E)$) or rate constants (k, in $m^3\ s^{-1}$) were adopted from are presented in the last column.

e^- collisions				
(1)	$e^- + Ar \rightarrow e^- + Ar$	elastic scattering	$\sigma(E)$	[79]
(2)	$e^- + Ar \rightarrow 2e^- + Ar^+$	electron-impact ionization	$\sigma(E)$	[80]
(3)	$e^- + Ar \rightarrow e^- + Ar^*_m$	electron-impact excitation	$\sigma(E)$	[81]
(4)	$e^- + Ar \rightarrow e^- + Ar^*$	electron-impact excitation	$\sigma(E)$	[82]
(5)	$e^- + Ar^*_m \rightarrow 2e^- + Ar^+$	electron-impact ionization	$\sigma(E)$	[92]
(6)	$e^- + Ar^*_m \rightarrow e^- + Ar^*$	electron-impact excitation	$\sigma(E)$	[93]
(7)	$e^- + Ti \rightarrow 2e^- + Cu^+$	electron-impact ionization	$\sigma(E)$	[94]
Ar^+ collisions				
(8)	$Ar^+ + Ar \rightarrow Ar^+ + Ar_{(f)}$	elastic scattering	$\sigma(E)$	[58]
(9)	$Ar^+ + Ar \rightarrow Ar_{(f)} + Ar^+$	charge transfer	$\sigma(E)$	[58]
(10)	$Ar^+ + Ar \rightarrow 2Ar^+ + e^-$	ion-impact ionization	$\sigma(E)$	[83]
(11)	$Ar^+ + Ar \rightarrow Ar^+ + Ar^*_m$	ion-impact excitation	$\sigma(E)$	[83]
(12)	$Ar^+ + Ti \rightarrow Ar + Ti^+$	charge transfer	$k = 6.61 \times 10^{-17}$	[95]
Ar^*_m collisions				
(13)	$Ar^*_m + Ar^*_m \rightarrow Ar + Ar^+ + e^-$	metastable-metastable collision	$k = 6.4 \times 10^{-16}$	[96,97]
(14)	$Ar^*_m + Ti \rightarrow Ar + Ti^+ + e^-$	Penning ionization	$\sigma = 4.93 \times 10^{-19}$	[98]
(15)	$Ar^*_m + Ar \rightarrow Ar + Ar$	two-body collision	$k = 2.3 \times 10^{-21}$	[99]
Ar_f collisions				
(16)	$Ar_f + Ar \rightarrow Ar_{(f)} + Ar_{(f)}$	elastic scattering	$\sigma(E)$	[100]
(17)	$Ar_f + Ar \rightarrow Ar + Ar^+$	atom-impact ionization	$\sigma(E)$	[83]
(18)	$Ar_f + Ar \rightarrow Ar_f + Ar^*_m$	atom-impact excitation	$\sigma(E)$	[101]
$Ti^{(+)}$ collisions				
(19)	$Ti^{(+)} + Ar \rightarrow Ti^{(+)} + Ar$	elastic scattering	$\sigma = 6 \times 10^{-20}$	[102]

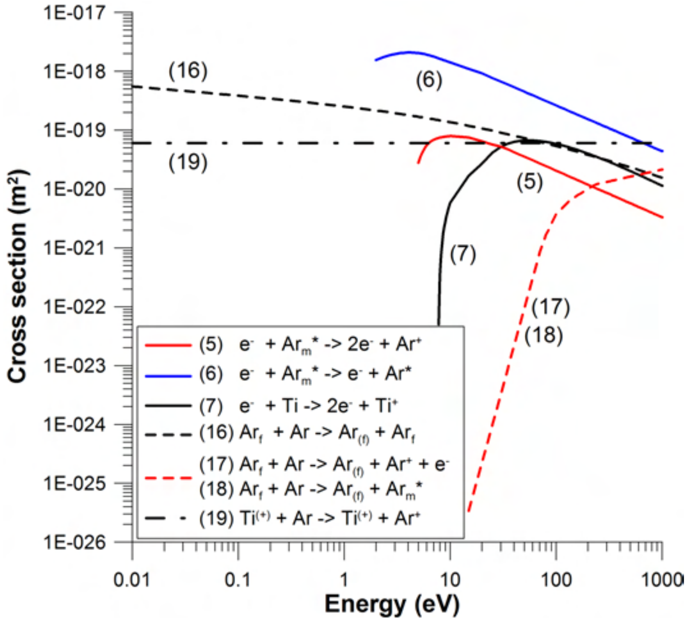

Figure 4.1: Cross section data of the additional collisions (apart from the collisions which cross section data are illustrated in figure 3.1), included in the model. The references where this data is adopted from are given in table 4.1.

4.5 Results and discussion

4.5.1 Plasma potential

The normalized plasma potential distribution on the line above the race track (i.e. $r = 13.5$ mm) for the different magnetic field strengths is presented in figure 4.2. For the weaker applied magnetic fields, i.e. in this case from 520 G to 730 G, the sheath thickness decreases when the magnetic field strength is increased. Similar results of a decreasing sheath width were found experimentally by Kuwahara et al. [87] (for an increase of the magnetic field strength of 10 G to 190 G), by Bowden et al. [88] (when increasing the magnetic field strength from 200 G to 450 G), and by Gu et al. [25] (when increasing the magnetic field from 140 G to 570 G). Computational studies also confirm this contraction of the sheath: Kondo et al. [43] calculated a decrease in sheath thickness with increasing the magnetic field from 330 G to 660 G, Nanbu et al. [89] when increasing the magnetic field from 250 G to 1000 G, and Bradley et al. [90] when increasing the magnetic field strength from 30 G to 110 G. Pandey et al. [103] studied the effect of separate electron and ion magnetization and found a decrease in sheath width with increasing magnetization, albeit, for larger magnetic field variations.

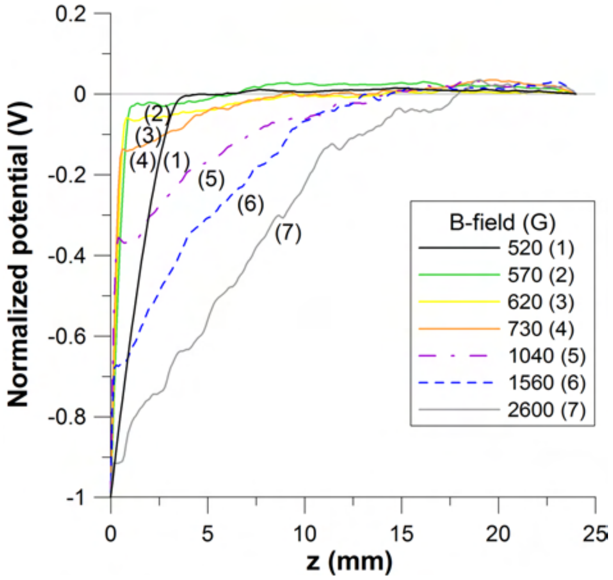

Figure 4.2: Normalized calculated potential distribution at a line above the race track (i.e. $r = 13.5$ mm), for different values of the magnetic field strength, as indicated in the legend.

Note that for these weak magnetic fields, the profile of the plasma potential (figure 4.2) is similar to the case of a non-magnetized plasma. However, when a magnetic field is applied of at least 730 G, figure 4.2 shows a sudden broadening of the potential profile. This broadening becomes more distinct with rising magnetic field strength. Wendt and Lieberman [28] have found evidence for these so-called "thick sheaths", and measurements of Yeom [84] also confirm this. Lister [91], using a 1D fluid model, finds a broadening of the sheath when increasing the magnetic field as well, in the case of a sufficiently strong magnetic field (up to 1000 G).

4.5.2 Ion and electron densities

Since the sheath structure is determined by the ion distribution, the ion densities on the same line above the race track are presented in figure 4.3. Only the Ar^+ ion density is presented, since this is the dominant ion, determining the potential distribution.

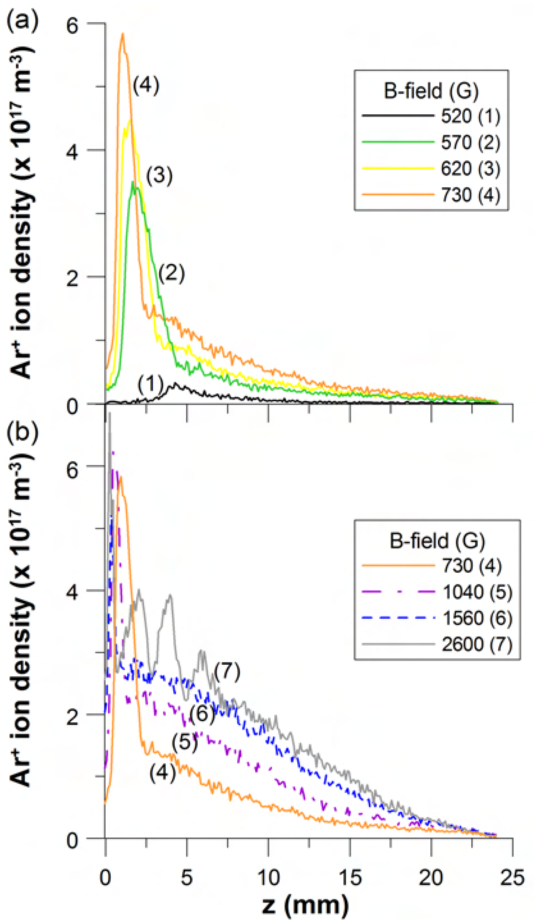

Figure 4.3: Calculated Ar^+ densities at a line above the race track (i.e. $r = 13.5$ mm), for low (a) and high (b) magnetic field strengths.

At low applied magnetic field strengths (figure 4.3a), a higher density peak is observed with increasing magnetic field, which is shifted towards the cathode, explaining the thinner sheath. The shift towards the cathode is justified by the well known fact of decreasing Debye length with rising ion density.

At higher magnetic field strengths, the ion density profiles, presented in figure 4.3b, show that the peak of the ion densities is approximately constant when increasing the magnetic field (although it shifts slightly towards the cathode), but in the tail of the profile, the ion densities increase. This is explained as follows. The electrons gyrate around the magnetic field lines with their Larmor radius. If the magnetic field is weak, the electrons are easily lost to the cathode wall, causing the creation of a positive ion sheath (i), see figure 4.4(a) (at $z = 0 - 2.5$ mm). When the magnetic field strength is increased, the Larmor radius becomes smaller, until the electrons are virtually trapped in the pre-sheath by the strong magnetic field. Therefore, their movement to the cathode wall is inhibited, leading to a less pronounced potential build up on the cathode wall and a less pronounced positive space charge in front of the cathode. This so-called magnetized pre-sheath or Chodura layer was also reported in [104–106]. In our case, it is clear from figure 4.4(b) that the electron density in front of the cathode even rises above zero, meaning that the ion sheath disappears. The Debye sheath (d) narrows and shifts towards the cathode, and the pre-sheath (p) widens. As a result, it is observed from our calculations that at a certain magnetic field strength (i.e. around 620-730 G, see figure 4.4(b)) the electron density starts to spread out towards the tail of the pre-sheath. Correspondingly, also the ion density expands (i.e. the pre-sheath widens), as presented in figure 4.3.

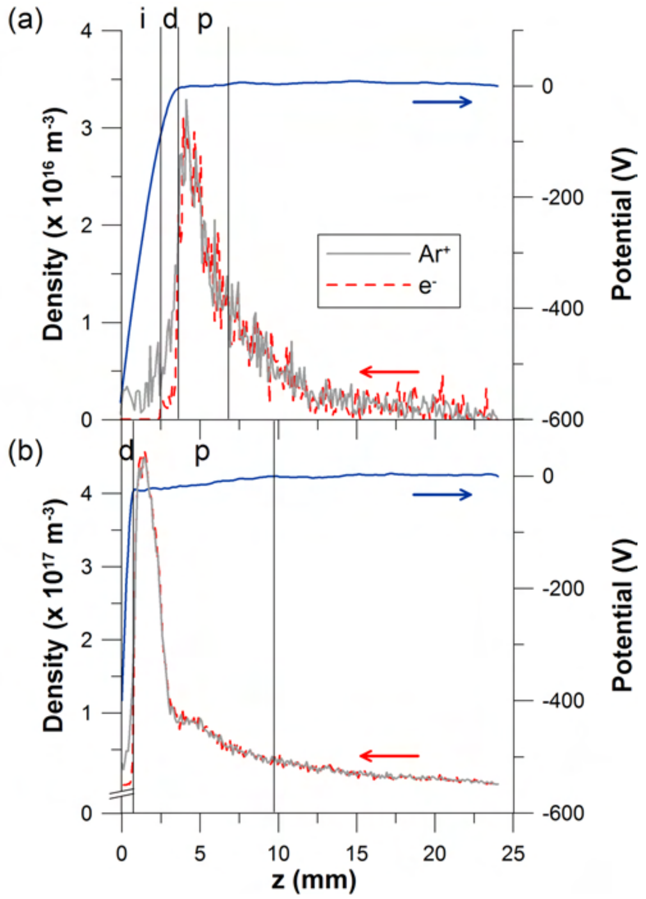

Figure 4.4: Calculated electron (dashed red line) and Ar$^+$ (solid grey line) densities, and potential distribution (blue line) at a line above the race track (i.e. $r = 13.5$ mm), for a magnetic field strength of 520 G (a) and 620 G (b). Also, the different sheath areas, i.e. the ion sheath (i), the Debye sheath (d), and the pre-sheath (p) are indicated. For better visualizing, the y-axis in (b) is stretched out between 0 and 10^{15}, since the electron density at $z = 0$ mm is 6.5×10^{15} m^{-3} s^{-1}.

4.5.3 Sputter and deposition fluxes

The difference in sheath behavior in a weak or a strong magnetic field will influence the sputter process. In a weak magnetic field, the ion density peak increases with the magnetic field. As a consequence, more Ti particles will be sputtered from the cathode surface, presented in figure 4.5. On the other hand, when increasing further the magnetic field strength above 730 G, the ion density tail increases but the peak stays constant. Therefore, the amount of sputtering remains approximately constant, as is clear from figure 4.5. Since the amount of sputtering determines the erosion of the target, at weak magnetic fields, the erosion profile will be less deep than at higher magnetic fields.

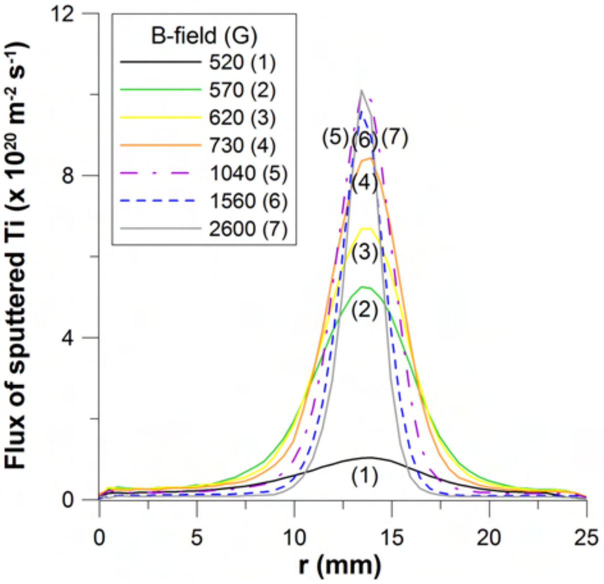

Figure 4.5: Calculated flux of sputtered Ti particles from the cathode target as a function of radial position, for different values of the magnetic field strength. Note that the y-axis (r=0) corresponds to the symmetry axis of the cilindrically symmetrical reactor.

On the other hand, also the width of the erosion profile is influenced by the magnetic field. At low magnetic field strengths, the sputter flux is more spread out, whereas, for high magnetic field strengths, the flux profile is very narrow. This is a consequence of the decreasing Larmor radius at increasing the magnetic field strength, and was also found in [28]. Consequently, at weak magnetic fields, although the sputter flux is low, the target is consumed more efficiently. At strong magnetic fields, there is a high sputter flux, but the erosion profile is very deep and narrow. A similar behavior was also found for the calculated fluxes of the depositing atoms at the substrate (not presented here).

4.5.4 Current, voltage and power

The effect of the magnetic field on the sputter and deposition rates can also be explained by the electrical current, potential and power, which are calculated self-consistently in the model, and are presented in figure 4.6.

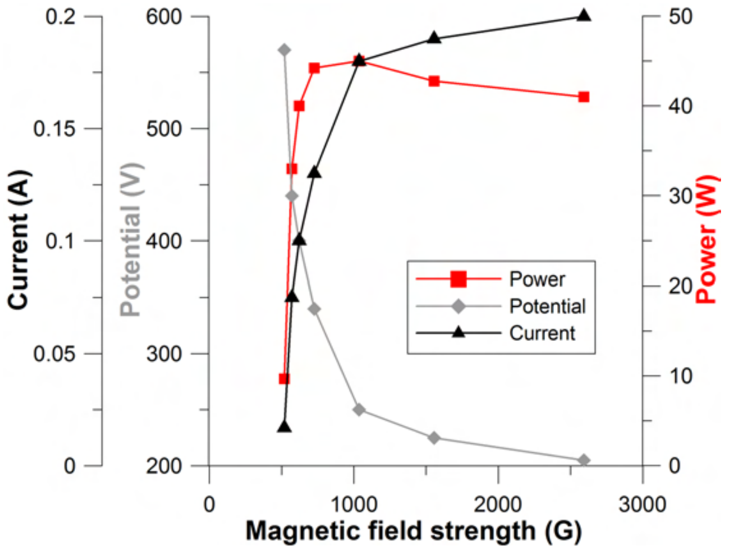

Figure 4.6: Calculated cathode current, potential (in absolute value) and power, for different values of the magnetic field strength.

An increase and a drop of the current I and the potential V, respectively, is seen when the magnetic field strength is increased. These I and V curves show the steepest slopes at low magnetic field strengths. Consequently, the power rises strongly for the low magnetic field strengths, but remains approximately constant at the high magnetic field strengths. This demonstrates that the power is more or less linearly connected to the sputtered Ti flux. This is logical because the sputter flux is determined by (i) the flux of the bombarding ions which is proportional to the current, and (ii) the sputter yield which depends on the energy of the bombarding species and hence on the voltage [63].

4.6 Conclusion

For the sputtering process, the cathode sheath is the most important area in magnetron discharges, since ions are accelerated here, gaining energy to sputter the cathode target. However, the sheath is also the most complicated and uncomprehended area in discharges, especially in magnetron discharges. Indeed, when an external magnetic field is present, the sheath behavior is dependent on the strength of the magnetic field. This was demonstrated by the calculation of plasma potentials and ion density profiles for different magnetic field strengths: at weak magnetic fields, the sheath width decreases with increasing magnetic field strength, whereas the opposite trend was noticed at strong magnetic fields. Even very thick sheaths were created, which was verified by experimental and other computational works. This was explained by the electron densities in the different sheath regions (pre-sheath, Debye sheath and ion sheath): at strong magnetic fields, the electrons not only reside in the bulk, but are also confined to the sheath. In our case, electrons are present in the pre-sheath, the Debye sheath, and even very close to the cathode, meaning that the ion sheath disappears. The Debye sheath narrows, and the pre-sheath widens at increasing magnetic field strength. This trapping limits the electrons' mobility, preventing a pronounced plasma potential build up, and hence the positive space charge is more spread out.

Furthermore, the sheath behavior influences the sputter deposition process. At weak magnetic fields, the sputtered Ti flux increases with rising magnetic field strength. At strong magnetic fields, the sputtered flux remains approximately constant. This trend is explained by the ion densities. Moreover, the profile becomes very narrow at high magnetic field strengths, and the target is therefore less efficiently consumed. In other words, one is able to control the depth and width of the erosion profile with the magnetic field strength, and a considered choice is essential for the optimal balance between a high sputter flux and an efficiently consumed target.

Chapter 5

Ar/N_2 mixture: reactive sputter deposition of TiN_x

5.1 Introduction

When a reactive gas like nitrogen is added to the argon discharge, N atoms originating from this reactive gas as well as the N_2 gas molecules themselves can react with the sputtered metal atoms on the substrate to form a metal nitride layer [8, 12–18, 107] in a proces called "reactive sputter deposition" (for a schematic presentation, see figure 1.2 above). Certain metal nitride layers have interesting tribological properties [14, 15, 17, 18, 107, 108], such as anti-reflective, anti-static, hard, and corrosion and wear resistant. Some also have interesting electrical properties [14, 16].

In the literature, reactive magnetron sputter deposition for an Ar/N_2 gas mixture was studied by means of simple analytical models, such as [22,30,31]. To our knowledge, no PIC/MCC model has been developed for an Ar/N_2 mixture before.

Therefore, to study the reactive magnetron sputter deposition process of TiN_x layers, a 2d3v PIC/MCC model is applied, including plasma-surface interactions. More specifically, the influence of a poisoned target on the

SEEC and the sputter yield is described, as well as the deposition process. For the latter, an analytical surface model, based on [30, 31, 68], is coupled to the PIC/MCC model to calculate the effective sticking of Ti, N and N_2 onto the substrate (see also section 2.4 above).

With this PIC/MCC model, cathode currents and voltages are calculated self-consistently and compared with experiments. Also, ion fractions at different N_2/Ar gas ratios are calculated and validated with mass spectrometric measurements. The influence of N_2/Ar gas ratio on the particle densities and fluxes is investigated. Moreover, the analytical surface model accounts for the effective sticking of Ti, N and N_2 species onto the substrate. The latter enables to predict the stoichiometry of the deposited TiN_x film.

5.2 Description of the magnetron discharge and simulated conditions

The simulated magnetron discharge in this chapter is the same as in the previous chapters, see section 3.2. The scheme of the simulated magnetron discharge was presented in figure 2.1.

The magnetron discharge operates in 1 Pa Ar gas, at 300 K. The external voltages and resistances, V_{ext} and R_{ext}, from which the cathode currents and voltages, I and V_0, are calculated self-consistently, are mentioned in the results section below. To study the effect of the N_2/Ar gas proportion, the Ar partial pressure is kept constant at 1 Pa for all calculations, whereas the N_2 partial pressure is increased as 0.03, 0.06, 0.13, 0.19, and 0.26 Pa. Under these conditions, the target is always fully poisoned. The conditions were chosen in order to avoid (i) the simulation of the hysteresis, and (ii) having to deal with a partially reacted TiN_x target.

5.3 Overview of the model

The model developed for the Ar/N_2 magnetron discharge is based on the model used in the previous chapters, and is described in detail in chapter 2. However, certain species and collision events are added, which are listed below (section 5.5). Moreover, the influence of a poisoned target on the plasma-surface interactions, i.e. on secondary electron emission and on sputtering is included. Finally, the coupling of the analytical surface model to the PIC/MCC model accounts for the deposition process (see also section 2.4 above, and section 5.4 below).

5.4 Plasma-surface interactions

In order to find the *RC* and $SEEC$ values of the Ti target, a discharge in pure Ar is evaluated. Since both the *RC* and the $SEEC$ directly influence the cathode current and voltage [109], they are slightly adapted in the model, so that the calculated currents and voltages can be compared with experimental values. Note, however, that these coefficients are kept the same for the different $I - V$ combinations investigated for sputtering of Ti in pure Ar. Afterwards, N_2 gas is added, under pressures for which the target is completely in poisoned mode. As a consequence of target poisoning, the $SEEC$ value alters, and in the case of a TiN_x target, the $SEEC$ decreases [61]. Therefore, the $SEEC$ value is adjusted, in accordance to the range reported in [61] (see values below, in section 5.6.1), and the calculated currents and voltages are again compared with experiments.

Both Ti and N atoms can be sputtered from the fully poisoned TiN_x target, but their sputter yield is lower than for the sputtering of Ti atoms from a metallic Ti target. According to the values reported in [22], the sputter yield of Ti from a fully poisoned target is lowered with a factor of 6.4 compared to the sputter yield of Ti from a metallic target. On the other hand, the sputter yield of N from a fully poisoned target is 4 times higher, compared to the sputter yield of Ti from a fully poisoned target. These assumed changes in sputter yields for the poisoned target are applied to all of the bombarding species (i.e. Ar$^+$, Ar$_f$, N$_2^+$, N$^+$, Ti$^+$; see later, section 5.6.4 and tables 5.3 and 5.4).

To describe the deposition of the TiN$_x$ film, an analytical surface model is coupled to the PIC/MCC model, which calculates effective sticking coefficients for the bombarding N, N$_2$ and Ti species (SC_{eff}) based on the compound fraction on the substrate (θ_{cs}). In section 2.4.4, a general description is given for a A$_w$B$_x$ deposited film, originating from metal A and gas B$_y$. Details for the deposition of a TiN$_x$ thin film by N$_2$ gas molecules, N atoms and Ti atoms are given here. From equation 2.81, which is based on [30,31,68], a compound fraction balance equation, for the deposition of a TiN$_x$ film with a desired stoichiometry x=1, is constructed:

$$2SC_{N_2}F_{N_2}(1-\theta_{cs}) + SC_N F_N(1-\theta_{cs}) = SC_{Ti}F_{Ti}\theta_{cs} \tag{5.1}$$

With this equation, at every PIC/MCC time step, the fraction of TiN compound on every radial position on the substrate (s), θ_{cs}, is derived from the fluxes (F) of the incoming N$_2$, N and Ti species (calculated with the PIC/MCC model), with corresponding constant SC. These SC values are chosen as 0.3 for N$_2$ [22], 1 for N [22] and 0.5 for Ti [67]:

$$\theta_{cs} = \frac{2SC_{N_2}F_{N_2} + SC_N F_N}{2SC_{N_2}F_{N_2} + SC_N F_N + SC_{Ti}F_{Ti}} \tag{5.2}$$

Subsequently, the SC values of N and N$_2$ are adapted at that time step by the compound fraction, θ_{cs}, so that we obtain the so-called effective sticking coefficients, SC_{eff}, for this time step, on every position r on the substrate:

$$\begin{aligned} SC_{N_2,eff} &= SC_{N_2}(1-\theta_{cs}) \\ SC_{N,eff} &= SC_N(1-\theta_{cs}) \end{aligned} \tag{5.3}$$

Indeed, the sticking of N and N$_2$ on TiN$_x$ compound will be lower than on a pure metallic surface. Since the sticking of Ti is independent on the compound fraction (i.e. Ti will stick in a similar way on a metallic Ti surface and on a TiN_x surface), a constant SC_{Ti} can be used, i.e. $SC_{Ti,eff} = SC_{Ti}$. Note that the actual stoichiometry of the deposited TiN_x film, x, is found by multiplying the desired stoichiometry, x=1, by the compound fraction, θ_{cs}.

5.5 Included collisions

Apart from the already present electrons, Ar^+ ions, metastable Ar_m^* atoms, fast Ar_f atoms Ti^+ ions, and Ti atoms, the new species taken into account in the model are N^+ ions, N_2^+ ions, and N atoms. The list of the considered collisions in the Ar/N_2 discharge, and their rate constants and references to their cross sections is given in table 5.1. Besides elastic collisions with Ar atoms, and electron impact ionization and excitation of Ar (ground state and metastable atoms), also electron impact ionization, excitation (to four different excited levels), dissociative ionization and dissociation of the N_2 gas molecules are included. Ionization of N is not considered, because N has a lower density, and hence its ionization is less important. Also, the density of N^+ is low, so recombination of N^+ is also not included. Elastic collisions of electrons with N_2 are also omitted, due to the lower density of N_2, so the momentum change of the electrons by elastic collisions with N_2 is small compared with Ar. As far as the heavy particle collisions are concerned, elastic scattering of Ti^+ with N_2 and N is included, because, in constrast to electrons, a considerable amount of energy is transferred. Charge transfer of Ar^+ with N_2 is included, due to its very high rate constant. The model also contains elastic and charge transfer $N(_2)^+$ collisions with Ar, N_2 and N.

Note that not only electrons and Ar^+ ions are present from the beginning, but also N^+ ions and N_2^+ ions. Fast N atoms, created out of the initial species (by plasma reactions or by sputtering) are considered. After thermalization, the Ti and N atoms are described with balance equations, as described in section 2.5.1 above.

Table 5.1: List of the collisions considered in the model. The references where the cross sections ($\sigma(E)$) or rate constants (k, in m^3 s^{-1}) were adopted from are presented in the last column. "(a)" refers to assumed rate constants based on similar reactions, due to lack of data in the literature. "LH" refers to the Langevin-Hasse treatment for the cross section (see text above).

e^- collisions				
(1)	$e^- + Ar \rightarrow e^- + Ar$	elastic scattering	$\sigma(E)$	[79]
(2)	$e^- + Ar \rightarrow 2e^- + Ar^+$	electron-impact ionization	$\sigma(E)$	[80]
(3)	$e^- + Ar \rightarrow e^- + Ar_m^*$	electron-impact excitation	$\sigma(E)$	[81]
(4)	$e^- + Ar \rightarrow e^- + Ar^*$	electron-impact excitation	$\sigma(E)$	[82]
(5)	$e^- + Ar_m^* \rightarrow 2e^- + Ar^+$	electron-impact ionization	$\sigma(E)$	[92]
(6)	$e^- + Ar_m^* \rightarrow e^- + Ar^*$	electron-impact excitation	$\sigma(E)$	[93]
(7)	$e^- + Ti \rightarrow 2e^- + Cu^+$	electron-impact ionization	$\sigma(E)$	[94]
(8)	$e^- + N_2 \rightarrow 2e^- + N_2^+$	electron-impact ionization	$\sigma(E)$	[110]
(9)	$e^- + N_2 \rightarrow e^- + N_2^*$	electron-impact excitation to $A^3\sigma_u^+$	$\sigma(E)$	[110]
(10)	$e^- + N_2 \rightarrow e^- + N_2^*$	electron-impact excitation to $B^3\Pi$	$\sigma(E)$	[110]
(11)	$e^- + N_2 \rightarrow e^- + N_2^*$	electron-impact excitation to $C^3\Pi$	$\sigma(E)$	[110]
(12)	$e^- + N_2 \rightarrow e^- + N_2^*$	electron-impact excitation to $a^1\Pi_g$	$\sigma(E)$	[110]
(13)	$e^- + N_2 \rightarrow 2e^- + N^+ + N$	dissociative ionization	$\sigma(E)$	[111]
(14)	$e^- + N_2 \rightarrow e^- + N + N$	dissociation	$\sigma(E)$	[110]
(15)	$e^- + N_2^+ \rightarrow N + N$	dissociative recombination	$k = 4.8 \times 10^{-13}\sqrt{300/T_e}$	[112]
Ar^+ collisions				
(16)	$Ar^+ + Ar \rightarrow Ar^+ + Ar$	elastic scattering	$\sigma(E)$	[58]
(17)	$Ar^+ + Ar \rightarrow Ar + Ar^+$	charge transfer	$\sigma(E)$	[58]
(18)	$Ar^+ + Ar \rightarrow 2Ar^+ + e^-$	ion-impact ionization	$\sigma(E)$	[83]
(19)	$Ar^+ + Ar \rightarrow Ar^+ + Ar_m^*$	ion-impact excitation	$\sigma(E)$	[83]
(20)	$Ar^+ + Ti \rightarrow Ar + Ti^+$	charge transfer	$k = 6.61 \times 10^{-17}$	[95]
(21)	$Ar^+ + N_2 \rightarrow Ar + N_2^+$	charge transfer	$k = 4.45 \times 10^{-16}$	[113]
Ar_m^* collisions				
(22)	$Ar_m^* + Ar_m^* \rightarrow Ar + Ar^+ + e^-$	metastable-metastable collision	$k = 6.4 \times 10^{-16}$	[96, 97]
(23)	$Ar_m^* + Ti \rightarrow Ar + Ti^+ + e^-$	Penning ionization	$\sigma = 4.93 \times 10^{-19}$	[98]
(24)	$Ar_m^* + Ar \rightarrow Ar + Ar$	two-body collision	$k = 2.3 \times 10^{-21}$	[99]
Ar_f collisions				
(25)	$Ar_f + Ar \rightarrow Ar_{(f)} + Ar_{(f)}$	elastic scattering	$\sigma(E)$	[100]
(26)	$Ar_f + Ar \rightarrow Ar + Ar^+$	atom-impact ionization	$\sigma(E)$	[83]
(27)	$Ar_f + Ar \rightarrow Ar_f + Ar_m^*$	atom-impact excitation	$\sigma(E)$	[101]
Ti^+ collisions				
(28)	$Ti^+ + Ar \rightarrow Ti^+ + Ar$	elastic scattering	$\sigma = 6 \times 10^{-20}$	[102]
(29)	$Ti^+ + N_2 \rightarrow Ti^+ + N_2$	elastic scattering	$\sigma(E)$	LH
(30)	$Ti^+ + N \rightarrow Ti^+ + N$	elastic scattering	$\sigma(E)$	LH
Ti collisions				
(31)	$Ti_f + Ar \rightarrow Ti + Ar_f$	elastic scattering	$\sigma = 6 \times 10^{-20}$	[102]
(32)	$Ti + N \rightarrow TiN$	attachment	only at the walls (SC)	
N^+ collisions				
(33)	$N^+ + Ar \rightarrow N^+ + Ar_f$	elastic scattering	$\sigma(E)$	LH
(34)	$N^+ + Ar \rightarrow N + Ar^+$	charge transfer	$k = 4 \times 10^{-17}$	(a)
(35)	$N^+ + N_2 \rightarrow N^+ + N_2$	elastic scattering	$\sigma(E)$	LH
(36)	$N^+ + N_2 \rightarrow N + N_2^+$	charge transfer	$k = 4 \times 10^{-17}$	(a)
(37)	$N^+ + N \rightarrow N^+ + N_f$	elastic scattering	$\sigma(E)$	LH
(38)	$N^+ + N \rightarrow N_f + N^+$	charge transfer	$k = 4 \times 10^{-17}$	(a)
N_2^+ collisions				
(39)	$N_2^+ + Ar \rightarrow N_2^+ + Ar$	elastic scattering	$\sigma(E)$	LH
(40)	$N_2^+ + Ar \rightarrow N_2 + Ar^+$	charge transfer	$k = 1 \times 10^{-17}$	(a)
(41)	$N_2^+ + N_2 \rightarrow N_2^+ + N_2$	elastic scattering	$\sigma(E)$	LH
(42)	$N_2^+ + N_2 \rightarrow N_2 + N_2^+$	charge transfer	$k = 1 \times 10^{-17}$	(a)
(43)	$N_2^+ + N \rightarrow N_2^+ + N$	elastic scattering	$\sigma(E)$	LH
(44)	$N_2^+ + N \rightarrow N_2 + N^+$	charge transfer	$k = 1 \times 10^{-17}$	(a)

Certain cross sections can not be found in the literature. Therefore, some cross sections of ion-neutral collisions, σ, are described with the Langevin-Hasse model [114, 115], assigned "LH" in table 5.1:

$$\sigma = \left(\frac{\pi\alpha_p e^2}{\epsilon_0\mu}\right)^{1/2} \beta_\infty^2 g^{-1}, \tag{5.4}$$

where α_p is the polarizability, e is the electron charge, ϵ_0 is the permittivity of vacuum, μ is the reduced mass, $g = |v_i - v_n|$ is the relative precollision velocity, with v_i and v_n the ion and neutral velocities, respectively, and β_∞ is the value of the dimensionless impact parameter β, for which the deflection angle is negligibly small [57]. This value is set to 3 for Ar, N_2 and N [115]. The polarizability for Ar is 11.08 a_0^3 [86], 18.24 a_0^3 for N_2 [116], and 7.5 a_0^3 for N [86], where a_0 is the Bohr radius.

In addition to the cross section data from figure 3.1 and 4.1, the newly added electron-impact cross sections are plotted against electron energy in figure 5.1.

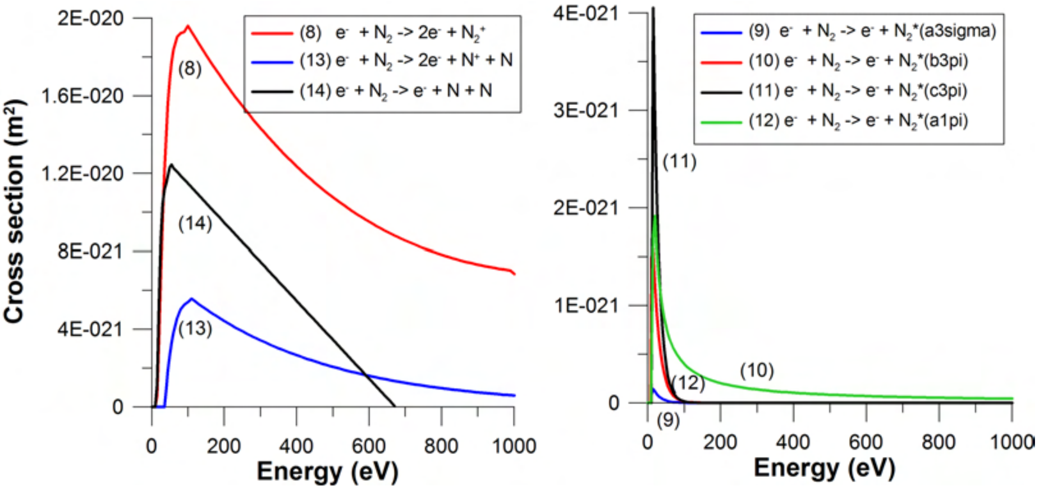

Figure 5.1: Cross section data of the additional electron-impact collisions (apart from the collisions which were illustrated in figures 3.1 and 4.1), included in the model. The references where this data is adopted from are given in table 5.1.

5.6 Results and discussion

5.6.1 Current-voltage characteristics

In our calculations, a pure Ar discharge was generated with an external voltage of -600 V. The discharge current and potential were varied by modifying the external resistance, as 1500 Ω, 1400 Ω, and 1300 Ω. A *RC* of 0.1 and a *SEEC* of 0.075 yielded calculated $I - V$ values in good agreement with the experimental data in pure Ar, as illustrated in table 5.2.

Table 5.2: Measured and calculated values of the cathode potentials (V_0) and currents (I) for a pure argon gas with a pressure of 1.0 Pa, an external voltage (V_{ext}) of -600 V, and external resistances (R_{ext}) as mentioned in the table.

Measured		Calculated		Input
V_0 (V)	I (A)	V_0 (V)	I (A)	R_{ext} (Ω)
-260	0.20	-255	0.23	1500
-264	0.23	-257	0.25	1400
-266	0.26	-257	0.26	1300

In the Ar/N_2 mixture, the cathode current was kept constant at 0.2 A, by keeping the external resistance at 1500 Ω. The *SEEC* alters as a consequence of poisoning, and in the case of a TiN_x target, the *SEEC* decreases [61]. Note that the *SEEC* values applied in the model comprise the *SEEC* values of all different incident species, to avoid complicating the model with different uncertain parameters. From figure 5.2, it is clear that the overall *SEEC* is lowered in the model with increasing the N_2 pressure. However, in reality, the *SEEC* values of individual species will probably decrease first, but then remain constant once the poisoning is complete. Nevertheless, the proportion $N(_2)^+/Ar^+$ will increase with N_2 pressure, and because the *SEEC* of $N(_2)^+$ is much lower than the *SEEC* of Ar^+ [117], the overall *SEEC* will indeed decrease with increasing N_2 pressure. The used *SEEC* values, and the calculated currents and voltages as a function of N_2 partial pressure are illustrated in figure 5.2, as well as the experimental values.

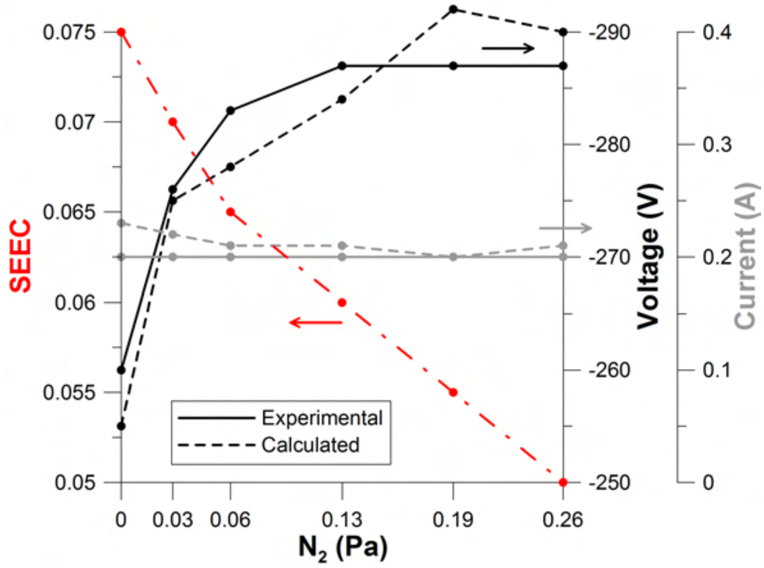

Figure 5.2: Measured and calculated values of the cathode potentials and currents as a function of N_2 partial pressure, at an Ar partial pressure of 1.0 Pa, an external voltage (V_{ext}) of -600 V, and an external resistance (R_{ext}) of 1500 Ω. The $SEEC$ values used in the model for different N_2 partial pressures are also indicated.

5.6.2 Electron, ion and atom densities

The externally applied magnetic field traps the electrons in an area close to the cathode. Most electrons are trapped in the region where the radial magnetic field is at maximum, causing a peak in the electron density. This is clear from figure 5.3, presenting the electron density in the simulation area (r, z), for the case of 0.26 Pa N_2. Similar profiles for the other N_2 partial pressures were obtained, but they are not shown. Indeed, since the $SEEC$ only varies within a limited range due to gas composition (see section 5.6.1), it will not have a large effect on the electron density.

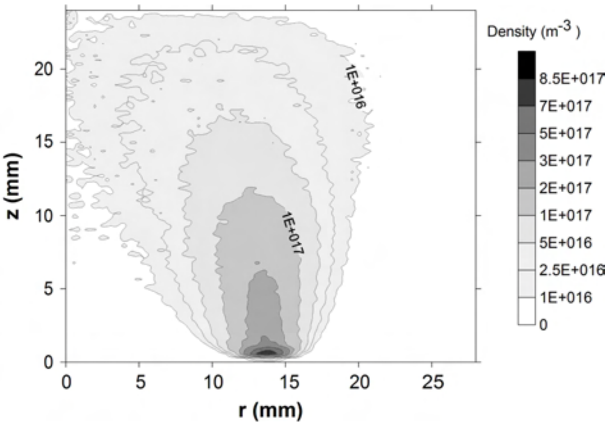

Figure 5.3: Calculated electron density profile (in m^{-3}) at an Ar partial pressure of 1.0 Pa and a N_2 partial pressure of 0.26 Pa. Note that the y-axis (r=0) corresponds to the symmetry axis of the cilindrically symmetrical reactor.

The electron density was also measured with a Langmuir probe. Due to limitations in size of the probe, measurements could only be carried out from at least 10 mm above the target. The calculated and measured electron densities for an Ar partial pressure of 1.0 Pa and a N_2 partial pressure of 0.26 Pa are presented in figure 5.4. A relatively good agreement is found between the experimental and the calculated electron density: the density profile exhibits the same curved form towards the center of the reactor, and the absolute values are in the same range. The only discrepancy is found at the borders, which is caused by the fact that in the calculations, “walls” are present, causing the density to drop there towards zero. On the other hand, in the experiments, these walls were much further away.

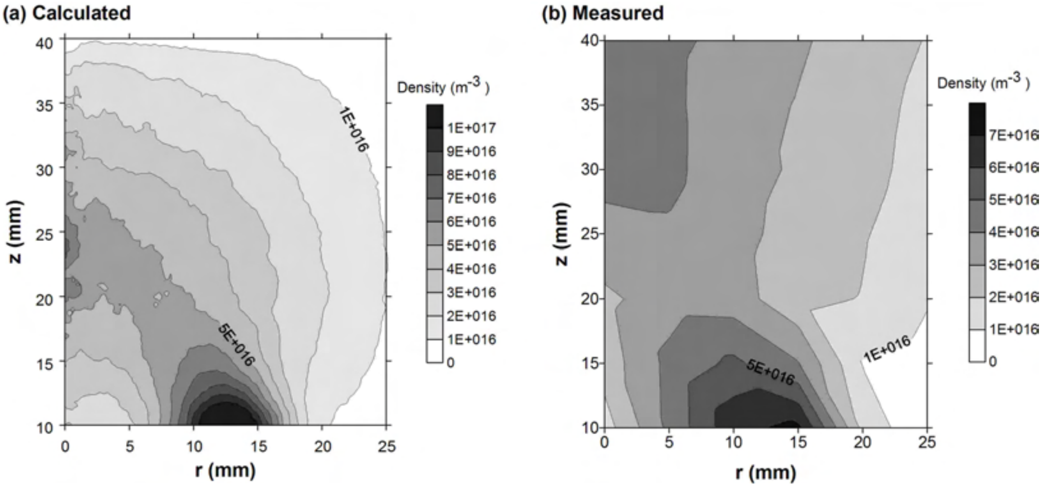

Figure 5.4: Calculated (a) and measured (b) electron density profiles (in m^{-3}) from a distance of 10 mm to 40 mm above the target surface, at an Ar partial pressure of 1.0 Pa and a N_2 partial pressure of 0.26 Pa. Note that the y-axis (r=0) corresponds to the symmetry axis of the cilindrically symmetrical reactor.

The localized electrons ionize neutrals, leading to similar density profiles for the Ar^+ ions, N^+ ions, N_2^+ ions, and Ti^+ ions, as shown in figure 5.5, for a N_2 partial pressure of 0.26 Pa. It is clear from this figure that the Ar^+ ions are the dominant positive ions, with a maximum density of $7 \times 10^{17}\ m^{-3}$, which is only slightly lower than the maximum electron density (see figure 5.3). The N_2^+ ions reach a maximum density of about $1.2 \times 10^{17} m^{-3}$, which is a factor of almost 6 lower than the Ar^+ density, despite the fact that the N_2 partial pressure is only a factor of 4 lower than the Ar partial pressure. This is attributed to the fact that the N_2^+ ions are lost more efficiently (by dissociative recombination with electrons) than the Ar^+ ions. The N^+ ion density is still two orders of magnitude lower (with a maximum density of about $3 \times 10^{15} m^{-3}$), which can be explained by the rather low dissociation degree of N_2 (i.e. the N atom density is also much lower than the N_2 density, as will be shown below). The Ti^+ ions have an even lower density, with a maximum of only $1 \times 10^{15} m^{-3}$, because these species do not originate from the background gases, but only from ionization of the sputtered atoms.

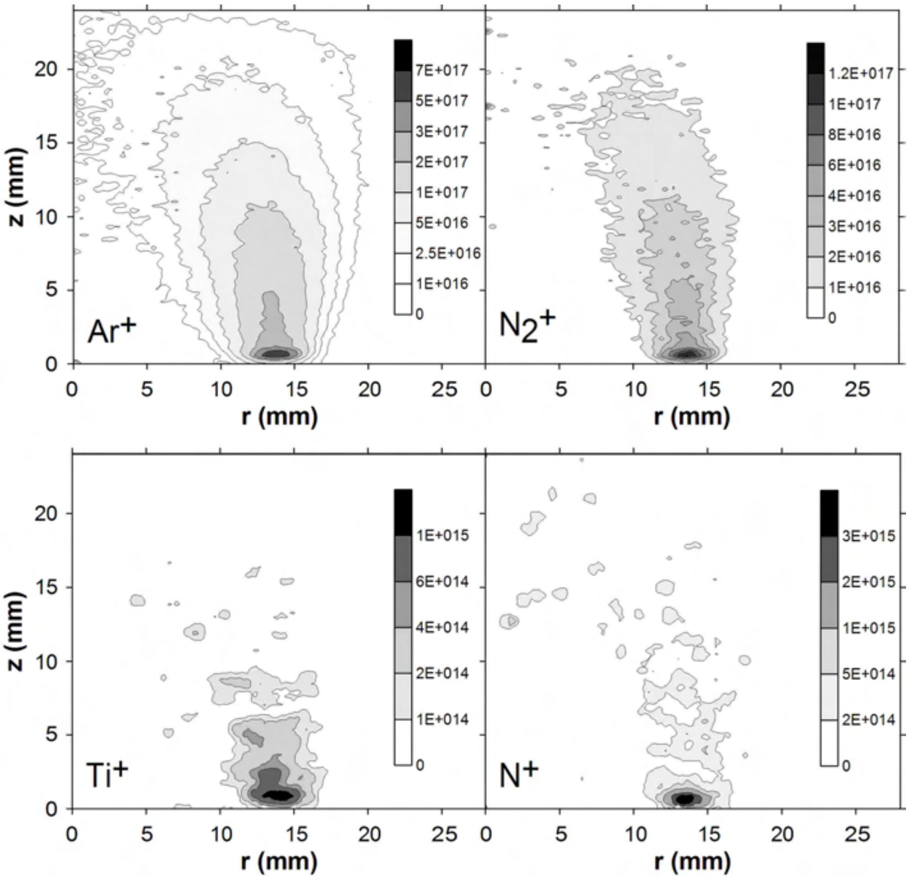

Figure 5.5: Calculated ion density profiles (in m^{-3}) at an Ar partial pressure of 1.0 Pa and a N_2 partial pressure of 0.26 Pa. Note that the y-axis (r=0) corresponds to the symmetry axis of the cylindrically symmetrical reactor.

As most of the fast Ar_f atoms originate from charge transfer reactions of Ar^+ ions, the typical Ar^+ ion peak profile appears for the fast Ar_f atoms as well, see figure 5.6. Its density is quite high, compared to the ion densities, but it is still two orders of magnitude lower than the overall background Ar gas density, which is about $2.4 \times 10^{20} m^{-3}$. Ti atoms originate from sputtering the cathode target, and therefore, the Ti density has a maximum near the cathode. Its overall density is four orders of magnitude lower than the total

Ar atom density.

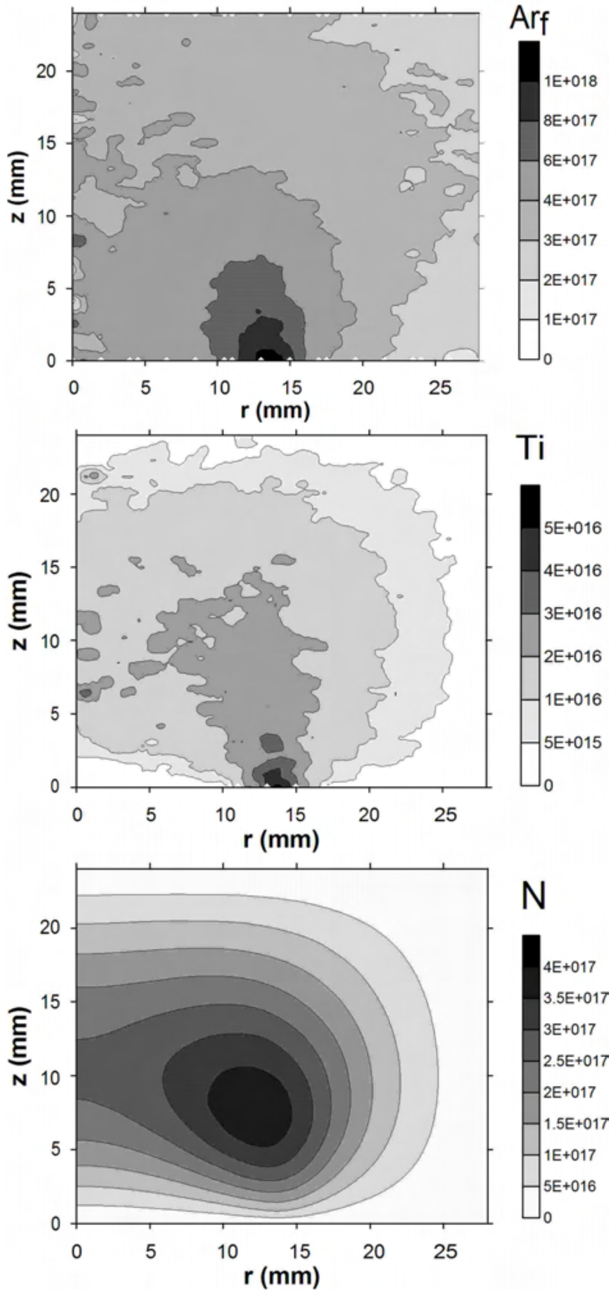

Figure 5.6: Calculated neutral density profiles (in m^{-3}) at an Ar partial pressure of 1.0 Pa and a N_2 partial pressure of 0.26 Pa. Note that the y-axis (r=0) corresponds to the symmetry axis of the cylindrically symmetrical reactor.

N atoms are also sputtered from the poisoned target, but most N atoms are created in the plasma instead of by sputtering (by reactions (13), (14), (15), (34) and (36) from table 5.1). As a consequence, the peak near the cathode is not so pronounced as in the case of the sputtered Ti atoms, and the N density is characterized by a broad profile throughout the discharge, as seen in figure 5.6. Also, the N density decreases towards the walls, because a sticking coefficient equal to 1 was assumed for N. Because N is not only created by sputtering but also by plasma reactions, the maximum value is almost an order of magnitude higher than the sputtered Ti atom density. Comparing the average N atom density, which is about $1.4 \times 10^{17} m^{-3}$, to the N_2 molecule density, which is about $6.2 \times 10^{19} m^{-3}$, reveals that the dissociation degree of N_2 is in the order of 0.2 %.

To investigate the influence of the N_2/Ar gas proportion on the various plasma species densities, 1D density profiles on a line perpendicular to the cathode at the peak density (i.e. r = 13.5 mm) are presented. Figure 5.7 illustrates the results for the Ti and N atoms.

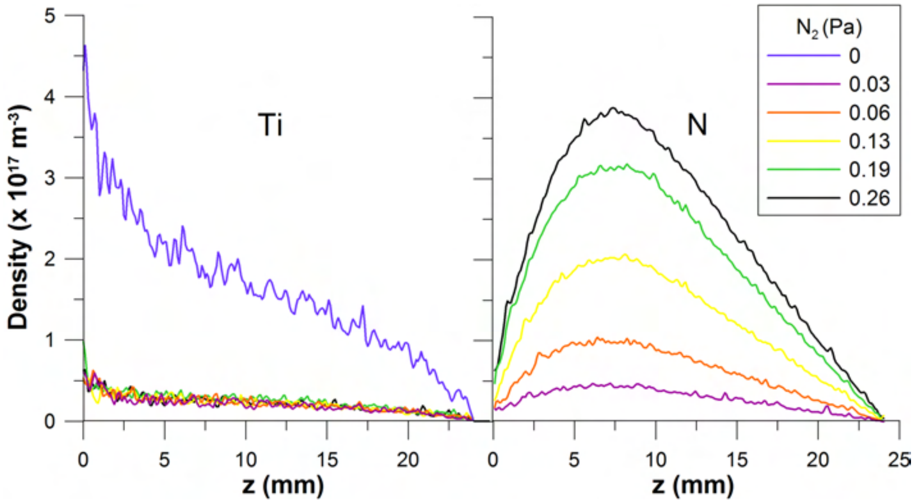

Figure 5.7: Calculated Ti and N atom densities above the cathode in the z-direction (at $r = 13.5$ mm), for different N_2 partial pressures as indicated in the legend, and at an Ar partial pressure of 1.0 Pa.

As a consequence of the difference in the Ti sputter yield for a metallic or a poisoned target (as mentioned in section 5.4 above, and as will be shown below in section 5.6.4), figure 5.7 shows that the Ti density drops significantly upon N_2 addition. However, when adding more N_2 gas, the Ti density remains constant. The N density rises logically with N_2 gas amount. The explanation for the profiles of the Ti and N densities was given in the paragraph above.

The influence of the N_2/Ar gas proportion on the 1D ion density profiles is shown in figure 5.8.

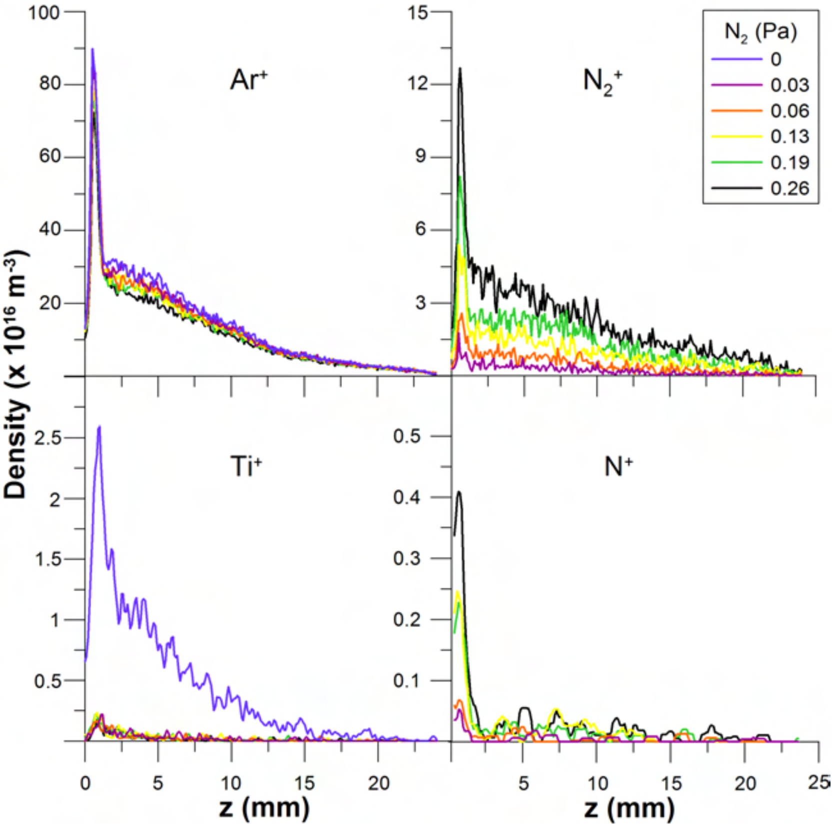

Figure 5.8: Calculated ion densities above the cathode in the z-direction (at r = 13.5 mm), for different N_2 partial pressures as indicated in the legend, and at an Ar partial pressure of 1.0 Pa.

Figure 5.8 demonstrates that the N^+ and N_2^+ densities increase when raising the N_2 gas pressure, whereas the Ar^+ density decreases slightly. This is explained as follows: the charge transfer reaction of Ar^+ with N_2, which causes the production of N_2^+ ions and the loss of Ar^+ ions, has a high rate constant (see reaction (21) of table 5.1). As a consequence, an increased N_2 gas amount leads to a higher N_2^+ density, but also to a lower Ar^+ density. The Ti^+ density drops approximately a factor of 10 when N_2 is added, similar to the Ti atom density (figure 5.7), caused by target poisoning.

Mass spectrometric measurements were carried out to determine the ion fractions at 7 cm from the cathode, for different N_2 gas concentrations. However, in order to keep the computation time reasonable, the size of the simulated magnetron reactor was limited to 2.4 cm. Hence, the ion fractions are calculated at 2 cm from the cathode. Nevertheless, it is assumed that the ion proportions will not vary much in the bulk of the plasma. From the measured and calculated ion fractions, presented in figure 5.9, we conclude that a good agreement with experiment is found, and similar trends as for the ion densities are observed. Only for the Ti^+ ions, the agreement is less satisfactory.

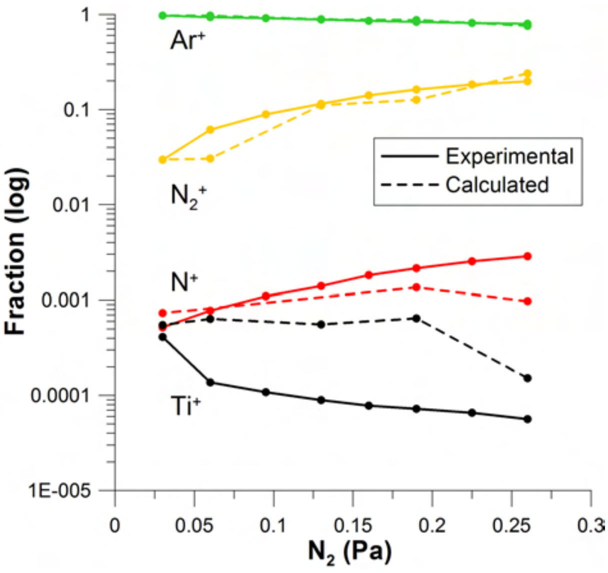

Figure 5.9: Experimental and calculated ion fractions as a function of N_2 partial pressure, at an Ar partial pressure of 1.0 Pa.

5.6.3 Ion and atom fluxes to the cathode

The ions accelerate towards the cathode by the applied electric field, where they can sputter the target. Also some neutrals contribute to the sputtering (see below). Therefore, in figure 5.10, the fluxes of the various species bombarding the cathode are plotted as a function of radial position for different N_2 concentrations.

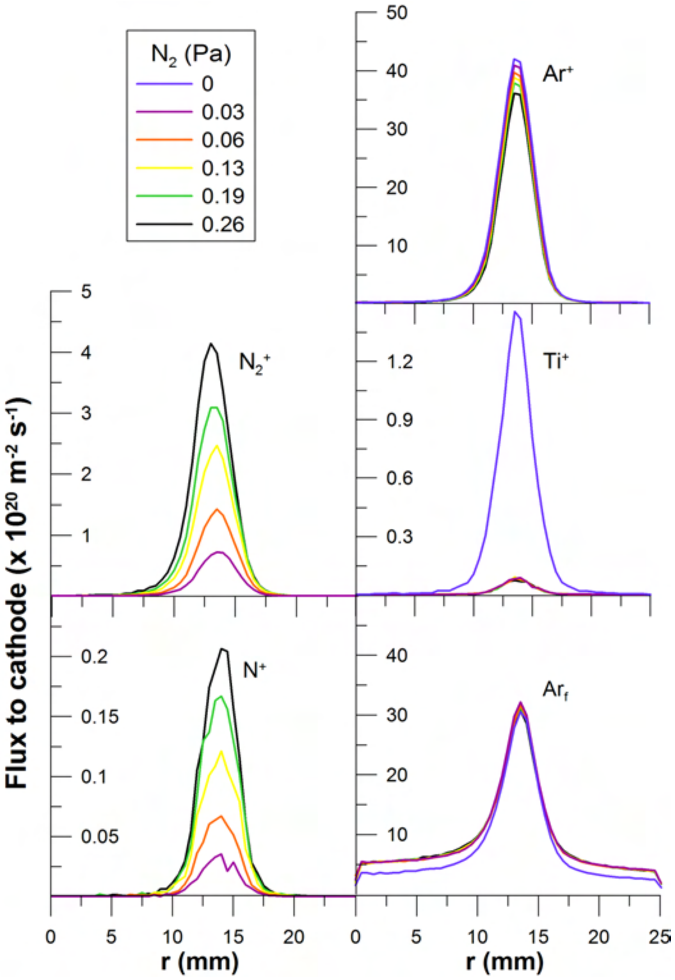

Figure 5.10: Calculated fluxes of the various ions and fast Ar_f atoms to the cathode for different N_2 partial pressures as indicated in the legend, at an Ar partial pressure of 1.0 Pa. Note that the y-axis (r=0) corresponds to the symmetry axis of the cylindrically symmetrical reactor.

The peak in figure 5.10 at 13.5 mm is a direct consequence of the maximum in the density profiles (see section 5.6.2 and figures 5.5 and 5.6 above). When the N_2 partial pressure is increased, the N_2^+ and N^+ fluxes increase and the Ar^+ flux decreases, in analogy to their densities (see section 5.6.2 and figure 5.8 above). The Ti^+ flux drops approximately a factor of 15 when N_2 is added. As was the case for the Ti^+ density (see section 5.6.2), this is a consequence of the lower Ti sputter yield when the target is poisoned (see also section 5.6.4 below). The fast Ar_f atom flux to the target is rather independent on the N_2 amount.

5.6.4 Ion and atom contributions to sputtering, and sputtered Ti and N fluxes

Depending on the magnitude of the fluxes, the corresponding energies, masses, and atom numbers, the above mentioned species contribute to the sputtering of the target (see equation (2.76) in chapter 2). In tables 5.3 and 5.4, the relative amount (in %) of Ti and N sputtering, respectively, created by each of these ions and atoms, is summarized.

Table 5.3: Calculated procentual contribution to the sputtering of Ti (from a Ti or a fully poisoned TiN_x target) of the different incident species, as a function of N_2 partial pressure, at an Ar partial pressure of 1 Pa.

Pressure (Pa)	Ar^+	Ar_f	N_2^+	N^+	Ti^+
0	87.13	9.71			3.00
0.03	87.49	11.15	0.97	0.04	0.16
0.06	86.31	11.37	1.86	0.10	0.15
0.13	85.26	11.92	3.24	0.19	0.17
0.19	84.09	10.99	4.36	0.19	0.16
0.26	83.40	10.54	5.35	0.29	0.19

Table 5.4: Calculated procentual contribution to the sputtering of N (from a fully poisoned TiN_x target) of the different incident species, as a function of N_2 partial pressure, at an Ar partial pressure of 1 Pa.

Pressure (Pa)	Ar^+	Ar_f	N_2^+	N^+	Ti^+
0.03	89.54	8.60	1.53	0.08	0.12
0.06	88.46	8.35	2.73	0.19	0.13
0.13	86.62	8.10	4.75	0.31	0.10
0.19	85.23	7.90	6.15	0.44	0.14
0.26	84.14	7.31	7.81	0.50	0.13

For both Ti and N, most sputtering is caused by bombarding Ar^+ ions, followed by fast Ar_f atoms. As mentioned before, these Ar_f atoms originate from elastic collisions (reaction (16)), including symmetric charge transfer collisions (reaction (17)), with Ar^+ ions [58]. The N_2^+ ions only play a role at high N_2 partial pressures, and more for sputtering N than Ti, because of the smaller mass differences, and hence the higher sputter yield. The role of N^+ and Ti^+ ions can be neglected under the investigated conditions, with a contribution of around 0.1-0.5 %. The order in contribution is a consequence of the magnitude of the fluxes, as was seen in figure 5.10. In general, raising the N_2 partial pressure causes an increase of the N_2^+ and N^+ contributions and a decrease of the Ar^+ contribution to the sputtering of both Ti and N. This can be explained by the dependence of the N_2^+, N^+, and Ar^+ fluxes on the N_2 partial pressure, as seen in section 5.6.3 and figure 5.10. From table 5.3, it is also clear that, when no N_2 gas is present, the contribution of Ti^+ to sputtering the metallic Ti target is a factor of 15 higher. This is a direct consequence of the behavior of the Ti^+ flux (section 5.6.3 and figure 5.10 above).

The total fluxes of sputtered Ti and N atoms are shown in figure 5.11. The maxima of the ion and atom fluxes towards the cathode (figure 5.10) cause a maximum in the sputter flux. This localized erosion creates the race track in the target. When no N_2 gas is added, the sputtered Ti flux is approximately a factor of 8 higher than after adding N_2, and hence poisoning the target, causing the sputter yield to decrease. As a consequence, the deposition rate of a pure Ti target will also be much higher than the deposition rate when the target is poisoned (see remarks below, in sections 5.6.5 and 5.6.6). Once the target is poisoned, the sputtered Ti flux remains constant and does not drop further upon N_2 addition.

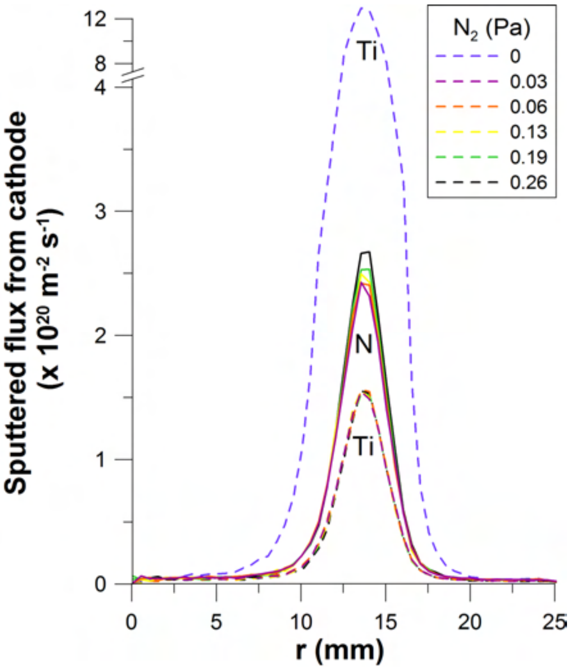

Figure 5.11: Calculated sputtered Ti (dashed lines) and N (solid lines) fluxes from the cathode for different N_2 partial pressures as indicated in the legend, and at an Ar partial pressure of 1.0 Pa. The lower part of the y-axis is stretched for clarity, because the sputtered Ti flux in pure Ar gas is much higher than in an Ar/N_2 mixture. Note that the y-axis (r=0) corresponds to the symmetry axis of the cylindrically symmetrical reactor.

The sputtered N flux is higher than the sputtered Ti flux due to the higher sputter yield of N (see above, section 5.4). However, the N sputter yield is four times higher than the Ti sputter yield (see section 5.4), whereas the sputter fluxes differ a factor of less than two. This is caused by another effect, i.e. the threshold energy for sputtering Ti by Ar^+ ions (the main sputter source in the discharge) is lower than for sputtering N by Ar^+ ions. As a consequence, the sputtered N and Ti fluxes will lie closer to each other than predicted by the sputter yields.

Moreover, in contrast to the Ti flux, the sputtered N flux increases slightly with increasing the N_2 partial pressure. This is a consequence of the dependence of the N or Ti sputter yield on the different incoming species. Indeed, sputtering N with N_2^+ or N^+ ions has a larger yield than with Ar^+ ions, whereas sputtering Ti is less dependent of the bombarding ion type. With increasing the N_2 pressure, the N_2^+ and N^+ fluxes increase (see section 5.6.3 and figure 5.10), causing an enhanced sputtering of N.

5.6.5 Ti, N and N_2 fluxes to the substrate

In order to obtain a better insight in the deposition of TiN_x films, the calculated fluxes of Ti, N and N_2 to the substrate are presented in figure 5.12. Obviously, the case of pure Ar is omitted, since we are interested in the deposition of a TiN_x film. Note, however, that the Ti flux to the substrate in a pure Ar discharge is a factor of eight higher, as a consequence of the higher sputtered Ti flux (see section 5.6.4 and figure5.11). This causes the deposition rate of Ti to be eight times higher in a pure Ar discharge, compared to an Ar/N_2 mixture.

The Ti flux to the anode is characterized by a similar radial peak profile as the sputtered Ti flux, implying that the deposited Ti in the film will be non-uniform. The broadening of the peak profile is a consequence of diffusion of the sputtered Ti atoms through the plasma.

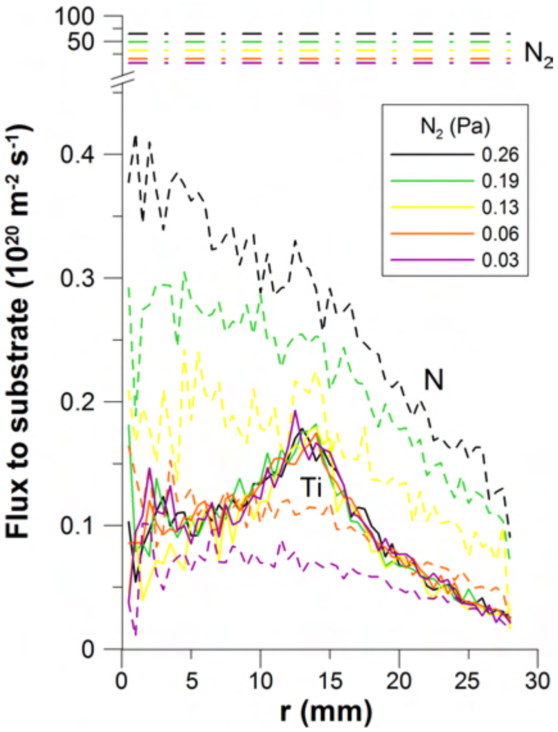

Figure 5.12: Calculated fluxes of the Ti, N and N_2 species to the substrate, as a function of radial position, for different N_2 partial pressures, at an Ar partial pressure of 1 Pa. Note that the y-axis (r=0) corresponds to the symmetry axis of the cylindrically symmetrical reactor.

The N flux has lost its radial peak profile, as was also clear from the N density (see section 5.6.2 and figure 5.6), because more N is created by plasma reactions than by sputtering. The N flux increases with N_2 amount, similar to the N density (see figure 5.7).

Finally, the N_2 flux at the substrate has a uniform profile. Indeed, under the investigated gas pressures, gas heating is negligible [118]. Therefore, the Ar and N_2 gas densities remain constant and uniform (see also equation 2.86). As for the N flux, the N_2 flux rises upon N_2 addition.

When the absolute values of the fluxes of Ti, N and N_2 to the substrate are compared (figure 5.12), and if constant sticking coefficients of 0.5, 1 and 0.3, respectively, would be used, the deposited TiN_x film would have a stoichiometry x much larger than one. This emphasizes the importance of using effective sticking coefficients, which depend on the deposited TiN fraction on the substrate, instead of constant sticking coefficients.

5.6.6 Deposition of a TiN_x film on the substrate

Based on the fluxes of the Ti, N and N_2 species, the compound fraction on the substrate is calculated by equation (5.2), and it is presented in figure 5.13. Equation (5.2) implies that the compound fraction is inversely proportional to the Ti flux, leading to a drop in the compound fraction profile at 13.5 mm from the center. On the other hand, at increasing N_2 gas pressure, the N_2 and N fluxes increase, resulting in a higher compound fraction close to unity. This trend was also calculated with the analytical "Berg-model" [30].

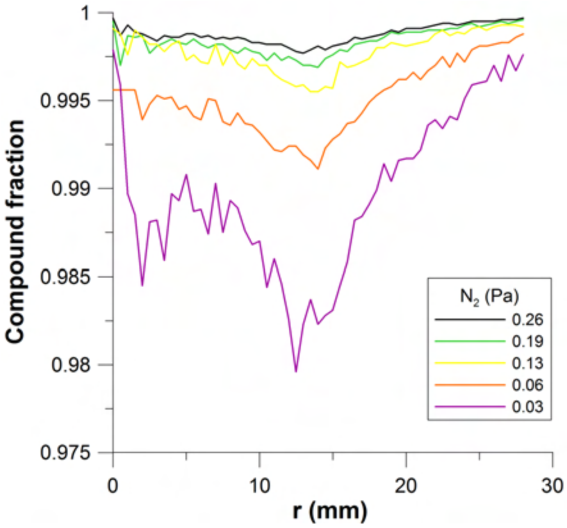

Figure 5.13: Calculated compound fraction of the substrate surface, as a function of radial position, for different N_2 partial pressures, at an Ar partial pressure of 1 Pa. Note that the y-axis (r=0) corresponds to the symmetry axis of the cylindrically symmetrical reactor.

Moreover, the profile flattens because it is less affected by the Ti flux, whereas the N and N_2 fluxes gain importance in the compound fraction, and they have a more uniform profile compared to the peaking Ti flux. Physically, this implies that at higher N_2 pressure, the deposited film consists mainly of compound material, whereas at lower N_2 pressure, a certain fraction of pure Ti is deposited. However, figure 5.13 shows that this fraction is very small at the conditions under study.

Based on the radial compound fraction, the constant SC values of N and N_2 are adapted, according to equation 5.3. The calculated effective SC values (SC_{eff}) of N and N_2 are presented in figure 5.14. It is clear that the SC_{eff} values are not constant, but they exhibit a radial dependence, being lowest at the highest compound fraction. Considering the initial SC values of N and N_2, i.e. 1 and 0.3, the effective values have dropped about a factor of 50-500, as can be deduced from figure 5.14. Note that the SC_{eff} plots of both N and N_2 exhibit exactly the same profile, which is a consequence of equation 5.3. Moreover, the effective sticking of the N and N_2 species decreases at increasing N_2 gas pressure, as a result of the higher compound fraction.

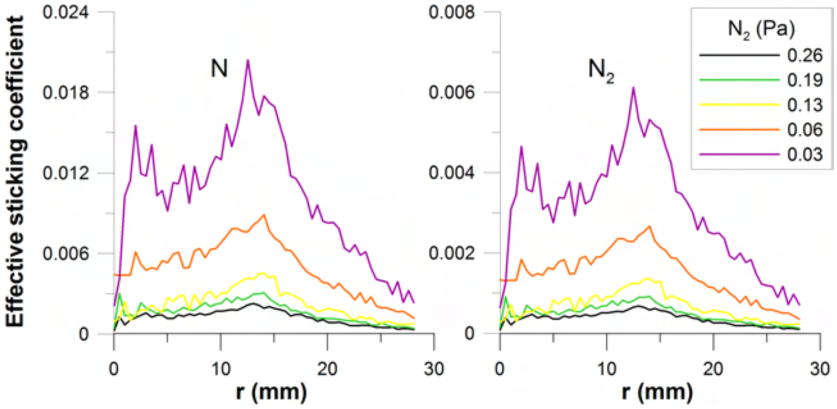

Figure 5.14: Calculated effective sticking coefficients of N and N_2, as a function of radial position, for different N_2 partial pressures, at an Ar partial pressure of 1 Pa. Note that the y-axis (r=0) corresponds to the symmetry axis of the cylindrically symmetrical reactor.

When the fluxes of Ti, N and N_2 (figure 5.12) are multiplied by the corresponding SC_{eff} values, the deposition rate of N and Ti can be calculated.

Figure 5.15 shows the total deposition rate of N, i.e. the sum of the deposition rates due to N and N_2 (note that N_2 counts double, because one N_2 molecule gives rise to two deposited N atoms), and the deposition rate of Ti, at N_2 partial pressures of 0.03, 0.06, and 0.26 Pa. As mentioned before, the Ti deposition rate in an Ar/N_2 mixture is calculated to be eight times lower than the Ti deposition rate in a pure Ar discharge, as a consequence of the lowered sputtered Ti flux from a poisoned target (not shown here).

Similar to the Ti deposition rate, the N deposition rate, displayed in figure 5.15, exhibits a peak profile, because of the radially dependent SC_{eff} values (figure 5.14). Hence, the peak profile in figure 5.15 predicts the non-uniformity of the TiN_x film thickness (i.e. thicker above the race track of the target), under the investigated conditions. Note that in our case the target-substrate distance is only 2.4 cm (to keep the calculation time reasonable). In experiments, on the other hand, a more uniform film can be deposited by placing the substrate further from the target so that the fluxes to the substrate are smoothened.

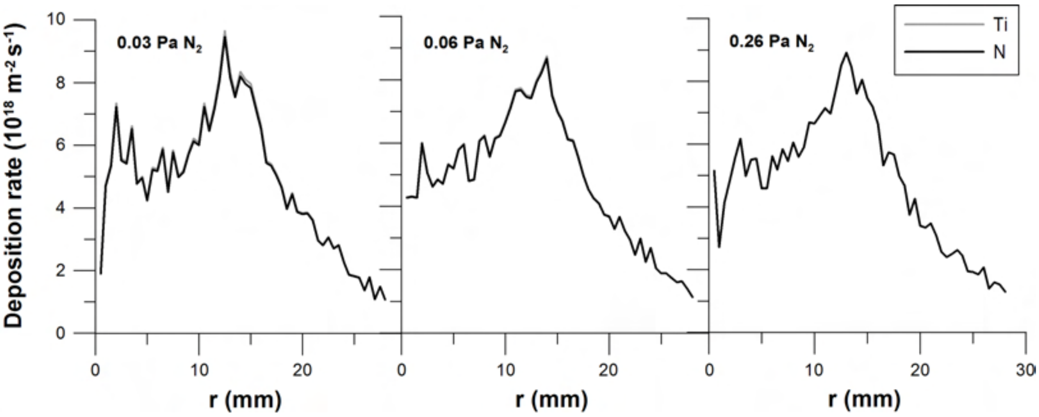

Figure 5.15: Calculated deposition rates of Ti and (total) N, for different N_2 partial pressures, and an Ar partial pressure of 1 Pa. Note that the y-axis (r=0) corresponds to the symmetry axis of the cylindrically symmetrical reactor.

It can also be observed from figure 5.15 that the Ti deposition rate remains constant upon N_2 addition, as was anticipated from figure 5.12. The total

N deposition rate is already very close to the Ti deposition rate at lowest N_2 pressure, and increases until it becomes equal to the Ti deposition rate, in order to aspire a TiN_x film with a stoichiometry x=1 (imposed by equations 5.1 and 5.2). Figure 5.15 therefore indicates that at higher N_2 amount, the film tends to a stoichiometric TiN deposition. This was also predicted above: figure 5.13 implies that the deposited film will have a more uniform compound fraction, closer to one, leading to a stoichiometry x, nearly equal to one, at the higher N_2 gas pressure (remember that the actual stoichiometry (x) of the deposited TiN_x film equals the desired stoichiometry (x=1) times the compound fraction (θ_{cs})).

If the surface model would not be applied, the total deposition rate, i.e. the product of the flux (figure 5.12) and the constant SC values (1 for N, 0.3 for N_2 and 0.5 for Ti) of N would be much higher than the deposition rate of Ti, causing an overstoichiometry in the deposited film, i.e. x of TiN_x would be much larger than one (in the order of 100-1000). This implies that the coupling of an analytical surface model to a PIC/MCC model is inevitable for a correct description of the deposition process.

The deposition of a stoichiometric TiN film at similar conditions was also observed in analytical calculations (in terms of the compound fraction) [30], and in experiments [17, 119].

In figure 5.16, the ratio of the N and N_2 contributions to the total N deposition rate is presented, at N_2 partial pressures of 0.03, 0.06, and 0.26 Pa. It is clear from figure 5.16 that the total deposition rate of N due to N_2 is much higher than the deposition rate due to N, i.e. at least 50 times higher (at the lowest N_2 pressure), despite the lower SC_{eff} of N_2. This is because the flux of N_2 molecules to the substrate is so high, i.e. more than two orders of magnitude higher than the N atom flux, whereas the SC_{eff} is only a factor of three lower.

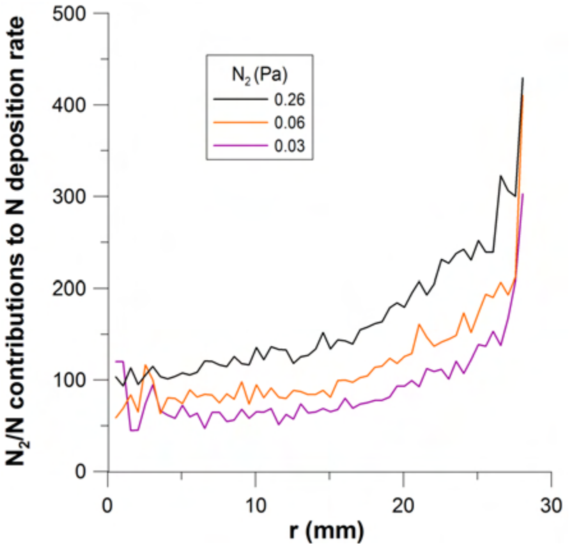

Figure 5.16: Calculated ratio of N_2/N contributions to the total N deposition rate, for different N_2 partial pressures, and an Ar partial pressure of 1 Pa. Note that the y-axis (r=0) corresponds to the symmetry axis of the cylindrically symmetrical reactor.

5.7 Conclusion

To simulate the physical processes in a magnetron discharge during reactive sputter deposition, a 2d3v particle-in-cell/Monte Carlo collisions modeling approach was applied. The plasma species taken into account are electrons, Ar^+ ions, fast Ar_f atoms, metastable Ar^*_m atoms, Ti^+ ions, Ti atoms, N^+ ions, N_2^+ ions, and N atoms. The model includes plasma-surface interactions, such as species reflection, secondary electron emission, target sputtering, the effects of a poisoned target (on *SEEC* and sputter yield), and atom sticking. The deposition process of the TiN_x film was visualized by coupling an analytical surface model for the substrate to the PIC/MCC model. As such, the PIC/MCC model calculates species fluxes to the substrate, which are used in the analytical surface model to calculate the radial compound fraction and the effective sticking coefficient. Based on the effective sticking coefficients, the actual stoichiometry and deposition rate of the TiN_x film at various N_2/Ar proportions can be predicted.

With this combined model, we are able to calculate in detail the plasma characteristics, such as densities and fluxes of the various species in the whole reactor. The influence of the N_2/Ar gas ratio on the plasma species densities and fluxes was investigated. The model was validated by comparing calculated ion fractions to mass spectrometric measurements. Moreover, the fluxes and contribution of various species bombarding the cathode target were calculated, emphasizing the importance of fast Ar_f atoms, after Ar^+ ions, for the sputtering process. Also, the influence of a poisoned target on the sputtered fluxes was illustrated, i.e. the sputtered Ti flux drops strongly after transition from a metallic to a poisoned mode.

Finally, it was shown that at higher N_2 pressure, the film has a more uniform compound fraction, closer to one, which results in a (nearly) stoichiometric TiN film. The total deposition rate of N due to N_2 is much higher than the deposition rate due to N: N_2 contributes at least 50 times more to the total deposition rate of nitrogen in the film, than N atoms.

Chapter 6

Ar/O_2 mixture: reactive sputter deposition of TiO_x

6.1 Introduction

In order to deposit a metal oxide layer, oxygen gas is added to the argon discharge. In analogy to the mechanisms in an Ar/N_2 magnetron discharge, O_2 gas molecules themselves and O atoms from this gas can react with the sputtered metal atoms on the substrate to form a metal oxide layer [9,19,20] (figure 1.2 above is also valid for the Ar/O_2 discharge). These metal oxide films are manufactured because of their interesting tribological properties [120–123], such as anti-reflective, anti-static, hard, and corrosion and wear resistant. Certain metal oxide films are beneficial due to interesting electrical properties [120].

Reactive magnetron sputter deposition for an Ar/O_2 gas mixture has been investigated in the literature by analytical models, such as [30, 31], and by MCC models [40]. As far as we know, only one PIC/MCC model exists for an Ar/O_2 magnetron discharge [46]. However, this PIC/MCC model does not take into account plasma-surface interactions, such as target sputtering, target poisoning, and atom sticking, i.e. the sputter deposition process itself is not described. Albeit, these plasma-surface interactions influence all of the calculated discharge characteristics [21,23]. Secondly, the external circuit was not included in the model of [46]. Nevertheless, the external circuit occurs to be inevitable in a PIC/MCC code for an accurate and correct description of magnetron discharges, as was demonstrated in chapter 3 above.

In our opinion, the PIC/MCC modeling approach produces the most elaborate and accurate data to simulate magnetron discharges. However a complete PIC/MCC model, which includes both an external circuit as well as plasma-surface interactions does not yet exist to describe the reactive sputter deposition in an Ar/O_2 gas mixture in a magnetron discharge. Therefore, to study the reactive magnetron sputter deposition process of TiO_x layers, a PIC/MCC model including plasma-surface interactions is developed and presented in this chapter. The plasma-surface interactions comprise the influence of a poisoned target on the $SEEC$ and the sputter yield. Moreover, the effective sticking coefficients of Ti, O and O_2 are calculated with an analytical surface model [30,31,68] to picture the deposition process of a TiO_x film on the substrate (see also section 2.4 above).

The effect of the O_2/Ar ratio on current-voltage characteristics, on the plasma potential distribution, and on different plasma species densities is calculated. Moreover, sputtered Ti and O fluxes from the target are calculated for different O_2/Ar proportions, as well as Ti, O and O_2 fluxes to the substrate. The coupled analytical surface model enables to describe the deposition process of the TiO_x film, in terms of the deposited TiO_x fraction, the Ti and O deposition rates and the film stoichiometry x. Moreover, a comparison is made between the sputter deposition of TiN_x and TiO_x layers.

6.2 Description of the magnetron discharge and simulated conditions

The simulated magnetron setup in this chapter is the same as in the previous chapters, see section 3.2 and figure 2.1. The discharge conditions are also the same as in the previous chapter, i.e. chapter 5. Moreover, similar to the Ar/N_2 study, the O_2 partial pressure is increased to investigate its effect on the calculated discharge characteristics. However, these values are slightly different from the N_2 partial pressures, since they are measured in the experiments: it is increased as 0.02, 0.06, 0.12, 0.18, and 0.24 Pa. Again, under these conditions, the target is always fully poisoned, in analogy to the Ar/N_2 discharge.

6.3 Overview of the model

The model for the Ar/O_2 discharge is similar to the models discussed in the previous chapters, and the details are described in chapter 2. To include the species and collisions which are present in an Ar/O_2 magnetron discharge, the model developed for the Ar/N_2 mixture is adapted. The included oxygen species and collisions are summarized in section 6.5. Moreover, the influence of a poisoned target on the plasma-surface interactions, i.e. on secondary electron emission and on sputtering is included. Finally, the coupling of the analytical surface model to the PIC/MCC model accounts for the deposition process (see section 6.4 below).

6.4 Plasma-surface interactions

The *RC* and *SEEC* values of the metallic Ti target were derived in chapter 5. Similar to the procedure to find the *SEEC* values of a poisoned TiN_x target, the *SEEC* values of a fully poisoned TiO_x target are derived (see values below, in section 6.6.1).

In analogy to the previous chapter, both Ti and O atoms can be sputtered from a poisoned TiO_x target, but with a lower sputter yield than for a metallic Ti target. Therefore, in the model, the sputter yield, calculated with the formula of Matsunami [63], is lowered with a factor, in accordance to the values reported in [66]: the sputter yield of Ti from a fully poisoned TiO_x

target is lowered with a factor of 8.8 compared to the sputter yield of Ti from a metallic target, and the sputter yield of O from a fully poisoned target is two times higher, compared to the sputter yield of Ti from a poisoned target [66].

The analytical surface model used in chapter 5 is adapted to account for the deposition of TiO$_x$ on the substrate with a desired stoichiometry of $x = 2$. For details, we refer to the theory described in section 2.4.4, and to the similar derivation in section 5.4. A compound fraction balance equation for the deposition of a TiO$_x$ film with desired stoichiometry x=2 is constructed from equation 2.81:

$$SC_{O_2}F_{O_2}(1-\theta_{cs}) + \frac{1}{2}SC_OF_O(1-\theta_{cs}) = SC_{Ti}F_{Ti}\theta_{cs} \tag{6.1}$$

With this equation, the already deposited TiO$_2$ fraction, θ_{cs}, can be found from the Ti, O, and O$_2$ fluxes and their corresponding SC values:

$$\theta_{cs} = \frac{SC_{O_2}F_{O_2} + \frac{1}{2}SC_OF_O}{SC_{O_2}F_{O_2} + \frac{1}{2}SC_OF_O + SC_{Ti}F_{Ti}} \tag{6.2}$$

The constant SC values are chosen as 0.3 for O$_2$ [22], 1 for O [22] and 0.5 for Ti [67]. These constant SC values of O and O$_2$ are adapted by θ_{cs}, so that we obtain the effective sticking coefficients, SC_{eff}:

$$\begin{aligned} SC_{O_2,eff} &= SC_{O_2}(1-\theta_{cs}) \\ SC_{O,eff} &= SC_O(1-\theta_{cs}) \end{aligned} \tag{6.3}$$

As mentioned in the previous chapter, the sticking of Ti is independent on the compound fraction. Therefore, a constant SC_{Ti} can be used: $SC_{Ti,eff} = SC_{Ti}$. Note that the actual stoichiometry of the deposited TiO$_x$ film, x, is found by multiplying the desired stoichiometry, x=2, by the compound fraction, θ_{cs}.

6.5 Included collisions

Similar to the Ar/N_2 model, certain species are included in the Ar/O_2 model: electrons, Ar^+ ions, metastable Ar_m^* atoms, fast Ar_f atoms Ti^+ ions, and Ti atoms, O^+ ions, O_2^+ ions, and O atoms. In this model, also the negative O^- ions are included. The list of the considered collisions in the Ar/O_2 discharge, and their rate constants and references to their cross sections is given in table 6.1. Some cross sections of ion-neutral collisions are described with the Langevin-Hasse model [114, 115], see section 5.5, assigned "LH" in table 6.1. Here, the value of β_∞ is set to 3 for Ar, O_2 and O [115]. The polarizability of O_2 is 10.60 a_0^3 [86] and 5.4 a_0^3 for O [86].

Table 6.1: List of the collisions considered in the model. The references where the cross sections ($\sigma(E)$) or rate constants (k) were adopted from are presented in the last column. The rate constants are in $m^3\ s^{-1}$ for two-body collisions and $m^6\ s^{-1}$ for three body collisions (indicated by*). "(a)" refers to assumed rate constants based on similar reactions, due to lack of data in the literature. "LH" refers to the Langevin-Hasse treatment for the cross section (see section 5.5).

e^- collisions				
(1)	$e^- + Ar \rightarrow e^- + Ar$	elastic scattering	$\sigma(E)$	[79]
(2)	$e^- + Ar \rightarrow 2e^- + Ar^+$	electron-impact ionization	$\sigma(E)$	[80]
(3)	$e^- + Ar \rightarrow e^- + Ar_m^*$	electron-impact excitation	$\sigma(E)$	[81]
(4)	$e^- + Ar \rightarrow e^- + Ar^*$	electron-impact excitation	$\sigma(E)$	[82]
(5)	$e^- + Ar_m^* \rightarrow 2e^- + Ar^+$	electron-impact ionization	$\sigma(E)$	[92]
(6)	$e^- + Ar_m^* \rightarrow e^- + Ar^*$	electron-impact excitation	$\sigma(E)$	[93]
(7)	$e^- + Ti \rightarrow 2e^- + Ti^+$	electron-impact ionization	$\sigma(E)$	[94]
(8)	$e^- + O_2 \rightarrow 2e^- + O_2^+$	electron-impact ionization	$\sigma(E)$	[110, 124]
(9)	$e^- + O_2 \rightarrow e^- + O_2^*(a)$	electron-impact excitation to $a^1\Delta_g$	$\sigma(E)$	[110]
(10)	$e^- + O_2 \rightarrow e^- + O_2^*(b)$	electron-impact excitation to $b^1\Sigma_g^+$	$\sigma(E)$	[110]
(11)	$e^- + O_2 \rightarrow O^- + O$	dissociative attachment	$\sigma(E)$	[110]
(12)	$e^- + O_2 \rightarrow e^- + O^- + O^+$	ion pair formation	$\sigma(E)$	[46]
(13)	$e^- + O_2 \rightarrow 2e^- + O^+ + O$	dissociative ionization	$\sigma(E)$	[110]
(14)	$e^- + O_2 \rightarrow e^- + O + O$	dissociation	$\sigma(E)$	[110]
(15)	$e^- + O_2^+ \rightarrow O + O$	dissociative recombination	$k = 2 \times 10^{-13}(300/T_e)$	[125, 126]
(16)	$e^- + O^+ + O_2 \rightarrow O + O_2$	recombination	$k = 6 \times 10^{-39}(300/T_e)^{1.5}$ *	[126]
(17)	$e^- + O^- \rightarrow 2e^- + O$	neutralization	$k = 1.95 \times 10^{-18}$	[127]

Table 6.2: Table 6.1 continued.

Ar^+ collisions				
(18)	$Ar^+ + Ar \rightarrow Ar^+ + Ar$	elastic scattering	$\sigma(E)$	[58]
(19)	$Ar^+ + Ar \rightarrow Ar + Ar^+$	charge transfer	$\sigma(E)$	[58]
(20)	$Ar^+ + Ar \rightarrow 2Ar^+ + e^-$	ion-impact ionization	$\sigma(E)$	[83]
(21)	$Ar^+ + Ar \rightarrow Ar^+ + Ar^*_m$	ion-impact excitation	$\sigma(E)$	[83]
(22)	$Ar^+ + Ti \rightarrow Ar + Ti^+$	charge transfer	$k = 6.61 \times 10^{-17}$	[95]
(23)	$Ar^+ + O_2 \rightarrow Ar^+ + O_2$	elastic scattering	$\sigma(E)$ LH	[46]
(24)	$Ar^+ + O_2 \rightarrow Ar + O_2^+$	charge transfer	$k = 5.1 \times 10^{-17}$	[128]
(25)	$Ar^+ + O \rightarrow Ar^+ + O$	elastic scattering	$\sigma(E)$ LH	
(26)	$Ar^+ + O \rightarrow Ar + O^+$	charge transfer	$k = 6.4 \times 10^{-18}$	[128]
Ar^*_m collisions				
(27)	$Ar^*_m + Ar^*_m \rightarrow Ar + Ar^+ + e^-$	metastable-metastable collision	$k = 6.4 \times 10^{-16}$	[96, 97]
(28)	$Ar^*_m + Ti \rightarrow Ar + Ti^+ + e^-$	Penning ionization	$\sigma = 4.93 \times 10^{-19}$	[98]
(29)	$Ar^*_m + Ar \rightarrow Ar + Ar$	two-body collision	$k = 2.3 \times 10^{-21}$	[99]
Ar_f collisions				
(30)	$Ar_f + Ar \rightarrow Ar_{(f)} + Ar_{(f)}$	elastic scattering	$\sigma(E)$	[100]
(31)	$Ar_f + Ar \rightarrow Ar + Ar^+$	atom-impact ionization	$\sigma(E)$	[83]
(32)	$Ar_f + Ar \rightarrow Ar_f + Ar^*_m$	atom-impact excitation	$\sigma(E)$	[101]
Ti^+ collisions				
(33)	$Ti^+ + Ar \rightarrow Ti^+ + Ar$	elastic scattering	$\sigma = 6 \times 10^{-20}$	[102]
(34)	$Ti^+ + O_2 \rightarrow Ti^+ + O_2$	elastic scattering	$\sigma(E)$	LH
(35)	$Ti^+ + O \rightarrow Ti^+ + O$	elastic scattering	$\sigma(E)$	LH
Ti collisions				
(36)	$Ti_f + Ar \rightarrow Ti + Ar_f$	elastic scattering	$\sigma = 6 \times 10^{-20}$	[102]
(37)	$Ti + 2O \rightarrow TiO_2$	attachment	only at the walls (SC)	
O^+ collisions				
(38)	$O^+ + Ar \rightarrow O^+ + Ar_f$	elastic scattering	$\sigma(E)$ LH	[46]
(39)	$O^+ + Ar \rightarrow O + Ar^+$	charge transfer	$k = 3 \times 10^{-17}$	(a)
(40)	$O^+ + O_2 \rightarrow O^+ + O_2$	elastic scattering	$\sigma(E)$ LH	[46]
(41)	$O^+ + O_2 \rightarrow O + O_2^+$	charge transfer	$k = 3.3 \times 10^{-17}$ $\times e^{-0.00169.T_{gas}}$	[125, 126]
(42)	$O^+ + O_3 \rightarrow O_2^+ + O_2$	atom transfer	$k = 1 \times 10^{-16}$	[126]
O_2^+ collisions				
(43)	$O_2^+ + Ar \rightarrow O_2^+ + Ar$	elastic scattering	$\sigma(E)$	LH
(44)	$O_2^+ + Ar \rightarrow O_2 + Ar^+$	charge transfer	$k = 3 \times 10^{-17}$	(a)
(45)	$O_2^+ + O_2 \rightarrow O_2^+ + O_2$	elastic scattering	$\sigma(E)$	LH
(46)	$O_2^+ + O_2 \rightarrow O_2 + O_2^+$	charge transfer	$k = 3 \times 10^{-17}$	(a)
O^- collisions				
(47)	$O^- + Ar \rightarrow O^- + Ar$	elastic scattering	$\sigma(E)$ LH	[46]
(48)	$O^- + O_2 \rightarrow O^- + O_2$	elastic scattering	$\sigma(E)$ LH	[46]
(49)	$O^- + O_2 \rightarrow e^- + O_3$	recombination	$k = 5 \times 10^{-21}$	[126]
(50)	$O^- + O_2(a) \rightarrow e^- + O_3$	recombination	$k = 3 \times 10^{-16}$	[125, 126]
(51)	$O^- + O_2(b) \rightarrow e^- + O + O_2$	recombination	$k = 6.9 \times 10^{-16}$	[125, 126]
(52)	$O^- + O \rightarrow e^- + O_2$	recombination	$k = 5 \times 10^{-16}$	[126]
(53)	$O^- + O^+ \rightarrow O + O$	recombination	$k = 2 \times 10^{-13}(300/T_{gas})^{0.5}$	[126]
(54)	$O^- + O_2^+ \rightarrow O + O + O$	recombination	$k = 1 \times 10^{-13}$	[126]
(55)	$O^- + O_2^+ \rightarrow O + O_2$	recombination	$k = 2 \times 10^{-13}(300/T_{gas})^{0.5}$	[126]

In addition to the cross section data from figure 3.1 and 4.1, the newly added electron-impact cross sections are plotted against electron energy in figure 6.1.

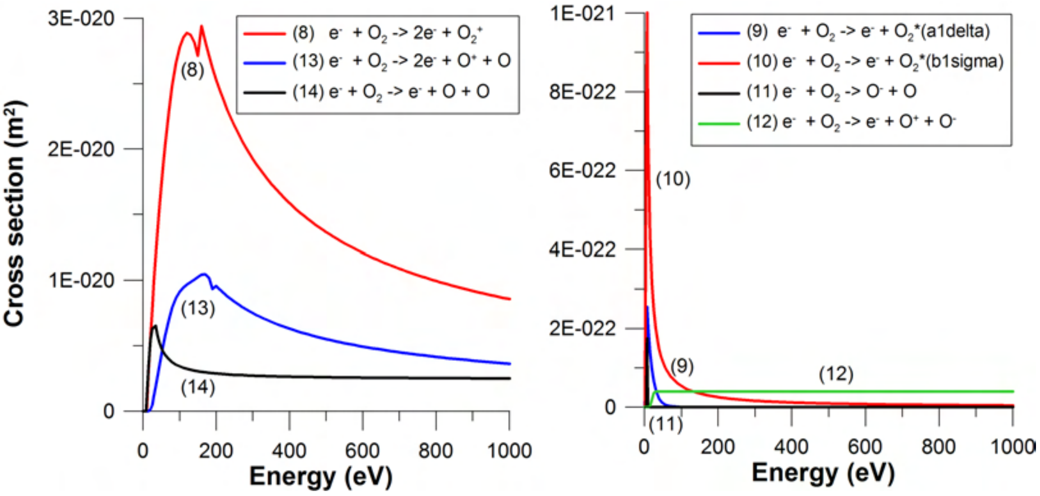

Figure 6.1: Cross section data of the additional electron-impact collisions (apart from the collisions which cross section data are illustrated in figures 3.1 and 4.1), included in the model. The references where this data is adopted from are given in table 6.1.

6.6 Results and discussion

6.6.1 Current-voltage characteristics

From previous calculations in pure Ar gas at 1 Pa, it was found that a RC of 0.1 and a $SEEC$ of 0.075 yielded calculated $I-V$ values in good agreement with the experimental data (see section 5.6.1 above). When adding O_2 gas in amounts for which the target is completely poisoned, the $SEEC$ value will change, and in the case of a poisoned TiO_x target, the $SEEC$ is lower compared to the pure metallic Ti surface [61]. In figure 6.2 it is shown how the $SEEC$ value depends on the amount of O_2 in the discharge. The $SEEC$ jumps from the value of the metallic target, 0.075, to the value of the poisoned target, 0.050, and decreases slightly afterwards to 0.035. This slight decrease is caused by the fact that the $SEEC$ value in the model represents the global $SEEC$ of all bombarding particles, rather than the separate $SEEC$ values of the different incident species (as was already explained in the previous chapter, section 5.6.1).

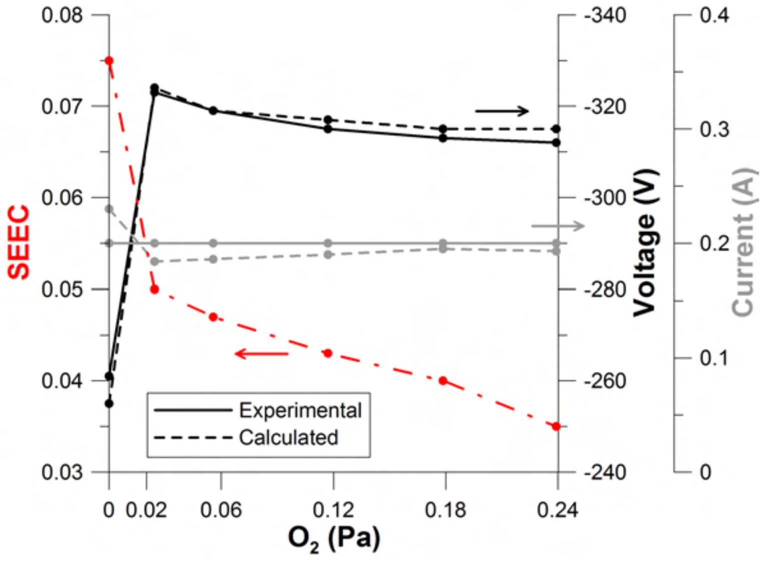

Figure 6.2: Measured and calculated values of the cathode potentials and currents as a function of O_2 partial pressure, at an Ar partial pressure of 1.0 Pa, an external voltage (V_{ext}) of -600 V, and an external resistance (R_{ext}) of 1500 Ω. The $SEEC$ values used in the model for different O_2 partial pressures are also indicated.

Figure 6.2 also presents the $I - V$ characteristics calculated with the aforementioned $SEEC$ values, an external resistance of $R_{ext} = 1500\ \Omega$, an external voltage of $V_{ext} = -600$ V, and a RC of 0.1. With these input values, the Ar/O_2 discharge operates in a constant current regime of 0.2 A, and the voltage decreases upon O_2 addition (caused by the changing $SEEC$ value). Also, the experimental $I - V$ values are presented.

6.6.2 Charged species density profiles, and potential distribution

When an external magnetic field is present, electrons are confined to the magnetic field lines, leading to a higher electron density at the maximum radial magnetic field, as presented in figure 6.3 (for the case of 0.12 Pa O_2). The electron density is only weakly dependent on the O_2/Ar proportion. Therefore, the electron density profiles at the other O_2 partial pressures are not shown here. When this electron density is compared to the electron density in the Ar/N_2 magnetron discharge at similar conditions (figure 5.3), it is clear that the electron density does not depend on the type of reactive gas.

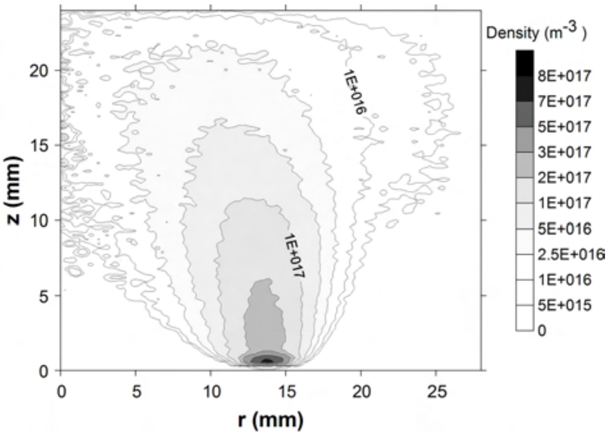

Figure 6.3: Calculated electron density profile (in m^{-3}) at an Ar partial pressure of 1.0 Pa and an O_2 partial pressures of 0.12 Pa. Note that the y-axis (r=0) corresponds to the symmetry axis of the cylindrically symmetrical reactor.

The electrons ionize neutral Ar, O_2, O and Ti species, causing the positive ion density to be highest in the same area. All have similar profiles as the electron density so they are not shown here. The Ar^+ density has approximately the same magnitude as the electron density, the O^+ and O_2^+ densities are two orders of magnitude lower (the latter is shown in figure 6.4), and the Ti^+ density is three orders of magnitude lower. Both the Ar^+ and the Ti^+ density do not change much with O_2/Ar ratio. However, the O^+ and O_2^+ densities rise with O_2 gas pressure: the O_2^+ density is presented in figure 6.4.

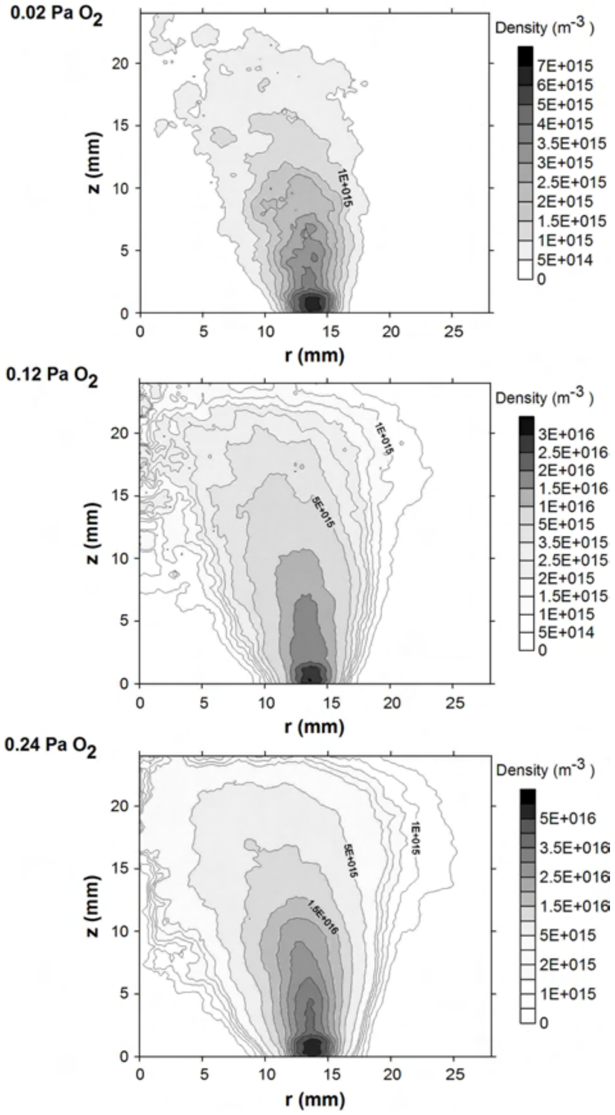

Figure 6.4: Calculated O_2^+ density profiles (in m^{-3}) at an Ar partial pressure of 1.0 Pa and O_2 partial pressures of 0.02, 0.12 and 0.24 Pa. Note that the y-axis (r=0) corresponds to the symmetry axis of the cylindrically symmetrical reactor.

The total positive ion density profile causes the sheath to be thinnest where the density is at maximum, i.e. at a radial position of 13.5 mm, as a consequence of a smaller Debye length at a higher ion density. This is clear from the plasma potential distribution presented in figure 6.5: the plasma potential well is steeper and the sheath is thinner at $r = 13.5$ mm. Moreover, due to the charged particles and the externally applied potential, a typical plasma potential distribution is created, as shown in figure 6.5: a steep ascend from cathode to bulk over the sheath area is observed, becoming flat and positive in the bulk.

When no O_2 gas is present, the negative space charge is only created by electrons, which are confined to the magnetic field in an area close to the cathode. As a result, the positive area of the electrical potential is only found in a narrow area close to the grounded reactor walls, as is clear from figure 6.5 (top figure).

When O_2 is added to the Ar gas, negative O^- ions are created by the electron impact reactions (11) and (12) from table 6.1, which is not the case in the Ar/N_2 discharge. Because the electrons are confined by the magnetic field in an area close to the cathode, the O^- ions are also created in this area. However, taking into account that heavy O^- ions are not trapped in the magnetic field in contrast to electrons, the plasma potential distribution (figure 6.5) forces the negative O^- ions to move towards the positive potential area. Figure 6.6 presents the calculated O^- density, which has a maximum at the positive potential area. This negative ion density causes the positive potential area to enlarge, see figure 6.5 (compare “without O_2” with “0.02 Pa O_2”).

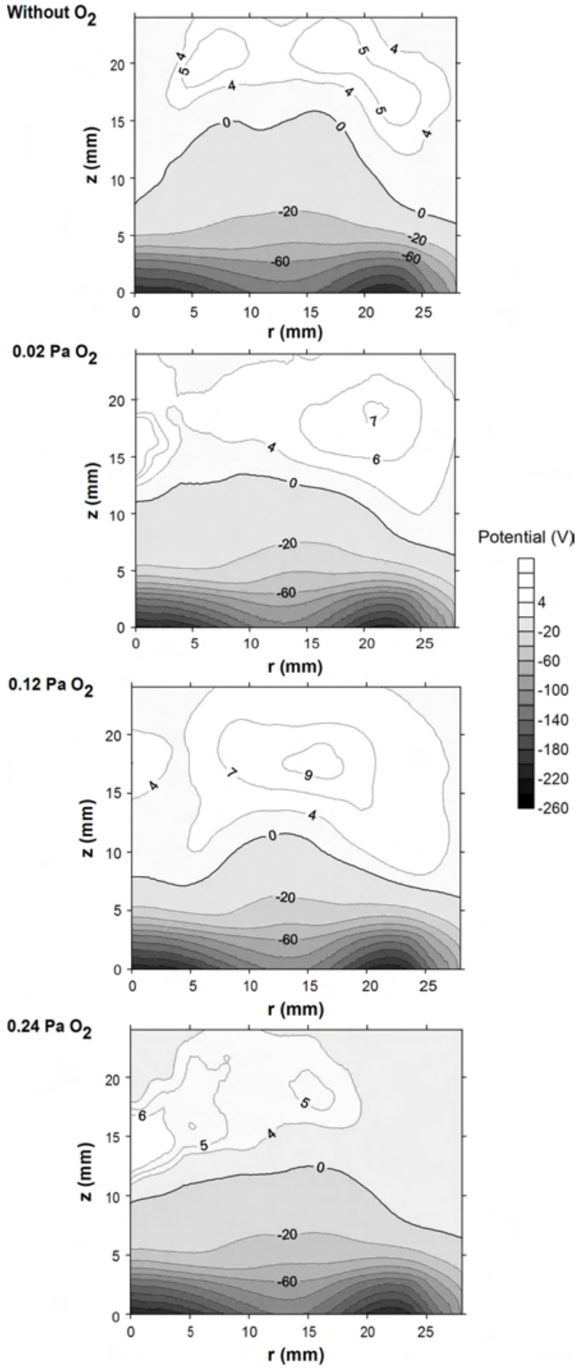

Figure 6.5: Calculated plasma potential distribution at an Ar partial pressure of 1.0 Pa, without O_2 and at O_2 partial pressures of 0.02, 0.12 and 0.24 Pa. The line which separates the negative and positive potential area ($V = 0$) is marked thicker for clarity. Note that the y-axis (r=0) corresponds to the symmetry axis of the cylindrically symmetrical reactor.

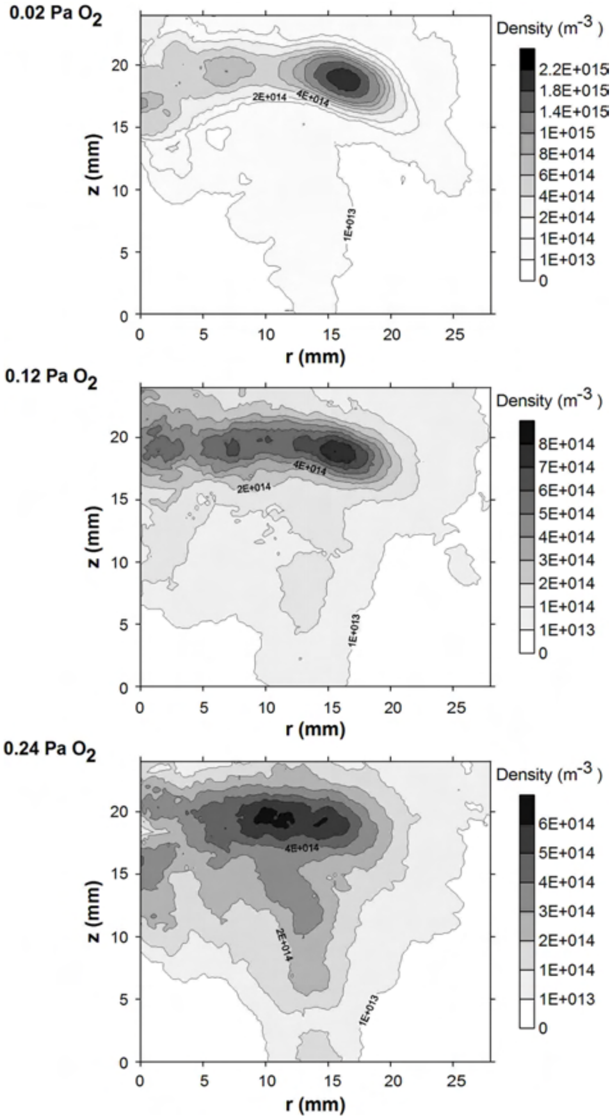

Figure 6.6: Calculated O^- density profiles (in m^{-3}) at an Ar partial pressure of 1.0 Pa and O_2 partial pressures of 0.02, 0.12 and 0.24 Pa. Note that the y-axis (r=0) corresponds to the symmetry axis of the cylindrically symmetrical reactor.

Figure 6.5 also illustrates that at increasing O_2 pressure, the positive potential area moves towards the symmetry axis of the magnetron discharge. This is true for the O^- density as well (see figure 6.6), which also becomes more spread out. Moreover, the O^- density exhibits a decreasing trend for higher O_2 pressure. This is a bit unexpected, but it is a consequence of the O^+ and

O_2^+ densities, which rise significantly when the O_2 pressure is increased, as was clear from figure 6.4 above. Consequently, the recombination reactions (53), (54) and (55) from table 6.1 occur much more often, which are an important loss mechanism for O^- ions. Therefore, the O^- density decreases upon O_2 addition (see figure 6.6). When the density drops, the Debye length increases leading to a less pronounced O^- shielding of the anode potential. This results in a spreading of the density profile and a spreading of the positive potential area towards the center of the discharge.

6.6.3 Sputtered Ti and O fluxes

The plasma species can bombard the target surface and sputter Ti and O atoms. Positive Ar^+, Ti^+, O^+ and O_2^+ ions, and fast Ar_f atoms contribute to the sputtering of the poisoned TiO_x target. The sputtered Ti and O fluxes at different values of the O_2 partial pressure are presented in figure 6.7. The sputtered Ti flux in the case of a pure Ar discharge is not presented here. It is around 10 times higher than the obtained values in the O_2/Ar mixture as a consequence of the lower sputter yield when the target is poisoned. When comparing with an Ar/N_2 discharge (see figure 5.11), it is clear that the sputtered Ti fluxes in an Ar/O_2 discharge are somewhat lower for similar operating conditions. This is explained by the difference in Ti sputter yield. Indeed, the Ti sputter yield from a TiN_x target has dropped a factor of 6.4 compared to the sputter yield of a pure metallic target (see section 5.4), whereas the Ti sputter yield from a TiO_x target has decreased more, i.e. a factor of 8.8 (see section 6.4). Therefore, the sputtered Ti flux from a TiO_x target drops more than from a TiN_x target.

As a consequence of localized bombardment of plasma species to the target, the sputtered Ti and O fluxes exhibit a peak profile. This localized sputtering causes the typical eroded race track area in the target.

The sputtered Ti and O fluxes are approximately equal, although the sputter yield of O is two times higher than of Ti (see section 6.4). However, the threshold energy for sputtering Ti by Ar^+ ions is lower (the main sputter source in the discharge) than sputtering O by Ar^+ ions. As a consequence, these two opposite effects cancel each other out. On the other hand, as was seen in section 5.6.4, in the Ar/N_2 discharge, there was a distinct difference between the Ti and N sputter fluxes. The reason is that the difference between the Ti and N sputter yields is four, whereas the difference between the Ti and O sputter yields is only two.

Also, there is no dependence of the O_2 partial pressure on the amount of sputtering, since most sputtering is caused by Ar^+ ions, which flux is independent on the O_2 partial pressure. In the Ar/N_2 discharge, however, a slight dependence was noted. Since the sputter yield of N is larger than of O, perhaps this slight dependence is only visible when sputtering N.

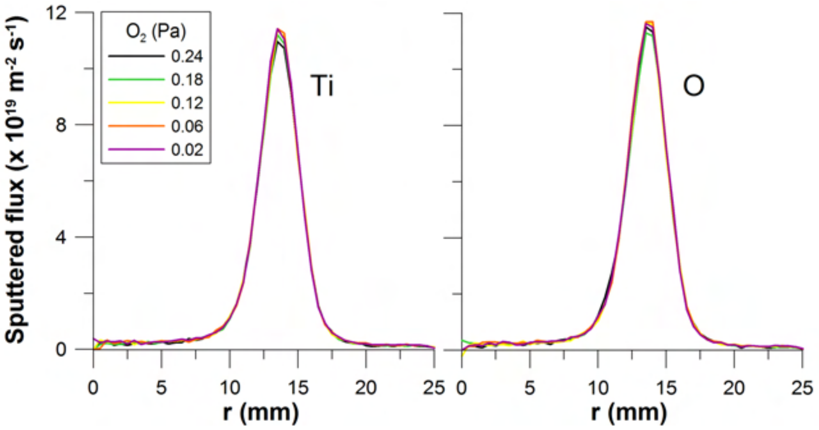

Figure 6.7: Calculated sputtered Ti and O fluxes from the cathode for different O_2 partial pressures as indicated in the legend, and at an Ar partial pressure of 1.0 Pa. Note that the y-axis (r=0) corresponds to the symmetry axis of the cylindrically symmetrical reactor.

6.6.4 Ti, O and O_2 fluxes to the substrate

The sputtered Ti and O atoms, together with the produced O atoms by plasma reactions, as well as the O_2 gas molecules, move through the plasma and can be deposited on a substrate, placed in front of the target. The calculated Ti, O and O_2 fluxes to the substrate are shown in figure 6.8. O^+, O_2^+, and O^- ions are also present close to the substrate (see figures 6.4 and 6.6). However, their flux to the substrate is several orders of magnitude lower than the O flux, causing these ions to have a negligible contribution to the deposition of the TiO_x film.

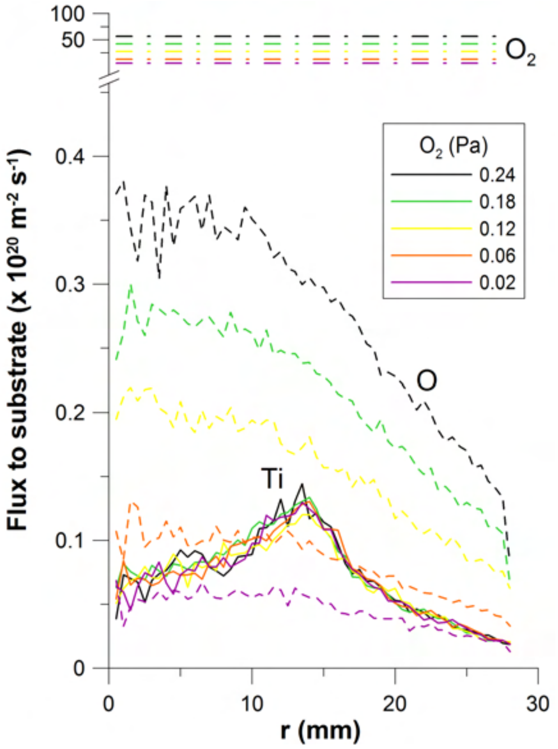

Figure 6.8: Calculated fluxes of the Ti, O and O_2 species to the substrate, as a function of radial position, for different O_2 partial pressures, at an Ar partial pressure of 1 Pa. Note that the y-axis (r=0) corresponds to the symmetry axis of the cylindrically symmetrical reactor.

Similar to the Ar/N_2 discharge, the Ti flux to the anode has a peak profile caused by the sputtered Ti peak profile (see figure 6.7), which is however broadened by diffusion. Moreover, the Ti flux to the anode remains virtually constant for increasing O_2 amount, in correspondance to the sputtered Ti flux (see section 6.6.3 and figure 6.7 above). The Ti fluxes to the substrate in the Ar/N_2 discharge were found to be somewhat higher (see figure 5.12), caused by the higher sputtered Ti fluxes, as was explained in section 6.6.3.

Similar to the Ar/N_2 discharge, more O atoms are created by plasma reactions than by sputtering. This causes the peak in the sputter profile to resolve in a typical diffusion profile. The O flux increases upon O_2 addition, which is a consequence of higher O production at higher O_2 amount.

At the gas pressures under consideration, gas heating is not so important [118]. As a result the Ar and O_2 gas densities remain constant and uniform (see also equation 2.86). Consequently, the O_2 flux bombarding the substrate has a uniform spatial profile. Logically, the O_2 flux increases for higher O_2 partial pressure (see also equation 2.87).

6.6.5 Deposition of a TiO_x film on the substrate

In analogy to the procedure followed in the Ar/N_2 chapter, the radial deposited fraction of TiO_2 (i.e. the compound fraction) on the substrate is calculated with equation 6.2, and it is shown in figure 6.9. Similar conclusions as in chapter 5 can be drawn: the compound fraction shows a drop, but flattens and becomes closer to unity at increasing O_2 partial pressure. When comparing the TiO_2 compound fraction to the TiN compound fraction (figure 5.13), it is noticeable that the TiO_2 compound fraction is lower than the TiN compound fraction. This is caused by the fact that two O atoms are needed for deposition of a TiO_2 compound, whereas only one N atom is aqcuired for the TiN compound (which was indeed included in equation 6.2).

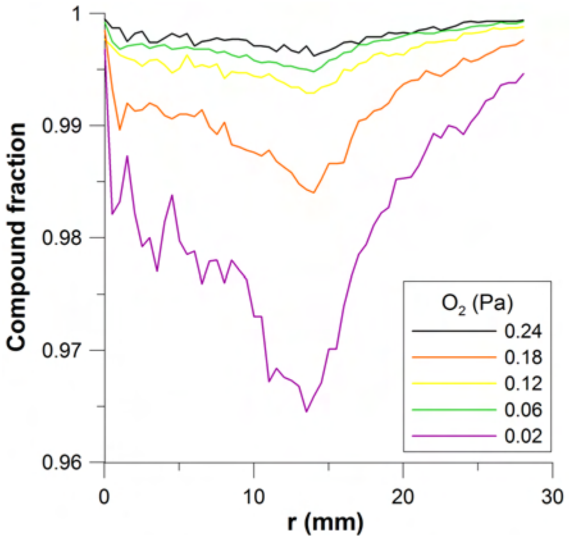

Figure 6.9: Calculated compound fraction on the substrate surface, as a function of radial position, for different O_2 partial pressures, at an Ar partial pressure of 1 Pa. Note that the y-axis (r=0) corresponds to the symmetry axis of the cylindrically symmetrical reactor.

Based on this radial compound fraction, the constant SC values of O and O_2 are adapted, according to equation 6.3. The calculated effective SC values (SC_{eff}) of O and O_2 are presented in figure 6.10.

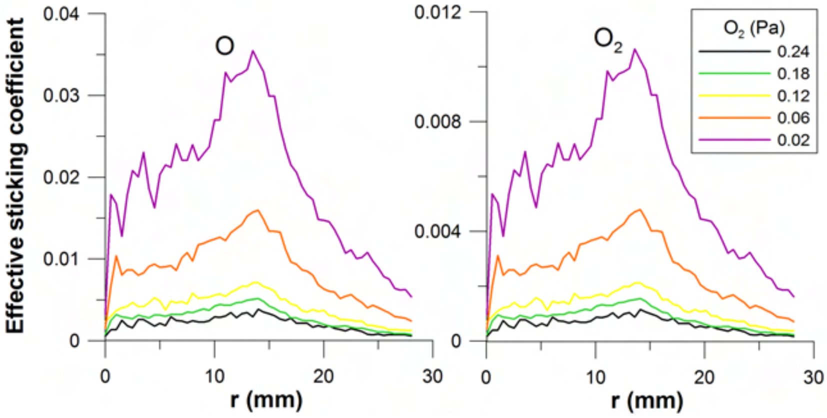

Figure 6.10: Calculated effective sticking coefficients of O and O_2, as a function of radial position, for different O_2 partial pressures, at an Ar partial pressure of 1 Pa. Note that the y-axis (r=0) corresponds to the symmetry axis of the cylindrically symmetrical reactor.

Similar to the Ar/N_2 discharge, the SC_{eff} values are not constant in the radial direction, and they decrease at increasing O_2 gas pressure. However, in comparison to the constant initial SC values of O and O_2, i.e. 1 and 0.3, the effective values have dropped about a factor of 25-250, whereas this drop was twice as high for the SC_{eff} values of N and N_2 (see section 5.6.6). This is caused by the lower compound fraction for TiO_2 at similar conditions.

The deposition rate of Ti and O can be found when multiplying the fluxes of Ti, O and O_2 (figure 6.8) by the corresponding SC_{eff} values. The total deposition rate of oxygen is the sum of the deposition rates due to O and O_2 (note that O_2 counts double, because one O_2 molecule gives rise to two deposited O atoms). Figure 6.11 shows that the total deposition rate of O is two times higher than the deposition rate of Ti, which is required to deposit a TiO_2 film. The calculated stoichiometries for three of the investigated O_2 partial pressures are also presented (figure 6.11: grey curves, right axis). At the lowest O_2 amount (0.02 Pa), the stoichiometry of two is almost achieved (with a minimum value of 1.93). At increasing O_2 amount, the deposition rates of both Ti and O are hardly affected, but nevertheless, the small effect results in a stoichiometry becoming equal to two. The latter could also be predicted by the compound coverage, as was presented in figure 6.9, because the real stoichiometry of the film is found by multiplying the desired stoichiometry x=2 by the compound coverage (note that the desired stoichiometry x=2 was imposed by equation 6.1). This means that an O_2/Ar proportion of 1/10 is already enough to deposit a stoichiometric film (with a minimum value of 1.98), with a satisfactory deposition rate. A stoichiometric TiO_2 film deposition at similar conditions was also observed in calculations with the analytical “Berg-model” (in terms of the compound fraction) [30], and in experiments [129, 130].

The peak profiles in figure 6.11 for the total deposition rates of Ti and O illustrate that the deposited TiO_x film will have a non-uniform thickness, under the investigated conditions, as was also found for the TiN_x film (see section 5.6.6 and figure 5.15). This is caused by the non-uniform Ti flux (figure 6.8) leading to radially dependent SC_{eff} values (figure 6.10). However, as was mentioned in the previous chapter, it is expected that a more uniform film can be deposited by placing the substrate further from the target so that the fluxes to the substrate are smoothed out.

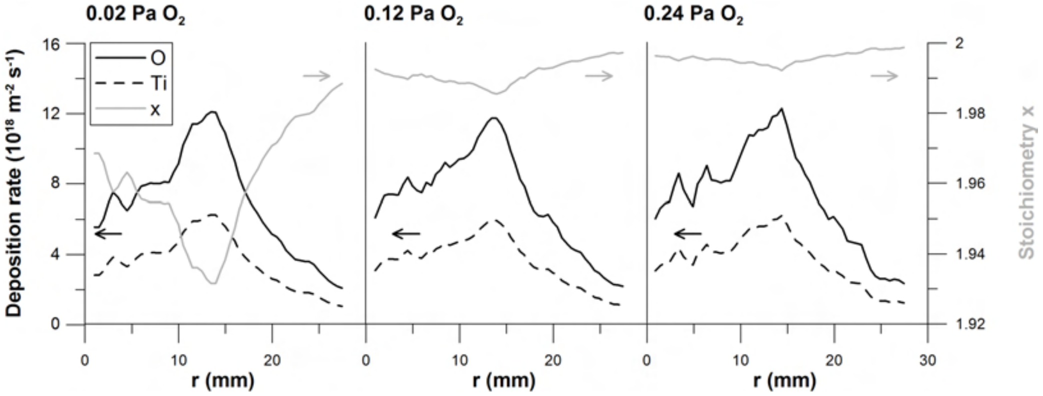

Figure 6.11: Calculated deposition rates of Ti and total O (black curves, left axis) as a function of radial position at an Ar partial pressure of 1 Pa and O_2 partial pressures of 0.02, 0.12 and 0.24 Pa. Also shown is the calculated stoichiometry x of the deposited TiO_x films (grey curves, right axis). Note that the y-axis (r=0) corresponds to the symmetry axis of the cylindrically symmetrical reactor.

Similar to the Ar/N_2 discharge, it was also found that O_2 contributes at least 50 times more than O to the total deposition of oxygen in the TiO_x film. This is caused by the much higher O_2 flux compared to the O flux (see figure 6.8 above), although the SC_{eff} of O_2 is lower than that of O (see figure 6.10 above).

6.7 Conclusion

A 2d3v particle-in-cell/Monte Carlo collisions model was developed to investigate the physical processes in a magnetron discharge during the reactive sputter deposition of TiO_x films. The plasma species taken into account are electrons, Ar^+ ions, fast Ar_f atoms, metastable Ar_m^* atoms, Ti^+ ions, Ti atoms, O^+ ions, O_2^+ ions, O^- ions, and O atoms. This model includes target sputtering, secondary electron emission, electron reflection, atom sticking, and the effects of a poisoned target (on sputter yield and $SEEC$ value). To investigate the deposition process of the TiO_x film, an analytical surface model was coupled to the PIC/MCC model. With this combined model, the cathode current and voltage, the plasma potential and electric field distribution, as well as the density profiles and fluxes of the different plasma species are calculated. Also, the stoichiometry x of the TiO_x film and its deposition rate can be obtained in a self-consistent manner.

The plasma characteristics were calculated at different O_2/Ar gas proportions. Note that at the lowest O_2/Ar gas proportion, the target is already completely poisoned. It was shown that at constant Ar partial pressure, higher O_2 pressures cause higher O^+ and O_2^+ densities. This leads to more recombination reactions of these ions with the negative O^- ions, causing the O^- density to become smaller, and more spread out. This also results in a more spread out positive plasma potential towards the center of the reactor.

The deposition of the TiO_x film was investigated, and it was calculated that at the O_2/Ar gas proportions under study, the stoichiometry of x=2 is almost achieved. When increasing the O_2/Ar gas proportion, the stoichiometry rises to x=2, whereas the deposition rates of both Ti and O are hardly affected. The deposited O in the TiO_x film originates almost entirely from the O_2 gas: O_2 molecules contribute at least 50 times more to the total oxygen deposition than O atoms.

Summary

Over the last decades, magnetron discharges have gained industrial importance as a tool for coating materials with a thin metallic or compound film. The coating process in magnetron discharges is referred to as "(reactive) sputter deposition". In this process, a metallic target material is sputtered, and the sputtered metal atoms are deposited (with or without other reactive species) on a substrate. As such, this protective layer enhances the substrate material in a mechanical, electrical or optical way.

To deposit a metallic film, a metallic target, in our case titanium, is sputtered by energetic species (mainly ions, but also fast atoms). These species can be created by generating an electric field between two electrodes placed in a gas, for example argon. The electric field breaks down the gas into electrons, ions, and (fast) atoms, and hence a plasma or discharge is created. In a magnetron discharge, apart from the electric field, also a magnetic field is present, to use the electrons more efficiently. Indeed, due to their small mass, their Larmor radius is small, causing them to be trapped in the magnetic field. As a consequence of their longer mean free path during their circulations around the magnetic field lines, more ionizations occur, and hence more sputtering. The sputtered Ti atoms diffuse through the plasma and can be deposited on a substrate, in a process called "sputter deposition".

To deposit a compound film, on the other hand, a reactive gas is added to the Ar background gas. Gas molecules as well as atoms from the gas can react with the Ti species on the substrate to form a compound film. However,

a compound film can also be formed on the target surface, which is called "target poisoning", and which drastically reduces the sputter yield. In this thesis, the addition of N_2 and O_2 to the Ar gas was studied, to deposit a TiN_x or a TiO_x film, respectively, in a process called "reactive sputter deposition".

Since the physics of a magnetron discharge and the processes concerning the sputter deposition process are both so complex and elaborate, a profound study is necessary to understand the magnetron discharge, and to improve the sputter deposition applications. A lot of experimental and numerical studies exist, focussing on either the plasma properties, or the sputter deposition process, and the properties of the deposited thin film. However, not many studies cover the whole picture of magnetron sputter deposition in detail.

In this work, numerical simulations were carried out to study the plasma behavior and sputter deposition process in a direct current (DC) magnetron discharge. More precisely, a 2d3v particle-in-cell/Monte Carlo collisions (PIC/MCC) model was applied, which includes plasma-surface interactions, such as target sputtering, secondary electron emission (characterised by the secondary electron emission coefficient, $SEEC$), species reflection and adsorption (characterised by the sticking coefficient, SC).

A first goal of this PhD thesis was the study of the plasma properties of a magnetron discharge in pure Ar gas. The focus lies on the importance of including an external electrical circuit (coupled to the cathode, and needed to generate the plasma) to the PIC/MCC description of a DC magnetron discharge. It is shown that an external circuit limits the calculated current to the desired regime: the normal and abnormal regime were studied. The importance of including a current limiting device was shown by comparing a code with external circuit included with a code in which the external circuit was omitted: the calculated currents in the latter case diverge to infinity or converge to an incorrect value, whereas the calculated currents in the code with external circuit are comparable with experiments. *We can conclude that the external electrical circuit is inevitable in a PIC/MCC code for an* *accurate and correct description of magnetron discharges.*

A second study described in this PhD thesis handles the effect of the magnetic field strength in a pure Ar discharge on the plasma species distributions, especially in the sheath area in front of the cathode. Also, the effects of the sheath behavior on the sputter deposition process are investigated. The sheath area is the most important area for sputtering: the ions are accelerated here, gaining enough energy to sputter the Ti target. The sheath behavior at different magnetic field strengths was studied: the calculated plasma potential and ion densities demonstrate that at low magnetic field, the sheath width decreases with increasing magnetic field strength, whereas the opposite trend was noticed at strong magnetic fields. This was explained by the calculated electron densities in the sheath: the electrons are trapped in the strong magnetic field which limits their mobility, preventing a pronounced plasma potential build up. Hence, a more spread out positive space charge is created, and consequently, the sheath is wider. The sheath behavior also affects the sputter deposition process. At weak magnetic fields, the sputtered Ti flux increases with rising magnetic field strength. At strong magnetic fields, the sputtered flux remains approximately constant, but the profile narrows, and the target is therefore less efficiently consumed. *Therefore, a proper choice of the magnetic field strength enables control of the sheath width and hence control of the erosion profile.*

A third aim of this thesis was the study of the reactive sputter deposition of TiN_x films. Apart from the plasma-surface interactions in a pure Ar discharge, the effects of a poisoned target are included, i.e. on the $SEEC$ and sputter yield. Moreover, an analytical surface model for the substrate is coupled to the PIC/MCC model to calculate effective sticking coefficients, SC_{eff}. Hence, the actual stoichiometry x and deposition rate of the TiN_x film at various N_2/Ar ratios can be predicted. With this combined model, we calculated the plasma characteristics, such as densities and fluxes of the various species in the whole reactor, and the influence of the N_2/Ar gas ratio. Moreover, the fluxes and contributions of various species bombarding the cathode target were calculated, emphasizing the importance of fast Ar_f atoms, after Ar^+ ions, for the sputtering process. Also, the effect of a poisoned target on the sputtered fluxes was illustrated, i.e. a drop in the sputtered Ti flux was noticed after transition from a metallic to a poisoned mode. Finally, it was shown that at higher N_2 pressure, the film has a more uniform stoichiometry, closer to one. The total deposition rate of nitrogen due to N_2 is much higher than the deposition rate due to N, i.e. N_2 contributes at least 50 times more to the total deposition rate of nitrogen in the film, than the N atoms.

The last topic in this PhD thesis examines the reactive sputter deposition of TiO_x films. The plasma characteristics were calculated at different O_2/Ar gas ratios, and we focussed on the effect of the present negative O^- ions. It was shown that at constant Ar partial pressure, higher O_2 pressures cause higher O^+ and O_2^+ densities. This leads to more recombination reactions of these ions with the negative O^- ions, causing the O^- density to become smaller, and more spread out. This also results in a more spread out positive plasma potential towards the center of the reactor. The deposition of TiO_x films was investigated, and it was predicted that at the O_2/Ar gas ratios under study, the stoichiometry of x=2 is almost achieved. Similar to the Ar/N_2 discharge, the deposited oxygen in the TiO_x film originates almost entirely from the O_2 gas: O_2 molecules contribute at least 50 times more to the total oxygen deposition than the O atoms.

In conclusion of the last two topics, the combined PIC/MCC-analytical surface model for the description of the reactive sputter deposition of TiN_x or TiO_x films is able to calculate in detail the plasma potential distribution, different species densities, target fluxes, sputter contribution, sputter fluxes, fluxes to the substrate, and to predict the stoichiometry x of deposited TiN_x or TiO_x films. *In summary, this model provides accurate information on the processes that occur in the plasma, as well as at the substrate surface.* It can be used as an extension or even validation for experiments and simple models, to come a step closer to a complete view on reactive magnetron sputter deposition.

In the future, this combined PIC/MCC-analytical surface model can be modified for other targets (e.g. Al, Mg) or target combinations (e.g. magnetron configurations with different Ti, Al, Mg, . . . targets), and/or different magnetron geometries (e.g. dual, cylindrical, rotating magnetrons). Also, different reactive gas combinations, e.g. Ar/N_2/O_2, can be used to deposit TiN_xO_y films. Furthermore, other electric (e.g. RF, pulsed DC, HIPIMS) or magnetic (e.g. unbalanced) configurations can be included in the model.

Samenvatting

De laatste decennia hebben magnetronontladingen aan industriëel belang gewonnen door hun toepassingen op het vlak van materiaaltechnologie. Hierbij worden materialen gecoat met een dunne film van een metaal of metaalverbinding. In magnetronontladingen wordt dit afzettingsproces "(reactieve) sputterdepositie" genoemd: een metalen targetmateriaal wordt gesputterd, en de gesputterde metaalatomen afgezet (met of zonder andere reactieve deeltjes) op een substraat. Deze beschermende laag verbetert de mechanische, electrische of optische eigenschappen van het substraatmateriaal.

Om een metaalfilm af te zetten wordt een metalen target, in ons geval titaan, gesputterd met energetische deeltjes (vooral ionen, maar ook snelle atomen). Deze deeltjes kunnen gegenereerd worden door een elektrisch veld aan te leggen tussen twee elektroden in een gas, bijvoorbeeld argon. Het elektrisch veld zorgt ervoor dat het gas opsplitst in elektronen, ionen, en (snelle) atomen: een plasma of ontlading komt tot stand. In een magnetronontlading is, naast het elektrisch veld, ook een magneetveld aanwezig, zodat de elektronen efficiënter gebruikt worden. Door hun lage massa is hun Larmor straal immers klein, wat ervoor zorgt dat ze vastgehouden worden in het magneetveld. Ten gevolge van hun langere vrije weglengte tijdens hun rotaties rond de magnetische veldlijnen, ionizeren ze meer neutralen, waardoor meer sputtering kan optreden. De gesputterde Ti-atomen diffunderen doorheen het plasma en kunnen afgezet worden op een substraat. Dit proces wordt "sputterdepositie" genoemd.

Om een metaalverbinding af te zetten wordt een reactief gas toegevoegd aan het Ar-achtergrondgas. Zowel gasmoleculen als atomen afkomstig van het gas kunnen reageren met Ti-atomen op het substraat, met de vorming van een metaalverbinding op het substraat tot gevolg. Deze metaalverbinding kan echter ook gevormd worden op het targetoppervlak, wat "target poisoning" of "targetvergiftiging" genoemd wordt, en waardoor o.a. de sputteropbrengst drastisch verlaagt. In dit proefschrift wordt de toevoeging van N_2 en O_2 aan het Ar-gas bestudeerd, om respectievelijk een TiN_x- of een TiO_x-film af te zetten. Dit proces wordt "reactieve sputterdepositie" genoemd.

Aangezien zowel de fysica van een magnetronontlading als het sputterdepositieproces zo complex en uitgebreid zijn, is een grondig onderzoek noodzakelijk om de magnetronontlading te begrijpen en de toepassingen van sputterdepositie te optimaliseren. Er bestaan reeds veel experimentele en numerieke studies, die zich ofwel concentreren op de plasma eigenschappen, ofwel op het sputterdepositieproces. Slechts weinig studies geven een volledige beschrijving van magnetronsputterdepositie in detail.

In dit werk werden numerieke simulaties uitgevoerd om het plasmagedrag en het sputterdepostieproces te bestuderen in een gelijkstroom magnetronontlading. Hiervoor werd een 2d3v particle-in-cell/Monte Carlo collisions (PIC/ MCC) model aangewend, dat ook de plasma-oppervlakte-interacties in rekening brengt, zoals targetsputtering, secundaire elektronemissie (gekarakteriseerd door de secundaire elektronemissiecoëfficiënt, $SEEC$), deeltjesreflectie en -adsorptie (gekarakteriseerd door de stickingscoëfficiënt, SC).

Een eerste doelstelling van deze thesis was de studie van de plasma eigenschappen van een magnetronontlading in puur Ar-gas. De nadruk ligt op het belang van een extern elektrisch circuit (dat gekoppeld wordt aan de kathode, nodig voor het genereren van een ontlading) aan een PIC/MCC-model van een gelijkstroom magnetronontlading. Er werd aangetoond dat een extern circuit de berekende stroom limiteert tot het gewenste regime: het normale en abnormale regime werden bestudeerd. Het belang van een stroom-limiterende component werd gedemonstreerd door een code met extern circuit te vergelijken met een code waarin het extern circuit werd weggelaten: de berekende stromen in het laatste geval divergeren naar oneindig, hoewel de berekende stromen in de code met extern circuit vergelijkbaar zijn met experimentele waarden. *We kunnen besluiten dat het extern elektrisch circuit noodzakelijk is in een PIC/MCC-code voor een accurate en correcte beschrijving van magnetronontladingen.*

Een tweede studie in dit proefschrift behandelt het effect van de sterkte van het magneetveld in een pure Ar-ontlading op de plasmadeeltjesverdelingen, vooral in de sheathzone voor de kathode. De effecten van het sheathgedrag op het sputterdepositieproces werden eveneens bestudeerd. De sheathzone is het belangrijkste gebied voor sputtering: de ionen worden daar versneld, zodat ze voldoende energie winnen om het Ti-target te sputteren. Het gedrag van de sheath bij een verschillende sterkte van het magneetveld werd bestudeerd: de berekende plasmapotentiaal en ionendichtheden demonstreren dat bij een zwak magneetveld de sheathbreedte daalt wanneer de sterkte van het magneetveld verhoogd wordt, hoewel de omgekeerde trend werd waargenomen bij sterke magneetvelden. Dit werd verduidelijkt door de berekende elektronendichtheden in de sheath: de elektronen worden vastgehouden in het sterke magneetveld, wat hun mobiliteit belemmert en daardoor een uitgesproken opbouw van de plasmapotentiaal verhindert. Hierdoor komt een meer uitgebreide positieve ruimtelading tot stand, met een bredere sheath tot gevolg. Het sheathgedrag beïnvloedt ook het sputterdepositieproces. Bij zwakke magneetvelden stijgt de gesputterde Ti-flux met stijgende magneetveldsterkte. Bij sterke magneetvelden blijft de gesputterde Ti-flux ongeveer constant, maar het profiel versmalt, waardoor het target minder efficiënt verbruikt wordt. *Als conclusie stellen we dat door een geschikte keuze van het magneetveld de breedte van de sheath en daardoor ook het erosieprofiel geregeld kan worden.*

Een derde doel van dit proefschrift was de studie van de reactieve sputterdepositie van TiN_x films. Naast de plasma-oppervlakte-interacties in een pure Ar-ontlading, werden de gevolgen van een vergiftigd target in rekening gebracht, d.i. op de $SEEC$ en de sputteropbrengst. Bovendien werd een analytisch oppervlatkemodel voor het substraat gekoppeld aan het PIC/MCC-model om effectieve stickingscoefficiënten, SC_{eff}. Hiermee kan de echte stoichiometrie x en de depositiesnelheid van de TiN_x-film bij verschillende N_2/Ar-verhoudingen voorspeld worden. Met dit gecombineerd model werden de plasma eigenschappen berekend, zoals dichtheden en fluxen van de verschillende deeltjes in de reactor, en de invloed van de N_2/Ar-gasverhouding. Bovendien werden de fluxen en bijdragen van de verschillende deeltjes die de kathode bombarderen, berekend. Hier werd het belang van snelle Ar_f-atomen benadrukt, na Ar^+-ionen, voor het sputterproces. Het effect van een vergiftigd target op de gesputterde Ti-flux werd geïllustreerd, d.i. er werd een daling van de gesputterde Ti-flux vastgesteld na de overgang van een metalen naar een vergiftigd target. Tenslotte werd gevonden dat bij een hogere N_2-druk de film een meer uniforme stoichiometrie heeft, die dichter ligt bij één. De totale depositiesnelheid van stikstof door N_2-moleculen is veel hoger dan de depositiesnelheid door N-atomen, d.i. N_2 draagt minstens 50 keer meer bij tot de totale depositiesnelheid van stikstof in de film, dan N-atomen.

Het laatste onderwerp in dit proefschrift bestudeert de reactieve sputterdepositie van TiO_x-films. De plasma-eigenschappen werden berekend bij verschillende O_2/Ar-gasverhoudingen, en we legden de nadruk op het effect van de aanwezige negatieve O^--ionen. Er werd aangetoond dat bij een constante Ar-partiëeldruk hogere O^+- en O_2^+-dichtheden veroorzaken. Dit leidt tot meer recombinatiereacties van deze ionen met de negatieve O^--ionen, wat een verlaagde en meer uitgespreide O^--dichtheid veroorzaakt worden door hogere O_2-drukken. Dit resulteert eveneens in een meer uitgespreide positieve plasmapotentiaal naar het midden van de reactor toe. Ook de depositie van TiO_x-films werd bestudeerd, en er werd voorspeld dat een stoichiometrie van x=2 nagenoeg bereikt werd bij de gebruikte O_2/Ar-gasverhoudingen. Vergelijkbaar met de Ar/N_2-ontlading werd gevonden dat de afgezette zuurstof in de TiO_x-film bijna volledig te wijten is aan het O_2-gas: O_2-moleculen dragen minstens 50 keer meer bij tot de totale zuurstof afzetting in de film dan O-atomen.

Ter conclusie van de laatste twee onderwerpen stellen we dat het gecombineerd PIC/MCC-analytisch oppervlaktemodel dat de reactieve sputterdepositie van TiN_x- of TiO_x-films beschrijft, het mogelijk maakt om in detail de plasmapotentiaalverdeling, verscheidene deeltjesdichtheden, targetfluxen, sputterbijdragen, sputterfluxen en fluxen naar het substraat te berekenen, en om de stoichiometrie x van afgezette TiN_x- of TiO_x-films te voorspellen. *Samengevat is dit model in staat om accurate informatie te verschaffen zowel over de processen die voorkomen in het plasma, als aan het substraatoppervlak.* Dit model kan gebruikt worden als een uitbreiding of zelfs validatie van experimenten en eenvoudige modellen, om zo een stap dichter te komen bij een volledig beeld van reactieve magnetronsputterdepositie.

In de toekomst kan dit gecombineerd PIC/MCC-analytisch oppervlaktemodel aangepast worden naar andere targetmaterialen (b.v. Al, Mg) of targetcombinaties (b.v. magnetronconfiguraties met verschillende Ti, Al, Mg, . . . targets), en/of andere magnetrongeometrieën (b.v. dual, cylindrische, roterende magnetrons). Bovendien kunnen verschillende reactieve gascombinaties, b.v. Ar/N_2/O_2, gebruikt worden om b.v. TiN_xO_y-films af te zetten. Verder kunnen andere elektrische (b.v. RF, gepulste DC, HIPIMS) of magnetische (b.v. ongebalanceerde) configuraties gebruikt worden in het model.

List of publications

1. Van der Linden V, Bultinck E, Deruytter J, Schalm O, Janssens K, and Devos W. Compositional analysis of 17-18th century archaeological glass fragments, excavated in Mechelen, Belgium: comparison with data from neighboring cities in the Low Countries. *Nucl. Instrum. Methods Phys. Res. B*, 239 (1-2):100-106, 2005.

2. Vande Velde C, Bultinck E, Tersago K, van Alsenoy C, and Blockhuys F. From anisole to 1,2,4,5-tetramethoxybenzene: theoretical study of the factors that determine the conformation of methoxy groups on a benzene ring. *Int. J. Quantum Chem.*, 107(3):670, 2007.

3. Bultinck E, Kolev I, Bogaerts A, and Depla D. The importance of an external circuit in a particle-in-cell/Monte Carlo collisions model for a direct current planar magnetron. *J. Appl. Phys.*, 103:013309, 2007.

4. Bultinck E and Bogaerts A. The effect of the magnetic field strength on the sheath region of a dc magnetron discharge. *J. Phys. D: Appl. Phys.*, 41:202007, 2008.

5. Bultinck E, Mahieu S, Depla D, and Bogaerts A. The reactive sputter deposition of a TiN film, simulated with a particle-in-cell/Monte Carlo collisions model. *New J. Phys.*, 11:023039, 2009.

6. Bogaerts A, Bultinck E, Eckert M, Georgieva V, Mao M, Neyts E, Schwaederl L. Computer modeling of plasmas and plasma-surface interactions. *Plasma Process. Polym.*, 6:295, 2009.

7. Bogaerts A, Bultinck E, Kolev I, Schwaederl L, Van Aeken K, Buyle G, and Depla D. Computer modeling of magnetron discharges. *J. Phys. D: Appl. Phys.*, accepted for publication.

8. Bultinck E, Mahieu S, Depla D, and Bogaerts A. Particle-in-cell/Monte Carlo collisions model for the reactive sputter deposition of nitride layers. *Plasma Process. Polym.*, accepted for publication.

9. Bultinck E and Bogaerts A. Particle-in-cell/Monte Carlo collisions treatment of an Ar/O_2 magnetron discharge used for the reactive sputter deposition of TiO_x films. *New J. Phys.*, submitted for publication.

Interactive communication

1. Bultinck E, Kolev I, and Bogaerts A. The consequences of neglecting an external circuit in a 2d3v particle-in-cell/Monte Carlo collisions model for a direct current planar magnetron. *Poster presentation at the Joint General Scientific Meeting 2007 of the Belgian Physical Society and the Belgian Biophysical Society (BPS)*, Antwerp, Belgium, May 30, 2007.
2. Bultinck E, Kolev I, and Bogaerts A. The consequences of neglecting an external circuit in a 2d3v Particle-In-Cell/Monte Carlo Collisions model for a direct current planar magnetron. *Poster presentation at the 28th International Conference on Phenomena in Ionized Gases (ICPIG)*, Prague, Czech Republic, June 15-20, 2007.
3. Bogaerts A, Bultinck E, Kolev I, and Gaillard M. Introduction to magnetron sputtering: basic physical processes and mechanisms. *Invited oral presentation at the 12th European Summer School Low Temperature Plasma Physics: Master Class "Physical Vapor Deposition"*, Bad Honnef, Germany, October 6-13, 2007.
4. Bultinck E and Bogaerts A. Computersimulaties van een magnetron ontlading voor de reactieve sputter-depositie van nitridelagen. *Oral presentation at the Vlaams Jongerencongres van de Chemie 9 (VJC9)*, Antwerp, Belgium, April 4, 2008.
5. Bultinck E, Mahieu S, Depla D, and Bogaerts A. Particle-in-cell/Monte Carlo collisions model for the reactive sputter-deposition of nitride layers. *Poster presentation at the 19th Europhysics Conference on*

the Atomic and Molecular Physics of Ionized Gases (ESCAMPIG), Granada, Spain, July 15-19, 2008.

6. Bultinck E, Mahieu S, Depla D, and Bogaerts A. Particle-in-cell/Monte Carlo collisions model for the reactive sputter-deposition of nitride layers. *Oral presentation at the 11th International Conference on Plasma Surface Engineering (PSE)*, Garmisch-Partenkirchen, Germany, September 15-19, 2008.

7. Bultinck E. Particle-in-cell/Monte Carlo collisions model (PIC/MCC). *Invited talk at the Department of Solid States Physics, Ghent University*, Belgium, October 22, 2008.

8. Bogaerts A, Bultinck E, Mao M, Neyts E, and Schwaederle L. Computer simulations of processing plasmas. *Invited oral presentation at the 2008 American Vacuum Society (AVS) Conference - Plasma Science and Technology Division*, Boston, USA, October 19-24, 2008.

9. Bultinck E, Mahieu S, Depla D, and Bogaerts A. Reactive sputter deposition of TiN_x layers, simulated with a particle-in-cell/Monte Carlo collisions model. *Oral presentation at the 14th International Conference on Thin Films & Reactive Sputter Deposition (ICTF14)*, Ghent, Belgium, November 17-20, 2008.

10. Bultinck E, and Bogaerts A. Reactive sputter deposition of TiO_x films in a magnetron discharge, described with a particle-in-cell/Monte Carlo collisions model. *Poster presentation at the 29th International Conference on Phenomena in Ionized Gases (ICPIG)*, Cancun, Mexico, July 12-17, 2009.

11. Bultinck E, and Bogaerts A. Particle-in-cell/Monte Carlo collisions treatment of a magnetron discharge used for the reactive sputter deposition of TiO_x films. *Abstract submitted for the Asian-European International Conference on Plasma Surface Engineering (AEPSE)*, Busan, Korea, September 20-25, 2009.

Bibliography

[1] Waits R K. Planar magnetron sputtering. *Journal of Vacuum Science and Technology*, 15(2):179, 1978.

[2] Buyle G. *Simplified model for the DC Planar Magnetron Discharge.* PhD thesis, Ghent University, 2005.

[3] Depla D and Mahieu S. *Reactive Sputter Deposition.* Springer-Verlag Berlin Heidelberg, 2008.

[4] Bradley J W, Thompson S, and Gonzalvo Y A. Measurement of the plasma potential in a magnetron discharge and the prediction of the electron drift speeds. *Plasma Sources Sci. Technol.*, 10(3):490, 2001.

[5] Li X Y, Depla D, Leroy W, Haemers J, and De Gryse R. Influence of deposition on the reactive sputter behaviour during rotating cylindrical magnetron sputtering. *J. Phys. D: Appl. Phys.*, 41:035203, 2008.

[6] Van Aeken K, Mahieu S, and Depla D. The metal flux from a rotating cylindrical magnetron : a Monte Carlo simulation. *J. Phys. D: Appl. Phys.*, 41(15):205307, 2008.

[7] Oloya J J, Rodil S E, and Muhl S. Comparative study of niobium nitride coatings deposited by unbalanced and balanced magnetron sputtering. *Thin Solid Films*, 516:8319, 2008.

[8] Mahieu S, Ghekiere P, De Winter G, De Gryse R, Depla D, Van Tendeloo G, and Lebedev O I. Biaxially aligned titanium nitride thin films

deposited by reactive unbalanced magnetron sputtering. *Surf. Coat. Technol.*, 200:2764, 2006.

[9] Ghekiere P, Mahieu S, De Winter G, De Gryse R, and Depla D. Scanning electron microscopy study of the growth mechanism of biaxially aligned magnesium oxide layers grown by unbalanced magnetron sputtering. *Thin Solid Films*, 493:129, 2005.

[10] Duquenne C, Tessier P Y, Besland M P, Angleraud B, Jouan P Y, Aubry R, Delage S, and Djouadi M A. Impact of magnetron configuration on plasma and film properties of sputtered aluminum nitride thin films. *J. Appl. Phys.*, 104:063301, 2008.

[11] Inoue S, Saeki T, Uchida H, Koterazawa K, and Iwasa M. Effects of ion flux on the properties of dc magnetron-sputtered stainless steel films. *Vacuum*, 66:257, 2002.

[12] Guo Q X, Yoshitugu M, Tanaka T, Nishio M, and Ogawa H. Microscopic investigations of aluminum nitride thin films grown by low-temperature reactive sputtering. *Thin Solid Films*, 483(1-2):16, 2005.

[13] Figueroa U, Salas O, and Oseguera J. Production of AlN films: ion nitriding versus PVD coating. *Thin Solid Films*, 469-470:295, 2004.

[14] Mahmood A, Machorro R, Muhl S, Heiras J, Castillon F F, Farias M H, and Andrade E. Optical and surface analysis of dc-reactive sputtered AlN films. *Diamond and Related Materials*, 12(8):1315, 2003.

[15] Fu Y, Du H, and Zhang S. Functionally graded $TiN/TiNi$ shape memory alloy films. *Materials Letters*, 57(20):2995, 2003.

[16] de Pinho Alves Neto J, Giacomelli C, Klein A N, Muzart J L R, and Spinelli A. Electrochemical stability of magnetron-sputtered ti films on sintered and sintered/plasma nitrided Fe-1.5% Mo alloy. *Surf. Coat. Technol.*, 191(2-3):206, 2005.

[17] Alsaran A, Celik A, and Karakan M. Structural, mechanical and tribological properties of duplex-treated AISI 5140 steel. *Materials Characterization*, 54(4):85, 2005.

[18] Szikora B. Background of the titanium nitride deposition. *Vacuum*, 50(3-4):273, 1998.

[19] Safi I. A novel reactive magnetron sputtering technique for producing insulating oxides of metal alloys and other compound thin films. *Surf. Coat. Technol.*, 135(1):48, 2000.

[20] Koski K, Holsa J, Juliet P, Wang Z H, Aimo R, and Pischow K. Characterisation of aluminium oxide thin films deposited on polycarbonate substrates by reactive magnetron sputtering. *Materials Science and Engineering B*, 65(2):94, 1999.

[21] Depla D and De Gryse R. Influence of oxygen addition on the target voltage during reactive sputtering of aluminium. *Plasma Sources Sci. Technol.*, 10:547, 2001.

[22] Möller W and Güttler D. Modelling of plasma-target interaction during reactive magnetron sputtering of TiN. *J. Appl. Phys.*, 102:094501, 2007.

[23] Depla D, Tomaszewski H, Buyle G, and De Gryse R. Influence of the target composition on the discharge voltage during magnetron sputtering. *Surf. Coat. Technol.*, 201:848, 2006.

[24] Pekker L and Krasheninnikov S I. On the theory of low-pressure magnetron glow discharge. *Physics of Plasmas*, 7(1):382, 2000.

[25] Lan Gu and Lieberman M A. Axial distribution of optical emission in a planar magnetron discharge. *J. Vac. Sci. Technol. A.*, 6(5):2960, 1988.

[26] Bradley J W, Arnell R D, and Armour D G. Measurement and modelling of the bulk plasma in magnetron sputtering sources. *Surf. Coat. Technol.*, 97(1-3):538, 1997.

[27] Bradley J W, Thompson S, and Gonzalvo Y A. Measurement of the plasma potential in a magnetron discharge and the prediction of the electron drift speeds. *J. Phys. D: Appl. Phys.*, 34(22):3241, 2001.

[28] Wendt A E and Lieberman M A. Spatial structure of a planar magnetron discharge. *J. Vac. Sci. Technol. A.*, 8(2):902, 1990.

[29] Buyle G, Depla D, Eufinger K, Haemers J, De Bosscher W, and De Gryse G. Simplified model for the dc planar magnetron discharge. *Vacuum*, 74:353, 2004.

[30] Berg S and Nyberg T. Fundamental understanding and modeling of reactive sputtering processes. *Thin Solid Films*, 476(2):215, 2005.

[31] Depla D, Heirwegh S, Mahieu S, and De Gryse R. Towards a more complete model for reactive magnetron sputtering. *J. Phys. D: Appl. Phys.*, 40:1957, 2007.

[32] Kolev I and Bogaerts A. Numerical models of the planar magnetron glow discharges. *Contrib. Plasm. Phys*, 44(7-8):582, 2004.

[33] Bradley J W. The plamsa properties adjacant to the target in a magnetron sputtering source. *Plasma Sources Sci. Technol.*, 5(1):622, 1996.

[34] Costin C, Marques L, Popa G, and Gousset G. Two-dimensional fluid approach to the dc magnetron discharge. *Plasma Sources Sci. Technol.*, 14(1):168, 2005.

[35] Bogaerts A, Van Straaten M, and Gijbels R. Description of the thermalisation process of the sputtered atoms in a glow discharge using a three-dimensional Monte Carlo method. *J. Appl. Phys.*, 77(1):1868, 1995.

[36] Birdsall C K and Langdon A B. *Plasma Physics via Computer Simulations.* Bristol: IOP publishing, 1991.

[37] Kolev I, Bogaerts A, and Gijbels R. Influence of electron recapture by the cathode upon the discharge characteristics in dc planar magnetrons. *Phys. Rev. E*, 72(5):056402, 2005.

[38] Kolev I and Bogaerts A. Detailed numerical investigation of a dc sputter magnetron. *IEEE Trans. on Plasma Science*, 34(3):886, 2006.

[39] Kolev I and Bogaerts A. PIC/MCC numerical simulation of a dc planar magnetron. *Plasma Process. Polym.*, 3:127, 2006.

[40] Pflug A, Szyszka B, and Niemann J. Simulation of reactive sputtering kinetics in real in-line processing chambers. *Thin Solid Films*, 442(1-2):21, 2003.

[41] Nanbu K, Segawa S, and Kondo S. Self-consistent particle simulation of three-dimensional dc magnetron discharge. *Vacuum*, 47(6-8):1013, 1996.

[42] van der Straaten T A, Cramer N F, Falconer I S, and James B W. The cylindrical dc magnetron discharge: I. particle-in-cell simulation. *J. Phys. D: Appl. Phys.*, 31:177, 1998.

[43] Kondo S and Nanbu K. A self-consistent numerical analysis of a planar dc magnetron discharge by the particle-in-cell/Monte Carlo method. *J. Phys. D: Appl. Phys.*, 32:1142, 1999.

[44] Shon C H and Lee J K. Modeling of magnetron sputtering plasmas. *Applied Surface Science*, 192(1-4):258, 2002.

[45] Kusumoto Y and Iwata K. Numerical study of the characteristics of erosion in magnetron sputtering. *Vacuum*, 74:359, 2004.

[46] Nanbu K, Mitsui K, and Kondo S. Self-consistent particle modelling of dc magnetron discharges of an O_2/Ar mixture. *J. Phys. D: Appl. Phys.*, 33(1):2274, 2000.

[47] Bultinck E, Kolev I, Bogaerts A, and Depla D. The importance of an external circuit in a particle-in-cell/monte carlo collisions model for a direct current planar magnetron. *J. Appl. Phys.*, 103:013309, 2007.

[48] Bultinck E, Mahieu S, Depla D, and Bogaerts A. The reactive sputter deposition of a TiN film, simulated with a particle-in-cell/Monte Carlo collisions model. *New J. Phys.*, 11:023039, 2009.

[49] Vahedi V, Birdsall C K, Lieberman M A, DiPeso G, and Rognlien T D. Verification of frequency scaling laws for capacitive radio-frequency discharges using two-dimensional simulations. *Physics of fluids B*, 5(7):2719, 1993.

[50] Vahedi V and DiPeso G. Simultaneous potential and circuit solution for two-dimensional bounded plasma simulation codes. *Journal of Computational Physics*, 131:149, 1997.

[51] Raizer Y R. *Gas Discharge Physics.* Springer-Verlag Berlin Heidelberg, 1991.

[52] Kolev I. *Particle-in-cell - Monte Carlo Collisions Simulations for a Direct Current Planar Magnetron Discharge.* PhD thesis, University of Antwerp, 2007.

[53] Fourth conference on the numerical simulation of plasma, Naval research laboratory, Washington DC: 3-67. *Relativistic plasma simulation - optimization of a hybrid code*, november 1970.

[54] Vincenti W G and Kruger C H Jr. *Introduction to Physical Gas Dynamics.* John Wiley & Sons Inc., New York, 1965.

[55] Georgieva V. *Computer Modeling of Low-pressure Fluorocarbon-based Discharges for Etching Purposes.* PhD thesis, University of Antwerp, 2005.

[56] Okhrimovskyy A, Bogaerts A, and Gijbels R. Electron anisotropic scattering in gases: a formula for Monte Carlo simulations. *Phys. Rev. E*, 65:037402, 2002.

[57] Nanbu K. Probability theory of electron-molecule, ion-molecule, molecule-molecule, and Coulomb collisions for particle modeling of materials processing plasmas and gases. *IEEE Trans. on Plasma Science*, 28(3):971, 2000.

[58] Phelps A V. The application of scattering cross sections to ion flux models in discharge sheaths. *J. Appl. Phys.*, 76(2):747, 1994.

[59] Lewis M A, Glocker D A, and Jorne J. Measurements of secondary-electron emission in reactive sputtering of aluminium and titanium nitride. *Journal of Vacuum Science and Technology A*, 7(3):1019, 1989.

[60] Oechsner H. Electron yields from clean polycrystalline metal surfaces by noble-gas-ion bombardment at energies around 1 keV. *Phys. Rev. B*, 17:1052, 1978.

[61] Depla D, Li X Y, Mahieu S, and De Gryse R. Determination of the effective electron emission yields of compound materials. *J. Phys. D: Appl. Phys.*, 41(20):202003, 2008.

[62] Greenwood J. The correct and incorrect generation of a cosine distribution of scattered particles for Monte-Carlo modelling of vacuum systems. *Vacuum*, 67:217, 2002.

[63] Matsunami N, Yamamura Y, Itikawa Y, Itoh N, Kazumata Y, Miyagawa S, Morita K, Shimizu R, and Tawara H. Energy dependence of the ion-induced sputtering yields of monatomic solids. *Atom. Data Nucl. Data Tables*, 31(1):1, 1984.

[64] Sigmund P. Theory of sputtering. I. Sputtering yield of amorphous and polycrystalline targets. *Phys. Rev.*, 184(2):383, 1969.

[65] Thompson M W. II. The energy spectrum of ejected atoms during the high energy sputtering of gold. *Philos. Mag.*, 18(152):377, 1968.

[66] Depla D, Mahieu S, and De Gryse R. Magnetron sputter deposition: linking discharge voltage with target properties. *Thin Solid Films*, 517:2825, 2009.

[67] Mahieu S, Van Aeken K, Depla D, Smeets D, and Vantomme A. Dependence of the sticking coefficient of sputtered atoms on the target - substrate distance. *J. Phys. D: Appl. Phys.*, 41(15):152005, 2008.

[68] Kubart T, Kappertz O, Nyberg T, and Berg S. Dynamic behaviour of the reactive sputtering process. *Thin Solid Films*, 515:421, 2006.

[69] Hirschfelder J O, Curtiss C F, and Bird R B. *Molecular Theory of Gases and Liquids.* John Wiley & Sons Inc., New York, 1964.

[70] Zhen S and Davies G J. Calculation of the Lennard-Jones n-m potential energy parameters for metals. *Phys. Stat. Sol. (a)*, 78:595, 1983.

[71] Svehla R A. Estimated viscosities and thermal conductivities of gases at high temperatures. *National Aeronautics and Space Administraion (NASA), Technical Report*, pages R–132, 1962.

[72] Hockney R W and Eastwood J W. *Computer Simulations using Particles.* Bristol: IOP publishing, 1988.

[73] Kawamura E, Birdsall C K, and Vahedi V. Physical and numerical methods of speeding up particle codes and paralleling as applied to rf discharges. *Plasma Sources Sci. Technol.*, 9:413, 2000.

[74] Bowers K J. Accelerating a particle-in-cell simulation using a hybrid counting sort. *Journal of Computational Physics*, 173:393, 2001.

[75] Verboncoeur J P, Alves M V, Vahedi V, and Birdsall C K. Simultaneous potential and circuit solution for 1d bounded plasma particle simulation codes. *Journal of computational physics*, 104:321, 1993.

[76] Lawson W S. Particle simulation of bounded 1d plasma systems. *Journal of Computational Physics*, 80(3):253, 1989.

[77] Depla D, Buyle G, Haemers J, and De Gryse R. Discharge voltage measurements during magnetron sputtering. *Surf. Coat. Technol.*, 200:4329, 2006.

[78] Window B and Savvides N. Charged particle fluxes from planar magnetron sputtering sources. *Journal of Vacuum Science and Technology A*, 4(2):196, 1986.

[79] ftp://jila.colorado.edu/collision_data/electronneutral/hayashi.txt.

[80] Phelps A V and Petrovic Z Lj. Cold-cathode discharges and breakdown in argon: surface and gas phase production of secondary electrons. *Plasma Sources Sci. Technol.*, 8:R21, 1999.

[81] Mason N J and Newell W R. Total cross sections for metastable excitation in rare gases. *J. Phys. B: At. Mol. Opt. Phys.*, 20:1357, 1987.

[82] Eggarter E. Comprehensive optical and collision data for radiation action. ii. $Ar*$. *J. Chem. Phys.*, 62(3):833, 1975.

[83] Phelps A V. Cross sections and swarm coefficients for nitrogen ions and neutrals in N_2 and argon ions and neutrals in Ar for energies from 0.1 eV to 10 keV. *Journal of Physical and Chemical Reference Data*, 20(3):557, 1991.

[84] Yeom G Y and Thornton J A. Cylindrical magnetron discharges. Current-voltage characteristics for dc- and rf-driven discharge sources. *J. Appl. Phys.*, 65(10):3816, 1989.

[85] Heirwegh S. Measurements at the university of ghent. Private communications.

[86] Lieberman M A and Lichtenberg A J. *Principles of Plasma Discharges and Materials Processing.* John Wiley & Sons Inc., New York, 1994.

[87] Kuwahara K and Fujiyama H. Applications of the Child-Langmuir law to magnetron discharge plasmas. *IEEE Trans. on Plasma Science*, 22(4):442, 1994.

[88] Bowden M D, Takamura T, Muraoka K, Yamagata Y, James B W, and Maeda M. Measurements of the cathode sheath in a magnetron sputtering discharge using laser induced fluorescence. *J. Appl. Phys.*, 73(8):3664, 1993.

[89] Nanbu K and Kondo S. Analysis of three-dimensional dc magnetron discharge by the particle-in-cell/Monte Carlo method. *Japan. J. Appl. Phys.*, 36:4808, 1997.

[90] Bradley J W and Lister G. Model of the cathode fall region in magnetron discharges. *Plasma Sources Sci. Technol.*, 6:524, 1997.

[91] Lister G. Influence of electron diffusion on the cathode sheath of a magnetron discharge. *J. Vac. Sci. Technol. A.*, 14(5):2736, 1996.

[92] Hyman H A. Electron-impact ionization cross sections for excited states of the rare gases (Ne, Ar, Kr, Xe), cadmium and mercury. *Phys. Rev. A*, 20(3):855, 1979.

[93] Hyman H A. Electron-impact excitation of metastable argon and krypton. *Phys. Rev. A*, 18(2):441, 1978.

[94] Vriens L. Calculation of the absolute ionisation cross sections of He, $He*$, He^{+}, Ne, $Ne*$, Ne^{+}, Ar, $Ar*$, Hg and $Hg*$. *Physics Letters*, 8:260, 1964.

[95] Bogaerts A and Gijbels R. Role of sputtered Cu atoms and ions in a direct current glow discharge: combined fluid and Monte Carlo model. *J. Appl. Phys.*, 79(3):1279, 1996.

[96] Ferreira C M and Ricard A. Modelling of the low-pressure argon positive column. *J. Appl. Phys.*, 54(5):2261, 1983.

[97] Ferreira C M, Loureiro J, and Ricard A. Populations in the metastable and the resonance levels of argon and stepwise ionization effects in a low-pressure argon positive column. *J. Appl. Phys.*, 57(1):82, 1985.

[98] Riseberg L A, Parks W F, and Schearer L D. Penning ionization of Zn and Cd by noble-gas metastable atoms. *Phys. Rev. A*, 8(4):1962, 1973.

[99] Tachibana K. Excitation of the $1s_5$, $1s_4$, $1s_3$, $1s_2$ levels of argon by low-energy electrons. *Phys. Rev. A*, 34(2):1007, 1986.

[100] Phelps A V, Greene C H, and Burke J P Jr. Collision cross sections for argon atoms with argon atoms for energies from 0.01 eV to 10 keV. *J. Phys. B: At. Mol. Opt. Phys.*, 33(16):2965, 2000.

[101] Phelps A V and Jelenkovic B M. Excitation and breakdown of Ar at very high ratios of electric field to gas density. *Phys. Rev. A*, 38(6):2975, 1988.

[102] Robinson R S. Energetic binary collisions in rare gas plasmas. *J. Vac. Sci. Technol.*, 16(2):185, 1979.

[103] Pandey B P, Samarian A, and Vladimirov S V. Dust in the magnetized sheath. *Phys. Plasmas*, 14:093703, 2007.

[104] Chodura R. Plasma-wall transition in an oblique magnetic field. *Phys. Fluids*, 25(9):1628, 1982.

[105] Kim G H, Hershkowitz N, Diebold D A, and Cho M H. Magnetic and collisional effects on presheaths. *Phys. Plasmas*, 2(8):3222, 1995.

[106] Singha B, Sarma A, and Chutia J. Experimental observation of sheath and magnetic presheath over an oblique metallic plate in the presence of a magnetic field. *Phys. Plasmas*, 9:683, 2002.

[107] Oliveira I C, Grigorov K G, Maciel H S, Massi M, and Otani C. High textured AlN thin films grown by rf magnetron sputtering; composition, structure, morphology and hardness. *Vacuum*, 75(4):331, 2004.

[108] Efeoglu I, Arnell R D, Tinston S F, and Teer D G. The mechanical and tribological properties of titanium nitride coatings formed in a four magnetron closed-field sputtering system. *Surf. Coat. Technol.*, 55(1):61, 1993.

[109] Depla D, Heirwegh S, Mahieu S, Haemers J, and De Gryse R. Understanding the discharge voltage behavior during reactive sputtering of oxides. *J. Appl. Phys.*, 101:013301, 2007.

[110] ftp://jila.colorado.edu/collision_data.

[111] Itikawan Y, Hayashi M, Ichimura A, Onda K, Sakimoto K, Takayanagi K, Nakamura M, Nishimura H, and Takayanagi T. Cross sections for collisions of electrons and photons with nitrogen molecules. *Journal of Physical and Chemical Reference Data*, 15(3):985, 1986.

[112] Georgieva V, Bogaerts A, and Gijbels R. Numerical study of $Ar/CF_4/N_2$ discharges in single- and dual-frequency capacitively coupled plasma reactors. *J. Appl. Phys.*, 94(6):3748, 2003.

[113] Henriques J, Tatarova E, Guerra V, and Ferreira C M. Wave driven N_2-Ar discharge. i. self-consistent theoretical model. *J. Appl. Phys.*, 91:5622, 2002.

[114] Nanbu K and Kitatani Y. An ion-neutral collision model for particle simulation of glow discharge. *J. Phys. D: Appl. Phys.*, 28:324, 1995.

[115] Georgieva V, Bogaerts A, and Gijbels R. Particle-in-cell/Monte Carlo simulation of a capacitively coupled radio frequency Ar/CF_4 discharge: Effect of gas composition. *J. Appl. Phys.*, 93(5):2369, 2003.

[116] Temkin A. Internuclear dependence of the polarizability of N_2. *Phys. Rev. A*, 17(3):1232, 1978.

[117] Baragiola R A, Alonso E V, Ferron J, and Olivaflorio A. Ion-induced electron-emission from clean metals. *Surface Science*, 90(2):240, 1979.

[118] Kolev I and Bogaerts A. Calculation of gas heating in a dc sputter magnetron. *J. Appl. Phys.*, 104:093301, 2008.

[119] Mao D, Tao K, and Hopwood J. Ionized physical vapor deposition of titanium nitride: Plasma and film characterization. *J. Vac. Sci. Technol. A.*, 20(2):379, 2002.

[120] Bartzsch H, Gloss D, Bocher B, Frach P, and Goedicke K. Properties of SiO_2 and Al_2O_3 films for electrical insulation applications deposited by reactive pulse magnetron sputtering. *Surf. Coat. Technol.*, 174:774, 2003.

[121] Kelly P J, Beevers C F, Henderson P S, Arnell R D, Bradley J W, and Backer H. A comparison of the properties of titanium-based films produced by pulsed and continuous dc magnetron sputtering. *Surf. Coat. Technol.*, 174-175:795, 2003.

[122] O'Brien J and Kelly P J. Characterisation studies of the pulsed dual cathode magnetron sputtering process for oxide films. *Surf. Coat. Technol.*, 142:621, 2001.

[123] Henderson P. S., Kelly P. J., Arnell R. D., Backer H., and Bradley J. W. Investigation into the properties of titanium based films deposited using pulsed magnetron sputtering. *Surf. Coat. Technol.*, 174(1):779, 2003.

[124] De Bleecker K, Herrebout D, Bogaerts A, Gijbels R, and Descamps P. One-dimensional modelling of a capacitively coupled rf plasma in silane/helium, including small concentrations of O_2 and N_2. *J. Phys. D: Appl. Phys.*, 36:1826, 2003.

[125] Guerra V and Loureiro J. Kinetic model of a low-pressure microwave discharge in $O_2 - N_2$ including the effects of O-ions on the characteristics for plasma maintenance. *Plasma Sources Sci. Technol.*, 8:110, 1999.

[126] Kossyi A, Kostinsky A Y, Matveyev A A, and Silakov V P. Kinetic scheme of the non-equilibrium discharge in nitrogen-oxygen mixtures. *Plasma Sources Sci. Technol.*, 1:207, 1992.

[127] Tinck S, Boullart W, and Bogaerts A. Investigation of etching and deposition processes of $\mathrm{Cl_2/O_2/Ar}$ inductively coupled plasmas on silicon by means of plasma-surface simulations and experiments. *J. Phys. D: Appl. Phys.*, 42:095204, 2009.

[128] Rauf S and Kushner M J. Argon metastable densities in radio frequency Ar, $\mathrm{Ar/O_2}$ and $\mathrm{Ar/CF_4}$ electrical discharges. *J. Appl. Phys.*, 82(6):2805, 1997.

[129] Boukrouh S, Bensaha R, Bourgeois S, Finot E, and Marco de Lucas M C. Reactive direct current magnetron sputtered $\mathrm{TiO_2}$ thin films with amorphous to crystalline structures. *Thin Solid Films*, 516:6353, 2008.

[130] Poelman H, Tomaszewski H, Poelman D, Depla D, and De Gryse R. Effect of the oxygen deficiency of ceramic TiO_{2-x} targets on the deposition of $\mathrm{TiO_2}$ thin films by DC magnetron sputtering. *Surf. Interface Anal.*, 36:1167, 2004.